Detector Control Systems and Searches for Leptonic Decays of the Higgs Boson in the ATLAS Experiment at the LHC

Russell Turner

Thesis submitted for the title of Doctor of Philosophy

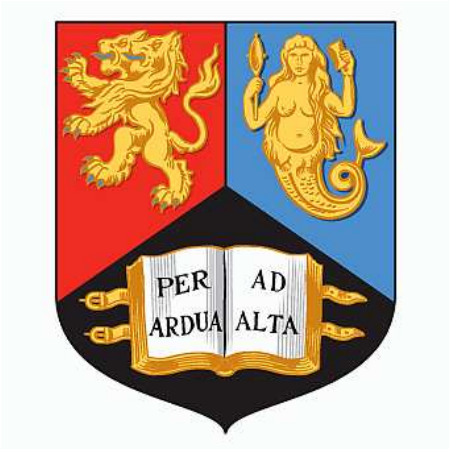

Particle Physics Group,
School of Physics and Astronomy,
University of Birmingham.

August 9, 2020

A long tale, like a tall Tower,
must be built a stone at a time

Stephen King

Abstract

The Large Hadron Collider at CERN has recently finished Run-II, during which proton beams were collided at a centre of mass energy of 13 TeV, producing data equivalent to a total integrated luminosity of 139 fb^{-1} for the ATLAS experiment. The collider and its experiments have now entered into a shutdown period, in which various components will be upgraded to accommodate for a higher luminosity (300 fb^{-1} expected) run (Run-III). This thesis presents the development of a control and monitoring system for the upgrade to the ATLAS level one calorimeter trigger. This system is designed for use in the ATLAS control room, and so needs to be easily understood and used by shifters who are not necessarily experts of the trigger system.

Also presented in this thesis are two analyses related to searches for the decays of the Higgs boson to lepton-antilepton final states by the ATLAS experiment. The first of these analyses is an analysis of the prospects of measuring the $H \to \mu^+\mu^-$ decay channel during the high luminosity phase of the LHC, Run-IV. During this run, ATLAS is expected to collect a total of 3000 fb^{-1} worth of data at a centre of mass energy of 14 TeV. This prospects analysis finds an expectation of measuring the decay with a significance of 9.6σ and a fractional precision on the branching ratio of 13% assuming the standard model decay rate.

The second analysis is a search for the $H \to e^+e^-$ decay channel using the entire ATLAS dataset from Run-II. No significant excess of events is observed and a 95% CL_S upper limit on the branching ratio $\mathcal{B}(H \to e^+e^-)$ of 3.6×10^{-4} is set, approximately a factor of 5 lower than the previously observed limit. This limit is four orders of magnitude larger than the standard model value of the branching ratio, 5×10^{-9}, and is compatible with the expected limit of 3.5×10^{-4}.

Declaration of Author's Contribution

As a collaboration containing thousands of members, work completed within the ATLAS experiment is naturally a team effort. This is seen through the design, construction and operation of both the LHC and the ATLAS detector. In addition to this, the other LHC experiments are involved in the development of shared tools and techniques used for common issues. The work presented in this thesis benefits greatly from the work of the entire CERN community. In addition to this work, I have also contributed to the ATLAS experiment through shift work in the ATLAS control room, where I worked as a trigger and run control shifter.

Chapters 2, 3 and 4 present details of the design of the ATLAS detector and the detector control systems (DCS) used by the ATLAS collaboration. My contribution to this work is mostly contained to the DCS of the level one calorimeter trigger as described in chapter 3, for which I was involved in the scripting and design of the finite state machine (FSM), as well as that of the user interface panels. I was also involved in the testing and development of a simplified DCS project for the level one topological trigger during Run-II, for which I contributed to the scripting of Open Platform Communication servers, as well as to the back-end FSM and user interface.

Chapters 6, 7 and 8 present work pertaining to the main focus of the thesis, searches for leptonic decays of the Higgs. While working with an analysis group, and sharing many different analysis tools, the work presented in these chapters is largely my own work. For the $H \to \mu^+\mu^-$ prospects analysis, I contributed to the event selection, classification and fitting as described in the chapter. I also performed the validation study of the smeared Monte Carlo samples. The smearing functions used, as well as the optimisation of the VBF category, were the work of other members of the collaboration who had worked on the analysis previously.

For the $H \to e^+e^-$ analysis presented in chapters 7 and 8, I was part of a small analysis team within the larger $H \to \mu^+\mu^-$ analysis sub-group in ATLAS. Although the overall method was based on similar analyses of the $H \to \mu^+\mu^-$ decay, the analysis chapters represent my own work, with the exceptions being the estimation of the spurious signal uncertainty, the study of the $H \to \gamma\gamma$ background and the consideration of the background modelling uncertainty. The results of this analysis are published in the Physics Letters B journal [1].

Acknowledgements

It has been an enormous privilege to work on this doctorate over the past three years. I have been able to work with some brilliant scientific minds, and achieve a lifelong goal of working on the forefront of particle physics research. Naturally, it would be impossible to thank every person individually who has helped me to get here, but nevertheless I will try my best to do so over the coming paragraphs.

First and foremost, I would like to thank the STFC for their financial support, as without it no aspect of this work would have been possible. They have empowered me to join a fantastic research group at the University of Birmingham, to become part of one of the most exciting scientific collaborations in the world at CERN, and to spend a year working with many international collaborators in Geneva. Over the course of my research I have worked with a number of research and analysis teams. In particular, I would like to thank the Hmumu, DCS and L1Calo teams for their valuable input into the work that makes up the content of this thesis. In no particular order, Andy, Hanna, Jan, Tom, Schlenk, Piotr, Paris, Revital, Juraj, Francesco, Steve, Richard, Bruce, Ian, Dave, and many others from these teams have helped me in some way, and I am immensely grateful towards all of them. In addition, I would like to thank the Birmingham Higgs group, especially Kostas, Andy, Rhys, Tom and Elliott, for their week-in week-out guidance and advice necessary to keep my research at a high standard. I would also like to thank all the other research staff in the Birmingham particle physics for all their advice. Finally, I'd like to recognise the enormous contribution of my supervisor Paul. He has gone above and beyond time and time again and I cannot possibly thank him enough.

I have made a lot of friends over the course of this PhD and it would be remiss of me not to recognise their contribution to keeping me sane. Thanks to Matt, Alasdair, James, Andy, Tim, Kendrick, Briglin, Elliott, Kristian, Rob, Jack, Ryan, John, Gov, Nandish, Dan, Robbie, Patrick, Jonathan, Robert, Cameron, Antonio, Alexis, Tom, Will, Harry, Julia and Gareth for all the Friday beers at the staff house, for all the curries at the Dilshad, and for all the films, games, quizzes, bets, and other activities we did when we probably should have been working.

Somewhat surprisingly, I have some friends who aren't particle physicists. Some

of the highlights of these are: Joe, James, Sam, Tessa, Harry, Jake, Matt, Ryan, Seth, Chris, Amber, James, Ian, Julie, Garry, Carol, Matt, Joe, Steve, Kay, George, Brendan, Tom, Lucy, Martyn and Sam. They have all helped me in various ways over the years, but for legal reasons I have decided not to publish any details here.

Finally, I have to thank my family as, without them I would not be here, either writing this thesis or alive at all. Thank you Mark for lending me a sympathetic ear when times were tough. Thank you Terri for being one of my best friends and for constantly inspiring me with your intellect, passion and drive. That's your drive, rather than your driving. Thank you Mum and Dad, for the omnipresent love, guidance (both moral and practical) and support you have given me since you cruelly cursed me with existence all those years ago. Plus an extra thank you for helping me move out of my house in the middle of a global pandemic, and getting it all done in a day and a half so I could still finish on time.

Contents

Chapter 1

Introduction

At the time of writing of this thesis, the Large Hadron Collider at CERN has recently finished its first major run at a centre-of-mass energy of 13 TeV (Run-II), and is now in the process of upgrading for a new run (Run-III). Over the lifetime of the LHC so far, the succeses have been many, from major discoveries such as those of the pentaquark at LHCb [2] and of the Higgs boson at ATLAS and CMS [3, 4] to precision measurements of Standard Model processes, all of which have expanded or refined our knowledge of the universe's fundamental building blocks. As one of the main LHC experiments, the general purpose detector experiment ATLAS has played a large role in these successes.

The work presented in this thesis is representative of projects undertaken within the ATLAS experiment, both during the recently finished Run-II and in preparation for future runs. This work can broadly be split into two topics: development of the detector control systems of the experiment and searches for light leptonic decays of the observed Higgs Boson.

Chapter 2 provides an overview of the Large Hadron Collider and the ATLAS experiment. Particular detail is given to the sub-detectors of ATLAS and their performance as relevant to the presented physics analyses, in addition to the upgraded trigger systems for which detector control systems were developed. Chapters 3 and

4 describe these control systems, with chapter 3 describing the common concepts and techniques used on a detector-wide level, and chapter 4 describing the systems developed for the upgraded level one calorimeter trigger.

Chapter 5 describes qualitatively the fundamental theories of particle physics, leading up to the proposal of a Higgs field and its corresponding gauge boson, and then brings this theory into the context of the LHC, and shows the Higgs phenomena one would expect to measure at a collider experiment. This chapter also shows a rundown of relevant results in the Higgs sector from both ATLAS and CMS.

Chapter 6 presents an analysis of prospective future results during Run-IV of the LHC, during which the LHC will be running under a high luminosity regime at a centre of mass energy of 14 TeV. This prospects analysis aims to quantify the expected results of a search for the dimuon decay of the Higgs boson. It is undertaken through the use of simulated proton-proton events, passed through a series of smearing functions which parameterise the expected performance of the upgraded ATLAS detector.

Chapters 7 and 8 respectively show the methodology and results of an analysis of data from the entirety of Run-II. This run was performed at a centre of mass energy of 13 TeV, and the data amounts to an integrated luminosity of 139 fb^{-1}. The analysis presented is a search for the dielectron decay of the Higgs boson. In brief summary, the analysis consists of a data-driven fit in order to parameterise the expected background, and a search for a signal over this background. The signal is parameterised via a fit to simulated $H \rightarrow e^+e^-$ events, passed through a full simulation of the ATLAS detector.

Finally, chapter 9 is an overview of all the work and results presented in the thesis, and offers some concluding remarks on their impact.

Chapter 2

The Large Hadron Collider and the ATLAS Experiment

2.1 The Large Hadron Collider

The Large Hadron Collider (LHC) is a 26.7 km circumference proton synchrotron housed in an underground tunnel near Geneva, Switzerland. This tunnel was originally used for the Large Electron Positron (LEP) collider [5]. The LHC has two beam pipes, each carrying a proton beam around the ring in opposite directions. The protons are supplied by the CERN accelerator complex, feeding from the proton synchrotron booster through to the proton synchrotron (PS) [6] and super proton synchrotron (SPS) [7] before finally being injected into the LHC, as shown in figure 2.1. The beams are then accelerated to a target energy. In the first runs of the LHC (Run-I) this target energy started at 3.5 TeV and was increased to 4 TeV later for a centre of mass energy of $\sqrt{s} = 7(8)$ TeV at the point of collision. In the following runs (Run-II) there was a higher target beam energy of 6.5 TeV for $\sqrt{s} = 13$ TeV. The LHC is designed for a maximum beam energy of 7 TeV. The proton beams are contained in their orbit by a system of 1232 dipole and 392 quadrupole magnets, which steer and focus the beams respectively. The LHC complex is also used for

heavy ion experiments, in which collisions (usually of lead ions) are used to recreate the conditions of the early universe. A more detailed description of the LHC machine is given at [8].

There are seven experiments based on the LHC, although only four of these have their own interaction points, where the two proton beams collide:

- A Toroidal LHC ApparatuS (ATLAS) is a general purpose detector experiment and the main focus of this thesis. ATLAS is designed with many different physics processes in mind and operates at a high luminosity ($\mathcal{L} = 2.1 \times 10^{34}$ cm^{-2} s^{-1}). It is described in more detail in section 2.2.

- Compact Muon Solenoid (CMS) is another general purpose detector, designed independently from ATLAS. The aims of CMS are the same as those of ATLAS, and both detectors operate at the same instantaneous luminosity. Operating with two independent general purpose experiments allows for cross-checking of results and independent confirmation of any discoveries made, as well as combinations of measurements to improve precision.

- LHC beauty (LHCb) is designed for studying the physics of the bottom quark. As opposed to the other three experiments, which are built symmetrically around the interaction point, LHCb is a forward detector, built solely on one side in order to precisely detect particles produced in a forward direction from the collision, whilst reducing costs. LHCb operates at an instantaneous luminosity of $\mathcal{L} = 10^{32}$ cm^{-2} s^{-1}, lower than the luminosities provided to ATLAS or CMS.

- A Large Ion Collider Experiment (ALICE), as its name suggests, is based on heavy ion collisions at the LHC. These collisions are performed at a centre of mass energy of around 2.6 TeV per nucleon, at an instantaneous luminosity of around $\mathcal{L} = 2 \times 10^{30}$ cm^{-2} s^{-1}. The main focus of ALICE is the study of a state of matter called the quark-gluon plasma.

The other three experiments are TOTEM, LHCf and MoEDAL. TOTEM and LHCf

are forward physics experiments, i.e. they focus on particles that are only deflected by a small angle from the beam line. They are based on detectors either side of the CMS and ATLAS interaction points respectively. MoEDAL is based near the LHCb interaction point, and is focussed on the search for magnetic monopoles.

The target luminosity at the ATLAS interaction point (IP) is 2.1×10^{34} cm^{-2} s^{-1}. The instantaneous luminosity at a proton collider like the LHC is given by

$$\mathcal{L} = f \frac{n_1 n_2}{4\pi\sigma_x\sigma_y}, \tag{2.1}$$

where f is the bunch crossing frequency, n_1 and n_2 are the numbers of protons per bunch in each beam, and σ_x and σ_y are the horizontal and vertical beam sizes, transverse to the beam line. So, in order to reach a high luminosity, the LHC must produce proton beams with large numbers of protons per bunch, and a low cross-sectional area transverse to the beam line. The final result of this is to the order of 1 billion proton-proton collisions every second. To this end, each beam in the LHC contains around 2800 bunches, each bunch containing the order of 10^{11} protons. The beams are then collided, at a rate of one bunch crossing every 25 ns. For each bunch crossing there are around 60 proton-proton collisions.

This huge collision rate presents some problems to the experiments. The first of these is, as there are so many collisions per bunch crossing, that many particles from separate collisions may inhabit the detector at the same time, making the different physics processes difficult to separate. This phenomenon is known as pile up. Pile-up at the LHC consists of both in-time and out-of-time pile up, defined based on whether the additional proton-proton collisions occur during the same bunch crossing or during adjacent bunch crossings. The other main issue is that each event that is recorded by an experiment takes time to be saved, during which time other interesting events may occur and be missed. This is known as dead-time. A typical dead-time fraction for the ATLAS experiment is around 1% [9].

Figure 2.2 shows the delivered luminosity over the course of Run-I and Run-II in

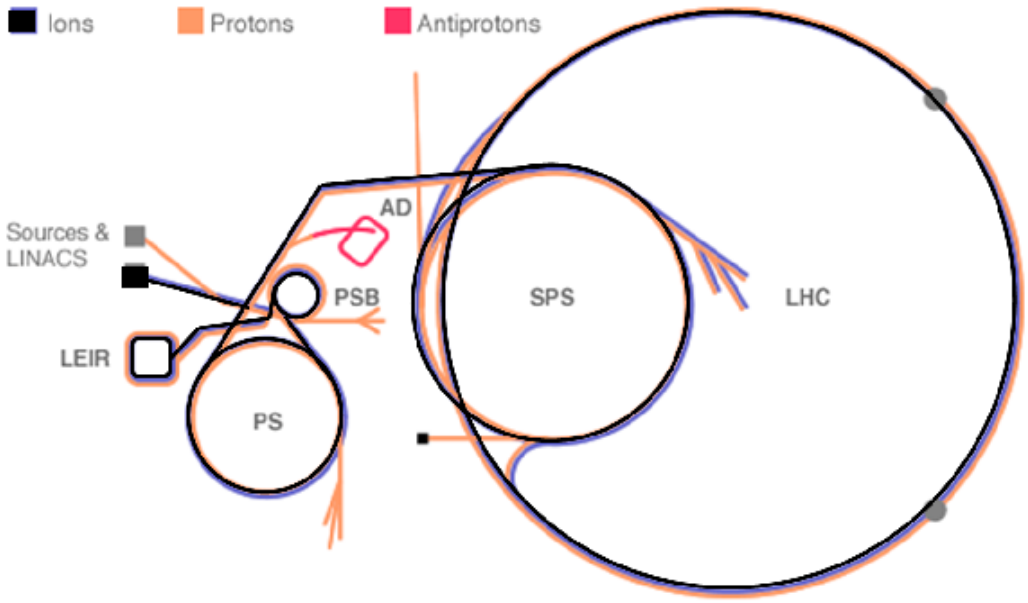

Figure 2.1: The CERN accelerator complex. The protons/ions are passed through a series of accelerators before injection into the LHC ring. Protons from the accelerator complex are also used in non-LHC experiments around CERN [10].

ATLAS. It can be seen that for each year of running (besides 2015 which had a later than usual start) the total delivered luminosity has increased. The LHC is currently expected to deliver around 350 fb^{-1} of luminosity by the end of Run-III (2022-2024). Details of the upgrades being made to ATLAS for Run-III (the Phase 1 upgrade) are given in section 2.2.7.

2.1.1 The High Luminosity LHC

The LHC has already reached several major milestones in terms of physics discoveries, including the discovery of the Higgs boson by ATLAS and CMS [3, 4] and the discovery of pentaquarks by LHCb [2]. However, to reach some of the more aspirational goals of the project, for example finding evidence of di-Higgs production, a much higher luminosity is needed. This will require a major upgrade of the collider and the experiments, referred to as the High Luminosity (HL) LHC. For the ATLAS experiment, the nominal target instantaneous luminosity is $\mathcal{L} = 5 \times 10^{34}$

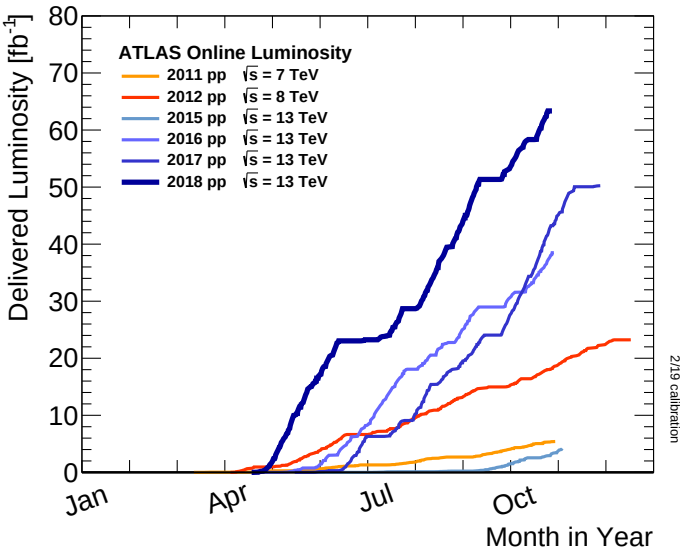

Figure 2.2: Delivered proton-proton luminosity in the ATLAS experiment between 2011 and 2018. No luminosity is recorded for 2013 or 2014 as the machine was shut down to upgrade to a higher collision energy [11].

$\text{cm}^{-2}\ \text{s}^{-1}$, for an integrated luminosity of around 250 fb^{-1} per year, reaching a final value of 3000 fb^{-1} at the end of operation. The HL-LHC is also expected to reach an "ultimate" target luminosity of $\mathcal{L} = 7.5 \times 10^{34}\text{cm}^{-2}\ \text{s}^{-1}$, corresponding to a final luminosity of around 4000 fb^{-1} and an average of 200 collisions per beam crossing [12]. The first year of HL-LHC running (Run-IV) is currently planned to be 2027. More detail on the upgrade of the LHC can be found in the technical design report [13]. Section 2.2.8 describes upgrades to the ATLAS experiment planned for the HL-LHC (the Phase 2 upgrade).

2.2 The ATLAS Detector

As mentioned earlier, ATLAS is a general purpose detector, designed to operate at high luminosity and detect the majority of interesting physics events produced in pp collisions. To this end, it is designed symmetrically around the interaction point, in order to detect particles deflected at most angles with respect to the beam line. The system of coordinates at ATLAS is defined using cylindrical polar coordinates r, ϕ

and z. The z axis is defined to run along the beam line, and so r is the transverse distance from the beam line, and the azimuthal angle ϕ is defined in the cartesian $x-y$ plane (where x points from the IP to the centre of the LHC ring and y points from the IP directly upward).

Broadly speaking, the detector is made up of three main layers. The first layer, the inner detector, detects the paths of all charged particles passing through it. It is housed within a large solenoidal magnet in order to measure the momentum of the particles as they pass through the magnetic field. The second layer is the calorimeter system and this captures and measures the energy of most particles that pass through it. The calorimeter is split into an electromagnetic layer which captures electrons and photons, and a hadronic layer which captures strongly interacting particles. The final layer is the muon spectrometer, a collection of trackers that detects any charged particles escaping the calorimeter, which in the majority of cases are muons. An overview of the entire ATLAS detector is shown in figure 2.3.

Three common kinematic variables used by ATLAS are the transverse momentum, p_T, the rapidity, y, and the pseudorapidity, η. Transverse momentum is the simplest to define, as the component of momentum transverse to the beam line, $p_T = \sqrt{p_x^2 + p_y^2}$. The rapidity of a particle with mass M, momentum $\vec{p}$ and energy $E = \sqrt{|\vec{p}|^2 + M^2}$ is given by

$$y = \frac{1}{2} \ln \left[\frac{E + p_z}{E - p_z} \right]. \tag{2.2}$$

For highly relativistic particles, where $E \approx |\vec{p}|$, this reduces to the pseudorapidity

$$\eta = -\ln \left[\tan \frac{\theta}{2} \right], \tag{2.3}$$

where θ is the angle with respect to the beam line. Under this definition, η has a value of infinity at an angle of $\theta = 0$ and a value of 0 at $\theta = \pi$. The pseudorapidity is a variable for which intervals ($\delta\eta$) are invariant under Lorentz boosts along the beam axis. It is quite common in ATLAS to define detected particles in terms of

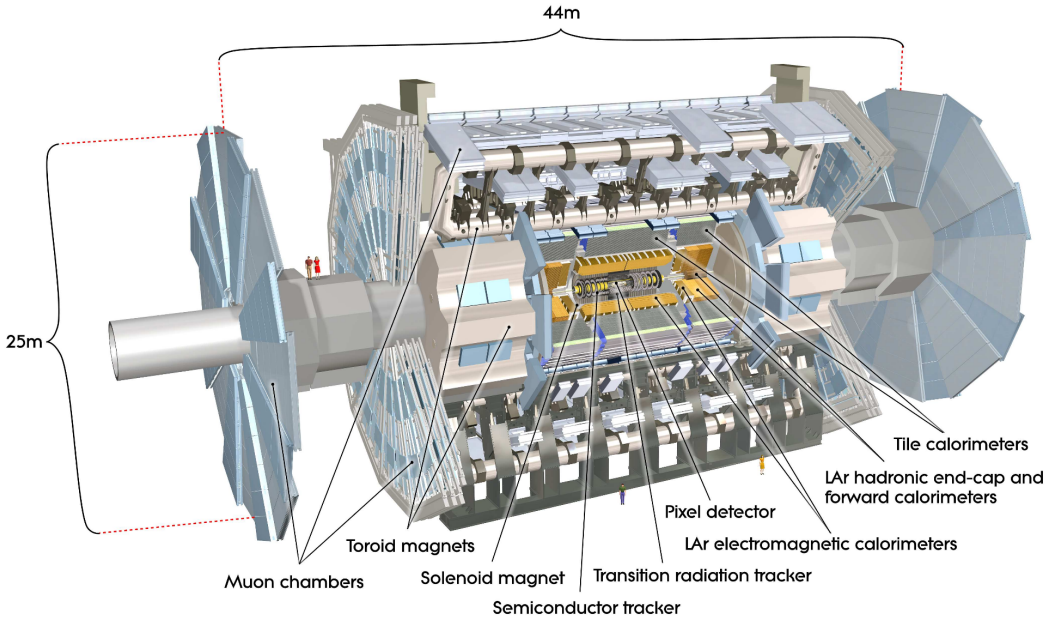

Figure 2.3: Schematic view of the ATLAS detector as installed in the experimental cavern at LHC point 1 [14].

the coordinates (p_T, η, ϕ, E). Two other common variables are the impact parameter d_0, the distance of closest approach to the beam line, and the longitudinal impact parameter z_0, the value of z at the point where d_0 is defined.

2.2.1 Magnet System

ATLAS has two main magnet systems, a solenoid surrounding the inner detector and a toroidal system surrounding the muon spectrometer. These are used to curve the paths of charged particles traveling through the detector, and then the curvatures of their trajectories can be used to calculate their momenta. The solenoid surrounding the inner detector produces a 2 T magnetic field. The tile calorimeters in the barrel and endcap (see section 2.2.3) form a return yoke for the solenoid, positioned to minimise the electromagnetic forces on the solenoid itself. The toroid system provides different strength fields in the barrel and in the endcap, with a 0.5 T field provided in the barrel and a 1.0 T field provided in each endcap.

2.2.2 The Inner Detector

The Inner Detector (ID) at ATLAS is designed to track charged particles that pass through it, in order to measure their momenta to a good degree of accuracy and to extrapolate their trajectory backwards to find the primary vertex (the point where the initial collision occured) and the secondary vertices (points at which particles have decayed after the collision). To achieve the desired accuracy, the ID needs to measure each particle very precisely. A large part of the challenge with this is the complexity of the environment; approximately 1000 particles will pass through the detector for each 25 ns bunch crossing [14].

The ID is made up of three different sections, each at different radii. The innermost section is the Pixel Detector which occupies radii of $31 < R < 242$ mm. This is then followed by the Semiconductor Tracker, which occupies radii of $255 < R < 549$ mm in the barrel and $251 < R < 610$ mm in the endcaps. Finally there is the Transition Radiation Tracker at radii of $554 < R < 1082$ mm in the barrel and $617 < R < 1106$ mm in the endcaps. These subdetectors are described in the following sections. The ID has angular coverage going up to an $|\eta|$ value of 2.5 and, as discussed in section 2.2.1, it is contained within a solenoid providing a uniform 2 T magnetic field. A cut-away view of the ID can be seen in figure 2.4.

2.2.2.1 Pixel Detector

The pixel detector is made up of 1744 identical n-type silicon pixel sensors. These sensors are 250 μm thick, with external dimensions of 19×63 mm^2, and they are arranged into three barrel layers along with three disc layers in each endcap. As the innermost layer, the pixel detector requires the highest spatial resolution within the ID and so each pixel offers a resolution of 10 μm $(R-\phi) \times 115$ μm (z) in the barrel and 10 μm $(R-\phi) \times 115$ μm (R) in the endcap [16].

During the long shutdown between Run I and Run II, the ID was upgraded with a

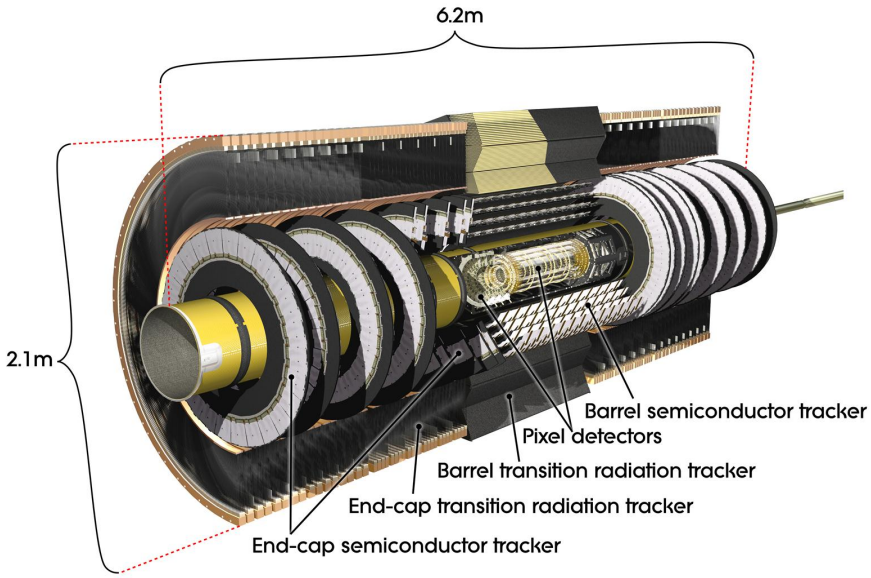

Figure 2.4: Computer generated cut-away view of the ATLAS Inner Detector [15]

fourth pixel layer known as the Insertable B-Layer (IBL) [17]. The purpose of this extra layer was to improve the capability to find the primary and secondary vertices in the ATLAS detector.

2.2.2.2 Semiconductor Tracker

The Semiconductor Tracker (SCT) consists of 4 barrel layers and 2×9 endcap layers. It is again made up of 250 μm thick silicon sensors, but here they are arranged as strips rather than as pixels. Each module typically contains two pairs of strips: one pair parallel to the z-axis in the barrel or perpendicular in the endcaps, and a second pair at the other end of the module, aligned at a slight 40 mrad stereo angle offset to the first, providing 580 μm z resolution in the barrel and 580 μm R resolution in the endcaps. There are a total of 4088 modules within the SCT, each providing a spatial resolution of approximately 17 μm in $R - \phi$ [16].

The SCT uses radiation hard read-out chips to process the signal. Each chip is responsible for read-out from 128 strips, and will register a hit for the strip if the charge deposited within exceeds a threshold.

2.2.2.3 Transition Radiation Tracker

The Transition Radiation Tracker (TRT) uses different technology to the other two subdetectors, consisting of 4mm diameter proportional drift tubes filled with a mixture of Xenon (70%), Carbon Dioxide (27%) and Oxygen (3%). Each of these tubes is 144 cm long in the barrel and 37 cm long in the endcaps. In total, the TRT consists of 298304 of these drift tubes, and each one provides 130 μm spatial precision in the $R - \phi$ plane [14].

The spatial resolution in the TRT is notably lower than in the Pixel Detector or the SCT. However, this is balanced by the number of measurements it can make along the track length; a charged particle with $p_T > 0.5$ GeV and $|\eta| < 2.0$ is expected to traverse around 36 drift tubes [14]. Another benefit of the TRT is that electrons traversing through create a larger signal than other charged particles, which helps with electron identification.

2.2.2.4 Performance

As the magnetic field of the surrounding solenoid is parallel to the beam line, the curvature in the trajectory of charged particles in the ID provides a direct measurement of their transverse momentum p_T. In general, for a trajectory along an arc with chord length L and sagitta s, in a field of strength B, the transverse momentum can be calculated as

$$p_T = \frac{0.3BL^2}{8s}. \tag{2.4}$$

This equation provides the p_T in units of GeV, given the sagitta and chord length in metres and the magnetic field strength in Tesla. The geometry of this measurement can be seen in figure 2.5. In the actual measurement during data taking, energy loss and multiple scattering need to be taken into account, so the calculation becomes more complex than this simple formula. The trajectories are formed starting from groups of three hits in the ID, known as track seeds. An algorithm is then used

to combine track seeds with compatible hits throughout the ID, and when all the compatible hits are collected, a fit is performed to calculate the final trajectory. A more detailed description of this reconstruction process can be found at [18, 19].

Overall, the momentum resolution for the ID can be parameterised as

$$\sigma\left(\frac{1}{p_T}\right) = a \oplus \frac{b}{p_T}, \tag{2.5}$$

where a and b are both fitted parameters dependent on pseudorapidity, representing the energy loss and multiple scattering respectively. As an example, in the low pseudorapidity range of $0.00 < |\eta| < 0.25$, a has a value of 0.365 TeV^{-1} and b has a value of 12.3×10^{-3} [20]. The uncertainty is given as an uncertainty on $\frac{1}{p_T}$, as it is related to the uncertainty on measuring the sagitta s, but through error propagation, the uncertainty on the measurement p_T can be found as

$$\frac{\sigma(p_T)}{p_T} = ap_T \oplus b, \tag{2.6}$$

and so it can be seen that at low p_T, multiple scattering dominates the resolution.

Figure 2.6 shows the impact parameter resolution, as measured by the inner detector, in data from 2012 and 2015. These measurements were performed using events containing at least one reconstructed vertex with at least two associated tracks. This shows the improvement in impact parameter measurement due to the insertion of the IBL, which was inserted in between the two years. In the regions of lowest $|\eta|$ and p_T values, this amounts to a 40% improvement due to the IBL, relative to the initial Run I resolution [21].

2.2.3 The Calorimeters

The calorimeter system is designed to capture the majority of particles that pass through it, in order to measure their energy and position. It is made up of two layers: an inner Electromagnetic Calorimeter (ECAL) designed to measure electrons and

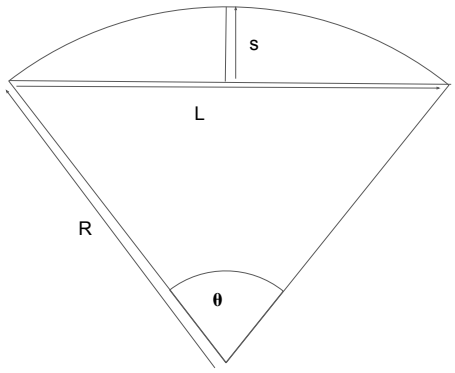

Figure 2.5: Geometry used for measuring transverse momentum. The magnetic field runs perpendicular to the page.

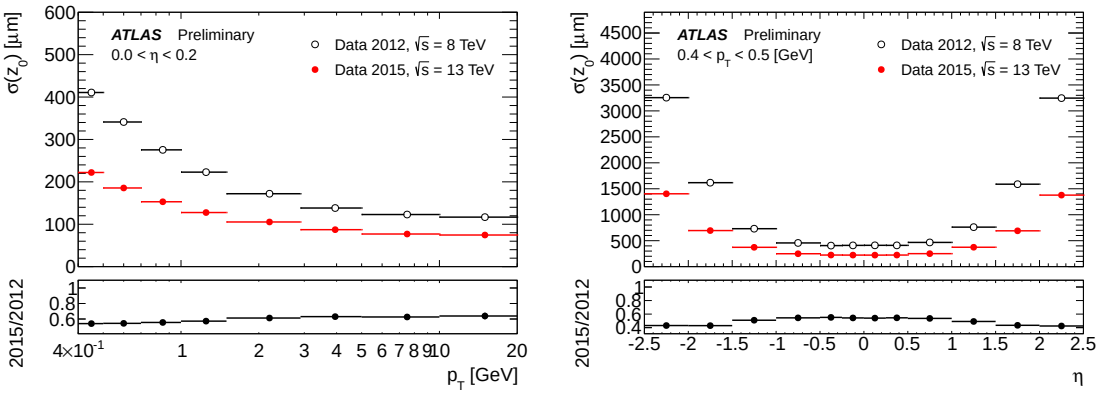

(a) (b)

Figure 2.6: Longitudinal impact parameter resolution, measured from data in 2015, $\sqrt{s} = 13$ TeV, compared to that measured from data in 2012, $\sqrt{s} = 8$ TeV, as a function of (a) p_T in the region $0.0 < \eta < 0.2$, and (b) η in the region $0.4 < p_T < 0.5$ GeV [21].

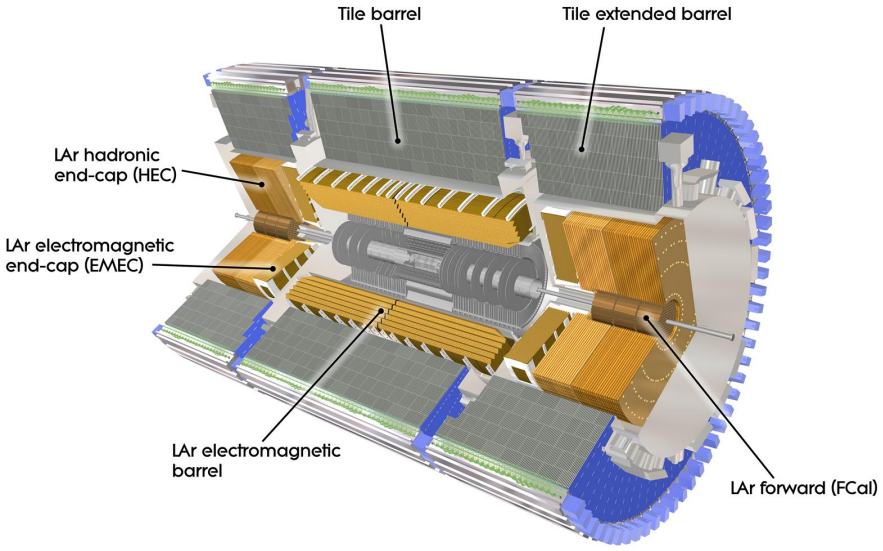

Figure 2.7: Computer generated image of the ATLAS calorimeter, surrounding the ID (greyed out) [22].

photons, and an outer Hadronic Calorimeter (HCAL) designed to measure hadrons. There is also a forward calorimeter (FCAL) for particles at high pseudorapidities. The calorimeters work (in a broad sense) by encouraging the particle to interact in a way that induces a shower of particles, and then measuring the energy of the shower. Both calorimeters in ATLAS are sampling calorimeters, and so are made up of alternating layers of "absorber" material, which induces a shower when particles interact with it and eventually absorbs the shower particles, and "active" material, which measures the shower particles as they pass through. An image of the entire calorimeter system can be seen in figure 2.7.

2.2.3.1 Electromagnetic Calorimeter

The Electromagnetic Calorimeter uses the same technology throughout its η range of $|\eta| < 4.9$; alternating layers of liquid Argon (LAr) as the active material and Lead as the absorbing material. These layers are arranged in an "accordion" geometry to provide a system with no gaps in ϕ. The LAr calorimeter is made up of different modules, each with 3 layers. The innermost layer, layer one, is made up of thin,

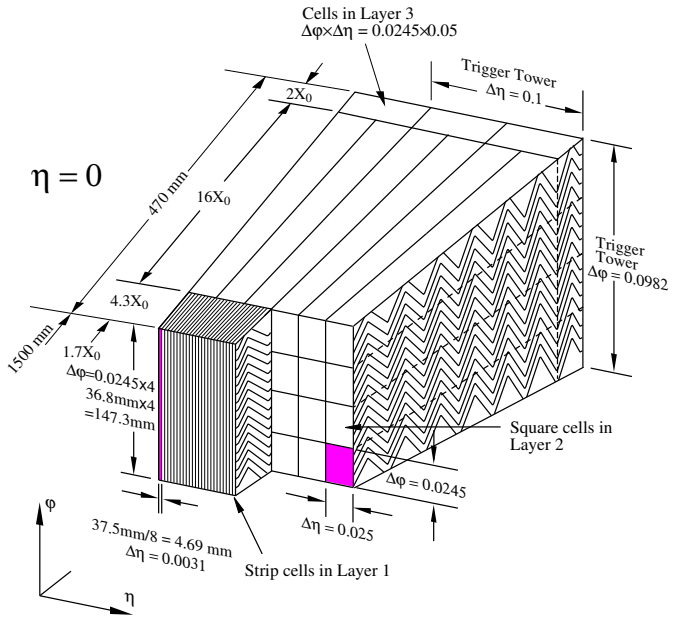

Figure 2.8: Sketch of an ECAL barrel module, showing the different layers. The granularities of the cells in η and ϕ is shown.

strip-like cells which provide good precision in η. Layer two is then made up of square cells in order to collect the majority of the electromagnetic shower. Finally, layer 3 is only expected to deal with the tail of the EM shower, so is made up of coarser cells.

Figure 2.8 shows the cell layout of the ECAL, across one "trigger tower". These 0.1×0.1 ($\eta \times \phi$) towers are used in the reconstruction and trigger algorithms of the calorimeter. In these algoritms the information from one tower is combined with that from its neighbours to form topological clusters that are used in the reconstruction of physics objects.

2.2.3.2 Hadronic Calorimeter

The Hadronic Calorimeter in the barrel uses a tile calorimeter made up of steel as the absorbing medium and plastic scintillator tiles as the active medium. This is split into a barrel section ($|\eta| < 1.0$) and two extended barrel sections ($0.8 < |\eta| < 1.7$). These are then made up of 64 azimuthal modules, each again split into three layers.

In the endcaps ($1.5 < |\eta| < 3.2$), the Hadronic Calorimeter uses LAr technology. This change from the barrel hadronic calorimeter is chosen due to the increased radiation hardness needed close to the beam line. This consists of two wheels in each endcap, just behind the ECAL system. Each wheel consists of 32 azimuthal modules.

2.2.3.3 Forward Calorimeter

The forward calorimeter covers the pseudorapidity range of $3.1 < |\eta| < 4.9$ and completes the calorimeter system, capturing particles at angles close to the beam line. It consists of three LAr layers in each endcap: one made with copper to be used for EM measurements and two made with tungsten to make hadronic measurements.

2.2.3.4 Performance

With the combination of the ID and the calorimeters, ATLAS can reconstruct jets, electrons and photons. The reconstruction of jets and electrons is important to the analyses of leptonic Higgs decays, as electrons appear in some of the final states and jet kinematics are used in the event selection. Photons are not so important to the leptonic analyses discussed in this thesis so their reconstruction is not covered in great detail here. A detailed description of photon reconstruction in ATLAS can be found at [23]. The photon identification process involves two steps. First, the deposits in the electromagnetic calorimeters are searched for photon candidate clusters. These candidates can be matched with tracks in the inner detector as electrons may be produced from the photon via pair production, but this is not essential for a photon candidate. Once clusters have been identified, an algorithm is used to identify them as photons.

The reconstruction of electrons proceeds in four steps, starting with seed-cluster reconstruction. In this step, longitudinal towers of dimensions $\Delta\eta \times \Delta\phi = 0.025 \times 0.025$ within the electromagnetic calorimeter containing a transverse energy of at

least 2.5 GeV are sought. A clustering algorithm is then used to form clusters from these seeds, removing any duplicate clusters in the process. This algorithm reconstructs clusters with a 95% efficiency for 7 GeV clusters, increasing to more than 99% at 15 GeV.

The second step of the reconstruction process is track reconstruction. This differs from the general reconstruction, as tracks that cannot be reconstructed with the standard pion-like energy loss assumptions are re-attempted with larger energy loss assumptions corresponding to electrons. All the reconstructed tracks are then fit as usual, using either a pion or electron hypothesis, depending on which energy loss assumptions they were reconstructed under. In the third step, the electron specific track fit, the reconstructed and fitted tracks are loosely matched to the reconstructed EM clusters based on their η and ϕ coordinates. The tracks that match with a cluster, as well as have at least 4 precision hits within the inner detector, are re-fit using a process that takes into account bremsstrahlung effects.

The last step is the electron candidate reconstruction. This step determines the final variables of the candidate that are sent into the identification algorithms. Firstly, each of the re-fit tracks is again matched to an EM cluster. In the case of clusters which are matched with several tracks, a primary track is defined using an algorithm based on track to cluster distance, the number of hits in the pixel detector and the presence of a hit in the innermost silicon layer of the tracker. Clusters not matched to a track are assumed to be photons. Finally the energy of the electron candidate is determined from the energy of the cluster, and the ϕ and η coordinates are determined from those of the matched track.

Identification algorithms are then applied to the electron candidates to determine their quality. These algorithms use variables based on calorimeter shower shapes, information from the TRT, quantities related to the cluster-matching, track properties and variables related to bremsstrahlung effects in their decision making. In addition, the hits in the IBL are also used in Run II analyses. The full list of variables used is available in [24]. The ID algorithm used is a likelihood based multi-variate

analysis (MVA). The likelihood of a particular candidate being signal (an electron) or background (a jet, converted photon etc.) is defined as

$$\mathcal{L}_{S(B)}(\bar{x}) = \Pi_{i=1}^{n} P_{S(B),i}(x_i), \tag{2.7}$$

where P_S and P_B are probability density functions and $\bar{x}$ is the set of all the discriminating variables. The probability density functions used for the likelihood are obtained from data. These likelihoods are then used to calculate a discriminant

$$d_{\mathcal{L}} = \frac{\mathcal{L}_S}{\mathcal{L}_S + \mathcal{L}_B}. \tag{2.8}$$

Three working points, loose, medium and tight are defined for the electron candidates, each with a different requirement on $d_{\mathcal{L}}$. This is deliberately constructed so that the tight category is a sub-set of the medium category, which is itself a sub-set of the loose category. The efficiencies of the three working points, as well as the rates of misidentification, are shown in figure 2.9. At an E_T value of 25 GeV the efficiency ranges from 90% to 78% from loose to tight, and increases with E_T, due to optimisation of the working points in different E_T bins.

Electron selection also uses so-called isolation variables, which use the energies of particles surrounding the electron candidate in order to distinguish between isolated electrons and non-isolated electrons. This is beneficial as isolated electrons are more likely to come from the decays of high mass resonances, while non-isolated electrons are more likely to come from processes such as pair production or hadron decays, or to be misidentified hadrons. There are two discriminating variables used for isolation requirements: $E_T^{cone0.2}$ in the calorimeter and $p_T^{varcone0.2}$ in the tracker. $E_T^{cone0.2}$ is defined as the sum of the transverse energy of topological clusters contained within a cone of $\Delta R < 0.2$ around an electron candidate cluster. A rectangle of dimensions $\Delta\eta \times \Delta\phi = 0.125 \times 0.175$ is subtracted from the cone, and corrections are applied to account for energy leakage, pile-up and the effects of the underlying event. $p_T^{varcone0.2}$ is defined as the sum of the p_T of all tracks within a cone of size $\Delta R = 10$ GeV$/E_T$, down to a minimum of $\Delta R = 0.2$, excluding tracks associated with the electron.

Both of the discriminating isolation variables are normalised by E_T, and then working points are defined either to target a particular efficiency, or as simple cuts on the variables themselves. The efficiency of a fixed cut working point, "FixedCut-Loose" is shown in figure 2.10. A complete description of electron identification and isolation in ATLAS can be found at [24].

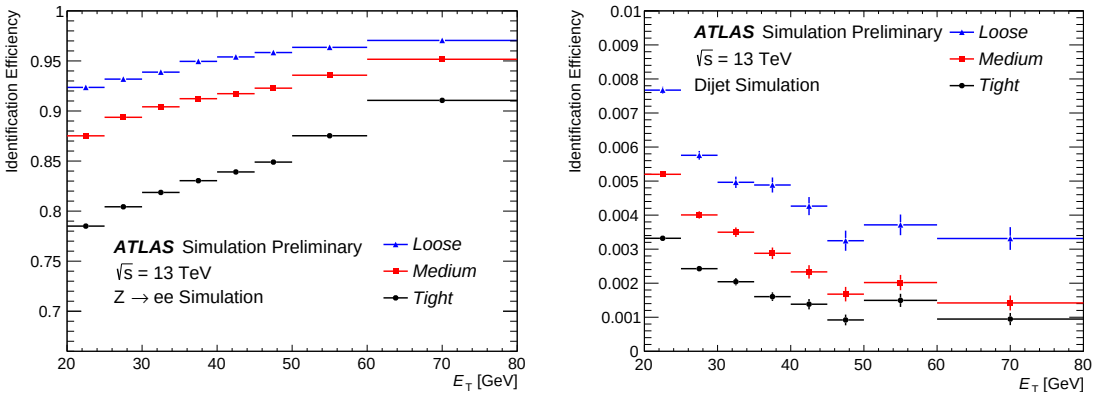

(a) (b)

Figure 2.9: The efficiency to identify (a) electrons from $Z \to e^+e^-$ decays and (b) hadrons as electrons (background rejection) estimated using simulated dijet samples for the loose, medium and tight working points. Figures taken from [24].

Hadrons in the ATLAS detector are reconstructed as jets, which are cones of detected particles from a particle shower. Many algorithms are used for jet reconstruction, but the most common, and the one used here is the anti-k_T algorithm [25]. For reconstructed jets, ATLAS also uses various algorithms to identify, or tag, jets which may contain a b or c hadron. These algorithms utilise many different pieces of information from the jets, including p_T, impact parameters and the existence of any secondary vertices, and their working points are typically defined in terms of the overall identification efficiency. These algorithms are very important for the $H \to b\bar{b}$ and $H \to c\bar{c}$ analyses for example, but are also used in a large range of analyses as b and c hadrons form part of many different signals and backgorunds. A more complete discussion of jet reconstruction at ATLAS can be found in [16].

Excluding noise, the energy resolution of the calorimeters can be empirically de-

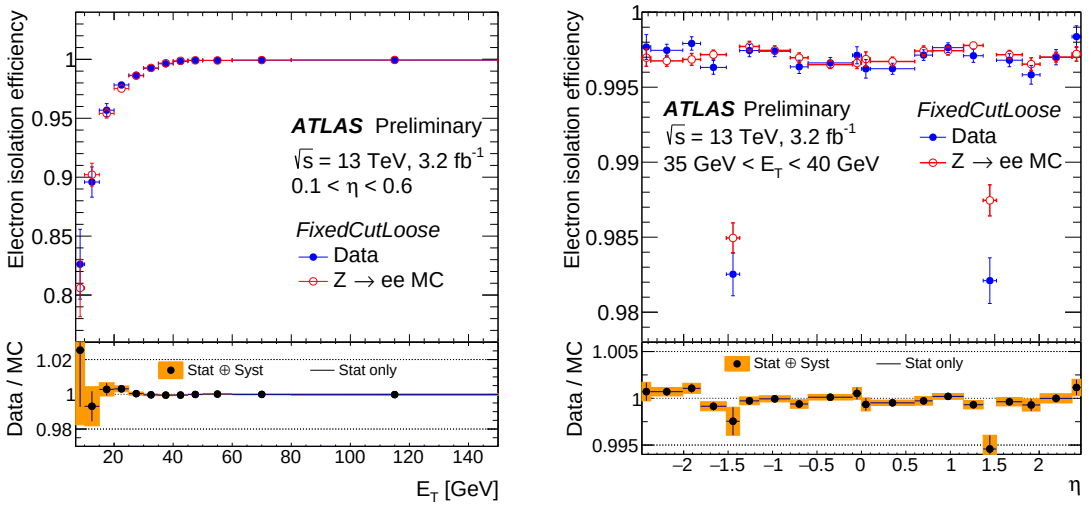

(a) (b)

Figure 2.10: The efficiency of the "FixedCutLoose" isolation working point, shown (a) as a function of E_T at values of $0.1 < \eta < 0.6$, and (b) as a funtion of η at values of $35 < E_T < 40$ GeV. Figures taken from [24].

scribed using the expression

$$\frac{\sigma(E)}{E} = \frac{a}{\sqrt{E}} \oplus b, \tag{2.9}$$

where a is a stochastic term, and b is a constant which represents non-uniformities within the calorimeter. A fit of the energy resolution in the electromagnetic calorimeter found values of $10\% \cdot \sqrt{\text{GeV}}$ for a and 0.17% for b. Likewise, in the hadronic calorimeter values of $a = (21.4 \pm 0.1)\% \cdot \sqrt{\text{GeV}}$ and a b compatible with 0 were found in the endcap and values of $a = (56.4 \pm 0.4)\% \cdot \sqrt{\text{GeV}}, b = (5.5 \pm 0.1)\%$ were found in the barrel. The data for these fits was collected using a test-beam setup with proton beams from the SPS [14].

2.2.4 The Muon Spectrometer

The muon spectrometer is the outer layer of the ATLAS detector and is used to detect and track any charged particles that escape the confines of the calorimeters. In the majority of cases, these particles will be muons. This subdetector is housed within the toroidal magnet system described in section 2.2.1 in order to provide

combined transverse momentum measurements along with the inner detector, and consists of 3 barrel layers and 3 layers in each endcap. Within the detector there are two main sets of detectors: fast detectors used for triggering in the range of $|\eta| < 2.4$ and more precise detectors used for tracking in the range of $|\eta| < 2.7$. A cut-away view of the whole muon system can be seen in figure 2.11.

Within the tracking part of the muon spectrometer, two technologies are employed: monitored drift tubes (MDTs) are used for high precision tracking throughout and cathode strip chambers (CSCs) are used in the inner layers of the endcaps ($2.0 < |\eta| < 2.7$). The CSCs have lower precision than the MDTs, but are used in this area as they can provide $\eta - \phi$ coordinates at a high rate and with good time resolution, so they are suitable for the high background rate close to the beam line.

The triggering in the detector also uses two technologies: resistive plate chambers (RPCs) in the barrel and thin gap chambers (TGCs) in the endcaps. Both of these technologies are chosen for their fast responses (around 1.5 ns in the RPCs and 4 ns in the TGCs [26, 27]), which is required for the trigger system.

2.2.4.1 Performance

Muon reconstruction is performed using information from both the inner detector and the muon spectrometer, although in some cases the calorimeters are used as well. A general overview of the reconstruction is given here, but a more detailed description can be found in [28]. Initially, four types of muons are identified, each one defined by the combination of subdetectors used in its measurement:

- **Combined (CB)** muons are the type with the lowest mis-identification rate. This type of muon is reconstructed as one large track combining hits in both the ID and the MS.

- **Segment-tagged (ST)** muons are reconstructed from an ID track which is extrapolated to match with a single hit in the MS. In this case the parameters

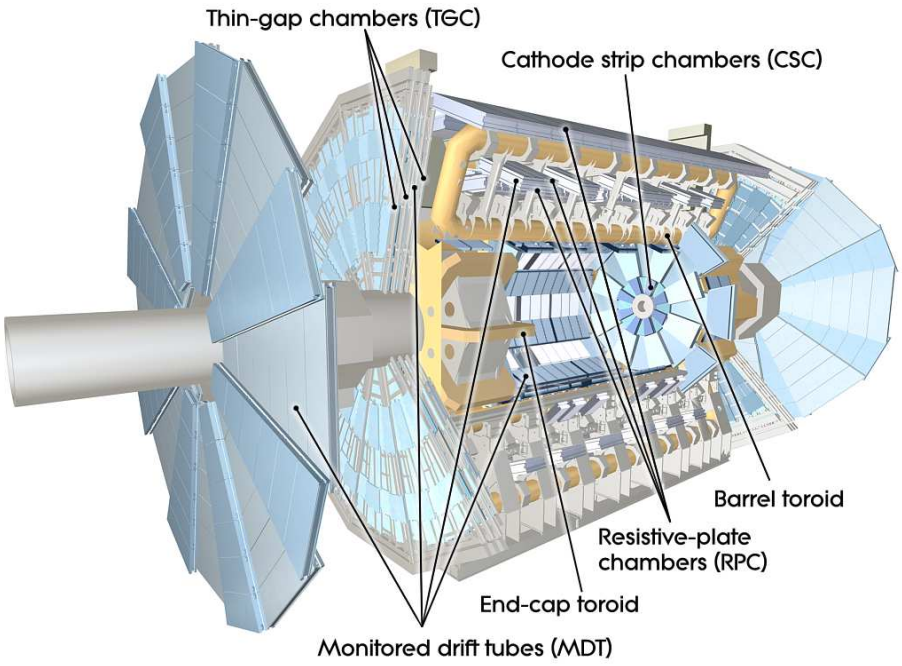

Figure 2.11: Computer generated cut-away view of the muon spectrometer and toroid system [14].

of the muon are chosen to match those of the ID track. This type is designed to find low-p_T muons which may not interact with all layers of the MS.

- **Calorimeter-tagged (CT)** muons have the highest mis-identification rate of the four types of muon. These are reconstructed from an ID track, extrapolated to match with a calorimeter deposit which is found to be consistent with a minimum-ionising particle.

- **Extrapolated (ME)** muons are reconstructed solely from a track in the MS. Muons of this type require that the track is extrapolated to originate from the interaction point. They also require for the track to have hits on two MS layers in the barrel region, or three MS layers elsewhere in the detector. The track parameters used here are from the extrapolated track, allowing for estimated energy loss in the calorimeters. This is used in the case of low quality ID tracks.

All four types of muon are exclusive, i.e. no one muon candidate is shared be-

tween two types. When two muon candidates share one ID track, the candidate of the combined type has highest priority, followed by segment-tagged and then calorimeter-tagged. When a muon can be defined as a different type based on multiple MS tracks, the track with the highest quality is used.

Identification algorithms are then used to select muons from the sorted candidates. In ATLAS, four working points are used for muon identification:

- **Loose** is the working point with the highest efficiency, but is also the least pure. This working point uses all four types of muon candidate.
- The **medium** working point uses just CB and ME muon candidates. This is the standard working point used in most ATLAS analyses, so is designed to cut down on systematic uncertainties due to reconstruction and calibration as much as possible. This working point also includes a requirement that the ID and MS tracks are consistent, which reduces the misidentfication rate further. Identification efficiencies for this working point can be seen in figure 2.12.
- The **Tight** working point is designed to maximise purity, and so has the lowest efficiency. This working point only uses CB muons with hits in at least two layers of the MS.
- The final working point is **high-p_T**. This working point is designed to choose muons with the best p_T resolutions at momenta greater than 100 GeV, and uses only medium CB muons with hits in three or more layers in the MS.

Unlike the muon types, the loose, medium and tight working points are inclusive, so the loose group contains muons from the medium group which contains muons from the tight group.

Similarly to electrons, muons have isolation variables defined in order to select particles likely to originate from the decays of heavy resonances. Two different isolation variables are used for muons. The first is the sum of the p_T of all the tracks inside a cone around the muon. This cone has a variable size of $\Delta R = \frac{10\text{GeV}}{p_T^\mu}$ up to a

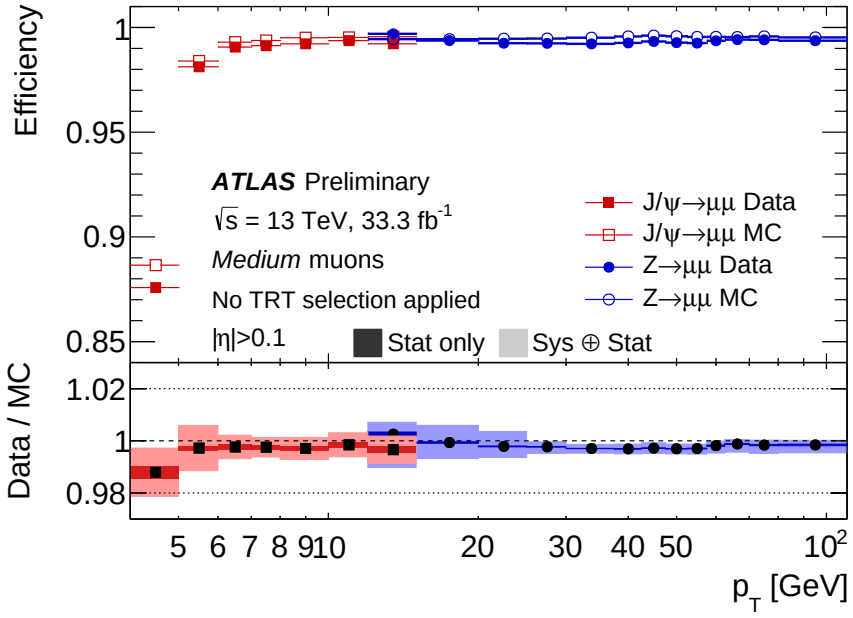

Figure 2.12: Measured identification efficiency for medium muons using data and Monte Carlo [29].

maximum size of $\Delta R = 0.3$. The second variable is based in the calorimeter and is the sum of the transverse energy E_T of all the topo clusters within a cone of fixed size ($\Delta R = 0.2$) around the muon.

In general the momentum resolution of the muon spectrometer can be expressed as the quadrature sum of three terms:

$$\frac{\sigma p_T}{p_T} = a \oplus b \cdot p_T \oplus \frac{c}{p_T}, \tag{2.10}$$

where the a term represents the effect of multiple scattering in the path of the muon, the b term represents the intrinsic resolution of the detector and the c term represents the effect of fluctuations in the energy loss of muons within the calorimeter system. The energy loss term c is thought to be negligible, while the multiple scattering a term is found to have values between 0.015 and 0.025, and the resolution b term has values between 0.08 and 0.2 TeV^{-1} [28].

2.2.5 The Trigger System

The LHC produces a very high rate of pp collisions at the ATLAS detector, and so current read out technology is incapable of dealing with the huge amount of data. In response to this, a trigger system is used, designed to reduce the read out rate to around 1 kHz [30] by identifying which events are interesting physics events. The trigger system in ATLAS consists of two main components: a hardware based level one (L1) trigger that makes fast decisions about every event, and a software based high level trigger (HLT) which uses information from the L1 trigger to make decisions about which events to eventually record. A schematic of the structure of the ATLAS trigger system can be seen in figure 2.13, and a full description of the Run-II trigger system can be found at [30].

The L1 trigger combines information from the muon spectrometer and the calorimeters. The input data stream to L1 has a rate of 40 MHz, and the L1 reduces this to around 100 kHz, and decisions need to be made within an interval of 2.5 μs, in order to prevent the data pipelines from overflowing. The level one calorimeter (L1Calo) and muon (L1Muon) trigger systems feed information to a topological trigger (L1Topo), which uses this information to make decisions based on topological calculations, for example using transverse mass calculations for a W boson trigger. This system, as well as L1Calo and L1Muon, sends information to a central processor (CTP) which makes the final L1 decision and, if a trigger has been fired, sends an accept signal to the various sub-detectors of ATLAS, so that they read out their data. This data is cached together as an event, while the decision of the HLT is awaited. The L1 trigger also defines regions of interest (ROIs) for accepted events, which are the areas of the detector surrounding the interesting particles of the event. The size of the ROIs is dependent on the specific trigger, for example an EM trigger could use a group of trigger towers in the electromagnetic calorimeter layer.

The software based HLT takes the data from the readout of the detector within the ROIs defined by L1 and performs some basic object reconstruction in them, in

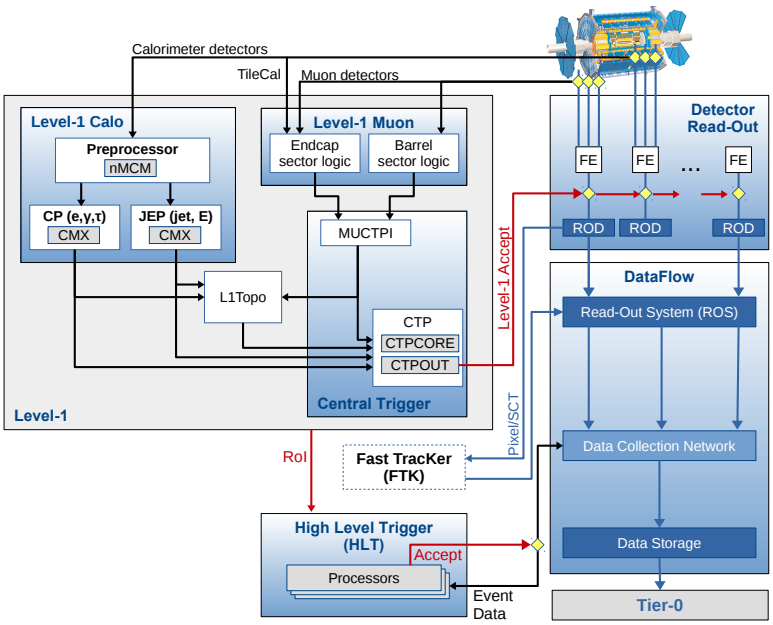

Figure 2.13: Schematic diagram of the trigger and data acquisition (TDAQ) system of the ATLAS detector [30].

order to apply more stringent cuts than in the L1 trigger. The criteria in the HLT are defined by a menu of approximately 2500 different "chains". These chains can be made up of criteria on a single object, such as requiring an electron with high p_T, or can be based on multiple objects. Many of the chains are reasonably generic, allowing them to be used for many different physics analyses, but some more specific chains are also included in the menu. Typically, a balance needs to be found between loose criteria with high efficiency, in order to record as many interesting events as possible, and more stringent criteria, in order to reduce the trigger rate further. In total, the HLT reduces the L1 rate of 100 kHz to a final trigger rate of around 1 kHz.

2.2.6 Simulation

In physics analyses at the ATLAS experiment, an important step is the precise simulation of pp collisions, including all the resultant particles of an event, as well as their interaction with the detector. A number of different event generation programs are used, each of which uses Monte Carlo (MC) simulation to parameterise the events. Each of these programs comes with several pre-defined sets of parameters for different physics processes. The same programs can be used to simulate hadronisation, parton showering and the underlying event, although sometimes separate programs are used for the different processes.

As the protons are not fundamental particles, we must use parton distribution functions (PDFs) to parameterise their structure when simulating events. More detail on the use of PDFs is given in section 5.1. This is of particular importance when calculating the cross section of a particular process, which is computed using an integral over the PDFs:

$$\sigma_{pp\to X} = \Sigma_{i,j} \int_0^1 \int_0^1 dx_1 dx_2 f_i(x_1, Q^2) f_j(x_2, Q^2) \times \hat{\sigma}_{ij\to X}(x_1, x_2, Q^2), \tag{2.11}$$

where f_i and f_j are the PDFs for partons i and j, given a proportion x_1 or x_2 of their respective proton, Q is the energy scale of the interaction, and $\hat{\sigma}_{ij\to X}$ is the cross section for the collision of those two partons. Several different models for PDFs are available for use in Physics simulations. For the analyses presented in this thesis, the PDF4LHC15 [31] set of PDFs is most relevant, as it is used in the simulation of the largest signal process of the Run-II $H \to e^+e^-$ analysis. This PDF set is based on a statistical combination of the CT14 [32], MMHT2014 [33] and NNPDF3.0 [34] PDF sets, each of which mainly uses data from the electron-proton collider HERA [35] to calculate the PDFs.

Pile-up is accounted for in the simulation through the generation of Monte Carlo events for the various pile-up processes. These events are overlaid onto the signal events at a rate chosen to match the rate of pile-up in the data. In order to reduce

the resources used generating these pile-up events, events are re-used in different Monte Carlo samples.

Following this simulation, the generated events are passed through a detailed simulation of the ATLAS detector, using the GEANT4 simulation toolkit [36, 37]. This simulation includes the entire geometry of the detector, as well as the material composition of the various sub-detectors, in order to accurately simulate the interaction between the particles and the detector. The output of this simulation is then reconstructed in the same way as real data. In order to save on computing costs, a faster simulation known as Atlfast-II is used for some analyses [38]. This combines full GEANT4 simulation in the ID and MS with a faster parameterised solution to model the calorimeters. Copies of the generated events before any detector simulation is applied are also kept, for so-called truth level analysis.

As no simulation is perfect, there will be inconsistencies between MC events and data. These inconsistencies are measured through comparison between measured data and expected results from MC, and are then accounted for in analyses through the use of scale factors and systematic uncertainties.

2.2.7 The Phase-I Upgrade

Run-II of the LHC ended in December 2018 and, at the time of writing, the LHC and its experiments are currently undergoing upgrades in order to increase their luminosity capacity for Run-III. In ATLAS, new forward detectors are being built and general upgrades are being performed to improve performance conditions under higher radiation levels and to account for the higher data rate. In addition to this, new tracking and trigger devices are being added to the forward region of the muon detector, in a "new small wheel". The aim of this is to create a sharper trigger threshold and to improve track reconstruction for muons under the higher expected backgorunds [39].

The level one calorimeter trigger (known as L1Calo) is also undergoing a substantial

upgrade, for which the control systems form the content of chapter 4. An overall decription of this upgrade is given here, although more detailed information can be found at [39, 40]. The main motivation for the L1Calo trigger upgrade is that the current use of trigger towers provides data too coarse to handle the increased pile-up, which would degrade the calorimeter resolution and elongate the trigger's turn-on curve, resulting in the need for higher thresholds for offline p_T. To help alleviate this, the read-out electronics of the LAr calorimeter are being upgraded in order to make finer granularity data available to the trigger system. The L1Calo trigger system must therefore also be upgraded in order to take full advantage of the finer granularity data being made available. The upgrade introduces improved processing, which enables better discrimination between electrons, taus, photons and jets.

The structure of the L1Calo trigger upgrade is based around three new feature extractors (FEXs): the electron feature extractor, the jet feature extractor and the global feature extractor (eFEX, jFEX and gFEX). These are housed in Advanced Telecommunications Crate Architecture (ATCA) [41] shelves, rather than the VME (Versa Module Europa) technology, from WIENER [42] currently used. Each FEX has different inputs and performs different trigger algorithms. They are fed by optical fibres from the LAr, mapped by an optical plant. Each FEX module is also connected to a custom HUB readout board, responsible for readout to the HLT and DAQ systems as well as providing information to the timing, triggering and control (TTC) system. The gFEX does not use a HUB board, as it handles this readout on its own. An overall schematic of this structure can be seen in figure 2.14.

The electron feature extractor has particular focus in chapter 4, so is described here. The function of the eFEX module is to identify features in the LAr cells consistent with electrons, photons or tau particles. This is done over a series of four Field Programmable Gate Arrays (FPGAs), and the results are then sent to L1Topo. The results are also stored temporarily in a rolling memory module, which upon receiving a level one accept (L1A) copies the results to a read out module on the Hub. A diagram showing this path can be seen in figure 2.15.

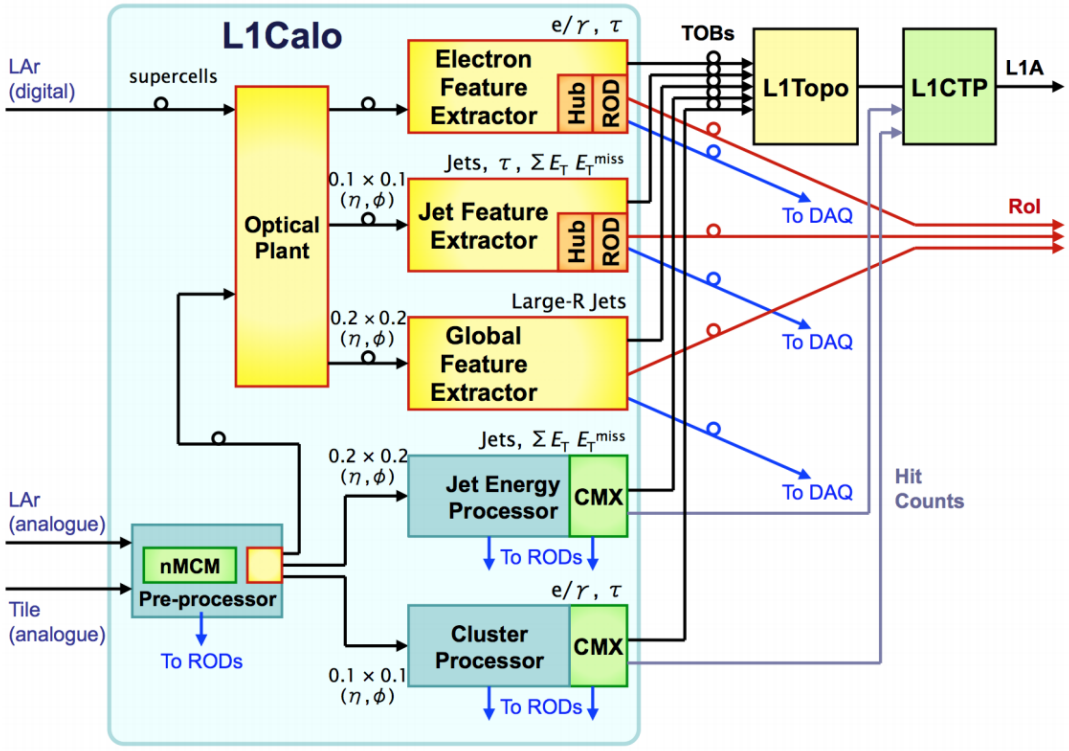

Figure 2.14: Schematic diagram of the phase-I upgrade to the L1Calo trigger system. The green components are components included in the original Run-II system, while the yellow components are those added for Run-III [40].

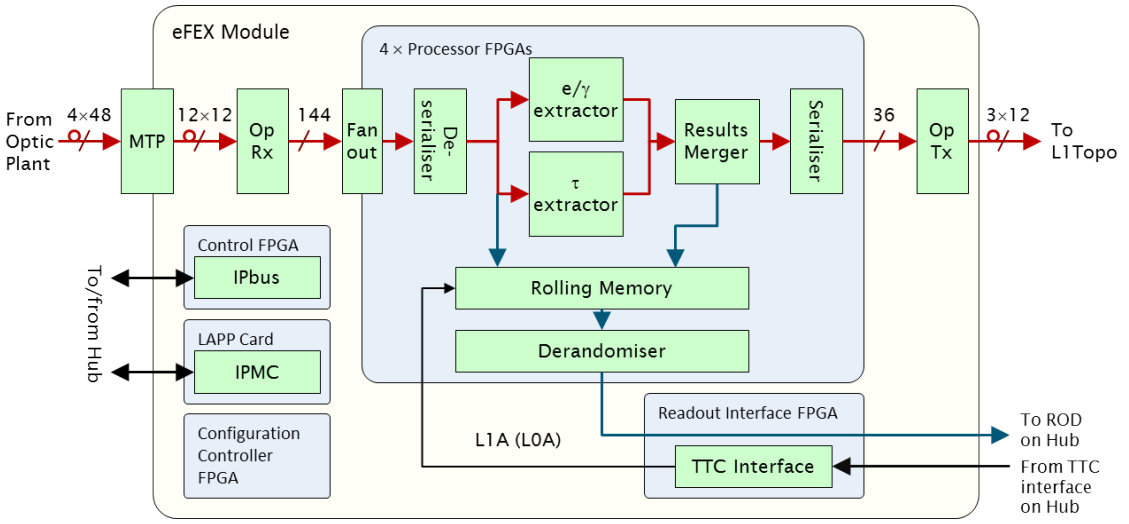

Figure 2.15: Block diagram of the eFEX module, showing the real-time (red) and read out (blue) data paths [39]. IpBus and IPMC refer to communication protocols discussed in chapter 4. LAPP refers to the Laboratoire d'Annecy de Physique des Particules, who originally designed the IPMC card for the system, although an in-house built card from CERN has been employed since the production of this figure.

2.2.8 The Phase-II (High Luminosity) Upgrade

Following Run-III, there is another upgrade planned in order to prepare for running with the HL-LHC. For this run, the ATLAS detector needs to be able to cope with the LHC parameters described in section 2.1.1, in particular the instantaneous luminosity of up to 7×10^{34} cm^{-2}s^{-1}, and the corresponding average pile-up of $< \mu >= 200$. This requires some large upgrades, most notably in the inner detector and in the trigger system. A full description of the planned upgrade can be found at [43].

The high luminosity of the HL-LHC will substantially increase the occupancy in the TRT to beyond 100%, severely compromising its performance. In addition to this, the two silicon components will be reaching the ends of their lifetimes, 700 fb^{-1} for the SCT and 400 fb^{-1} for the pixel detector, so the best option for the upgrade is a complete replacement of the entire inner tracking system. The proposed design is an all silicon tracker covering an η range of $|\eta| < 4$, using pixels close to the beam line for precision measurements [44] complemented by a strip system further out

[45]. This layout can be seen in figure 2.16. Simulation studies have shown that the new layout would maintain current performance standards in the high pile-up environment of the HL-LHC [46].

Extrapolating current trigger rates to the HL-LHC, and maintaining current trigger thresholds, the level one trigger system would need an accept rate of at least 500 kHz, as opposed to the 100 kHz rate currently supported. The proposed upgrade to reach this requirement is to a two step hardware trigger. The first level, level 0, will be based on the current level one trigger, with an accept rate of at least 500 kHz. The second step will be a new level one system which can reduce that rate to 200 kHz, using information from a new track based trigger. Due to the higher accept rates, the readouts of all detectors will need to be upgraded in order to improve their bandwith [43].

The large amount of data generated by the HL-LHC will also require improvements to offline software by ATLAS, both in terms of faster simulation of events, and faster running analysis software. Research is being undertaken on how to improve the computing speed of these processes, for example the use of multi-threaded processing with multicore CPUs is being investigated for Run III and beyond.

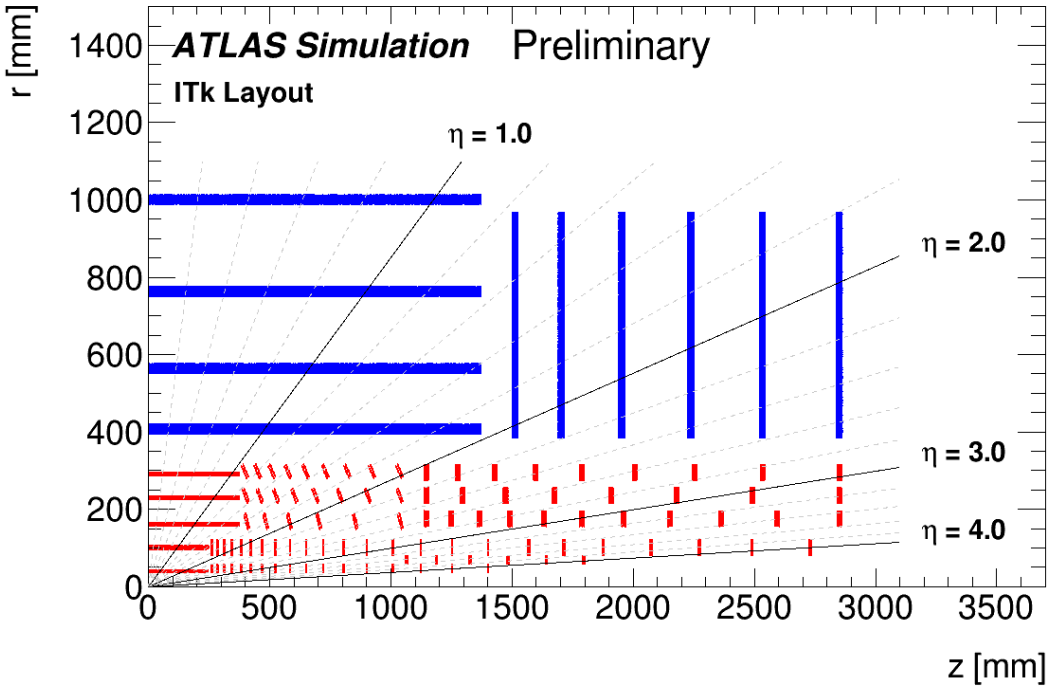

Figure 2.16: Plan for the proposed Phase-II upgrade of the inner tracker. Pixel detectors are shown in red, while strip detectors are shown in blue [46].

Chapter 3

The Detector Control System at ATLAS

3.1 The ATLAS Detector Control System

The ATLAS detector consists of ten main sub-detector systems, in addition to other types of hardware such as the trigger system and the magnet system, each with its own internal hardware structure, which need to be controlled and monitored concurrently in order to efficiently record data. In order to do this safely, all the hardware must be controlled remotely, due to the hazardous nature of the experimental caverns. To achieve this goal, the LHC experiments use a Detector Control System (DCS). This system monitors many parameters of the detector hardware, such as power supply voltage or temperatures of the various components, and allows some control of the incorporated modules.

During Physics runs, the detector is controlled by a team of shifters with a broad knowledge of the various sub-detectors, however many shifters will have limited experience with the inner workings of subsystems outside of their field of expertise. The DCS must therefore provide a clear control interface that simplifies the role of the shifter. The DCS can also create warnings of potential problems so that the shift crew may take action to prevent issues such as loss of data within an event or the failure of trigger systems. Finally, the DCS needs to archive data from the

hardware, which can then be used to diagnose issues after the fact, or in offline analyses [47].

However, the DCS is not solely responsible for the safety of users and machines. While the DCS monitors and reports issues that could lead to damage to the ATLAS equipment, allowing users to take steps to alleviate them, more immediate or severe threats to safety are monitored by the separate Detector Safety System (DSS). The DSS creates alarms and protocols for such events including, where aprropriate, automatically sending information to authorities such as the CERN fire brigade [48].

3.2 DCS Software

The DCS at ATLAS (and at other LHC experiments) is created using one software package for consistency between the different sub-systems. The software chosen for the task is the SIMATIC WinCC Open Architecture (WinCC OA) from Siemens [49]. WinCC OA is a supervisory control and data acquisition (SCADA) software package, designed for gathering and analysing data in real time. This package can be used to develop entire control projects and provides a broad range of tools for this purpose, including interfaces for user interface (UI) design and archive management. The WinCC OA package was previously known as PVSS-II, and documentation in this area still occasionally refers to the software as PVSS.

In general, WinCC OA projects function through a collection of variables called datapoints (DPs). Datapoint types (DPTs) are the "classes" of WinCC OA, and can be defined by the user. WinCC OA also contains various pre-defined DPTs, for example to describe a server connection. DPTs can be made up of elements, which can themselves have a user defined DPT or be one of many pre-determined types (for example the standard integer, float, string etc.). Each datapoint, or even individual elements of a datapoint (DPEs), can be configured to read its value from a hardware source. The datapoints can also be read and manipulated by control scripts. These scripts can also be used to display the values of datapoints in a UI, allowing a

user to monitor the hardware. For example, one could define a DPT describing a generic processor, with a float type and a boolean type DPE showing its monitored temperature and its on/off status. Then one could create multiple instances of this type as DPs, with each DP pointing to a different hardware address for the many processors of the system.

Since each LHC experiment is likely to require similar functionality from its DCS, a joint project between the experiments is needed to save the initial work from being repeated unnecessarily. While the foundational work on LHC DCS was performed by LHCb, soon after the Joint Controls Project (JCOP) was founded for this purpose [50]. One issue tackled by JCOP was selecting the WinCC OA package. Another significant contribution of JCOP is the development of libraries of software components within WinCC OA for use by all the experiments, known collectively as the JCOP framework. The framework contains tools which can be used to define Finite State Machines, an important concept which is explained in section 3.4. Also included in the framework is a Device Editor and Navigator, shown in figure 3.1, which displays not only the hardware connected to a system in a tree view but also the structure of any generated Finite State Machines, and an installation tool which allows the user to install the many other framework components [51].

3.3 DCS Structure in ATLAS

In broad terms the ATLAS DCS is split into two layers: the front-end and the back-end. The front-end consists of monitoring hardware, which is responsible for controlling the detector and reading data from the different components. The data is sent to the back-end to be read by the user, and the back-end also sends commands to the front-end. As well as monitoring the detector hardware, the front-end is also responsible for monitoring infrastructure, such as cooling, electronics racks and power. An overview of this structure is shown in figure 3.2.

The DCS back-end collectively refers to the network of rack PCs running the DCS

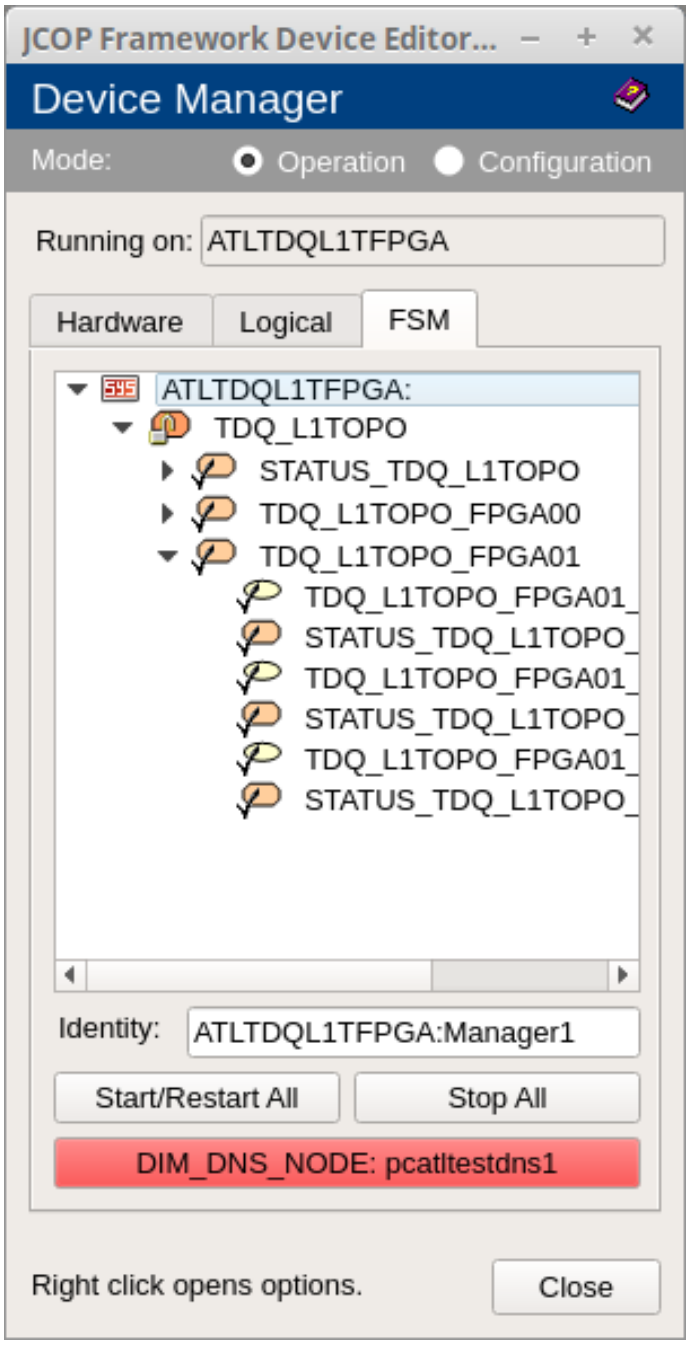

Figure 3.1: The device editor and navigator, a framework tool used to browse datapoints connected to hardware.

software. This layer can be further subdivided into three sub-layers: global control stations, subdetector control stations and local control stations. The global control stations are the highest level of the DCS, and so they provide the main interface between the DCS and the users in the ATLAS control room. They also perform global DCS services, including managing the Alarm System of the detector and communicating with outside systems such as the LHC and the DSS [47].

At the next level down, there are the subdector control stations. These are responsible for representing entire subdetectors (e.g. the pixel detector or the tile calorimeter) in the DCS. For most shifters this is the highest level at which they are given control of the detector, although the DCS desk in the control room can take control of the entire detector. These control stations summarise the individual states of connected local control stations and report the information as the state of the corresponding subdetector.

The subdetector control stations are also responsible for communication between the DCS and the trigger/DAQ system. This allows the TDAQ to send commands to, or receive DCS information from, the detector hardware.

Finally, the lowest level of the DCS is made up of the local control stations, which represent the interface between the DCS and the detector hardware. As such, their main priority is to receive data from the front-end to be read by WinCC OA. They also are required to define an operational state for their correpsonding hardware, and pass this information up the back-end as part of the overall finite state machine (see next section). Requests coming from higher up the back-end tree will be converted by the local control stations to commands, which are then sent via the front-end to the hardware [47].

Each PC in the DCS back-end is responsible for running part of the ATLAS Finite State Machine (FSM). The FSM describes the entirety of the detector, and the purpose of each node is decided by its position in the back-end tree. The use of FSMs in the ATLAS DCS is based on [50].

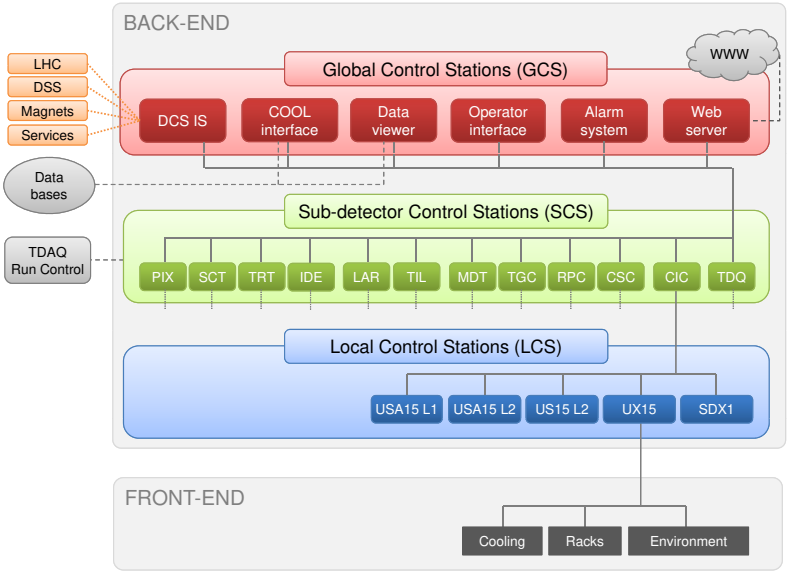

Figure 3.2: ATLAS DCS architecture [47]

3.4 Finite State Machines

The DCS uses FSMs to describe the parts of the detector. An FSM is described by a set of discrete states that describe the state of the associated hardware, for example a power supply could have the states ON, OFF, RAMPING UP, RAMPING DOWN and UNKNOWN. In the ATLAS DCS, each FSM also has an associated status along with its state, which can have one of four values:

- OK - The monitored object lies within expected parameters
- WARNING - The object has a minor fault, to be dealt with within normal working hours
- ERROR - The object has a more serious fault which could affect detector performance
- FATAL - The object has a fault which seriously affects the detector and should

be dealt with immediately

Generally, the state and status of a given FSM are not related, however a given state may restrict the available status options [47].

In the ATLAS DCS, each FSM is linked together via reference to form an FSM tree describing the entire detector. Statuses and states from the leaves of the tree are propagated upwards to help derive the overall state of the detector.

The leaf nodes of the FSM are called Device Units (DUs), and are run on the LCS machines. Each DU represents an item of monitored hardware, and interprets data from the hardware to derive a state. The DUs also interpret user requests into commands which can be sent to the hardware.

The branches of the FSM tree are made up of Logical Units (LUs) and Control Units (CUs). Both of these node types summarise the states of their children in their own state. Nodes are grouped into LUs based on their grouping within the detector, for example different hardware components within one module or different PCs within a rack [50].

Logical Units and Control Units share the same functionality, with the exception that CUs can be taken control of by a user. Taking control of a CU also gives the user control of its children, so they can propagate commands down the FSM branch. Control of the different CUs in the FSM tree can be shared, in a number of different operational modes.

In the main operational mode, the FSM has one owner (during normal running, this is the DCS desk in the ATLAS control room). Only the owner is able to rebuild the FSM or do any development work, however other users are allowed to issue FSM commands. In some cases, an expert may take ownership of particular nodes of the FSM in order to do development work on those specific branches. In addition to this, nodes can be excluded from the main FSM tree, meaning not only can that node no longer be issued commands by any user, but also that the state from the

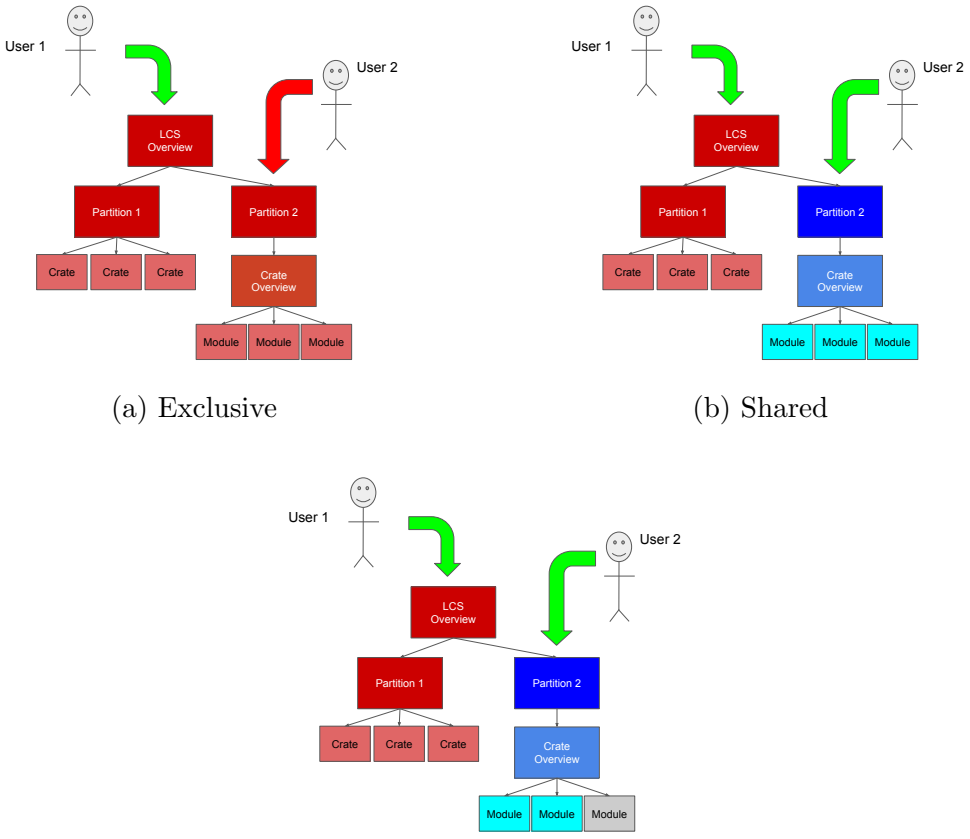

(a) Exclusive

(b) Shared

(c) Excluded

Figure 3.3: Diagrams showing the three main operational modes of CUs. In figure 3.3a, user 1 has exclusive ownership of the entire tree via the LCS CU. In figure 3.3b, ownership of partition 2 is shared between the two users, while user 1 retains exclusive ownership of partition 1. Figure 3.3c shows the same scenario as figure 3.3b, but in this case one of the modules in partition 2 is excluded from the FSM tree.

excluded node is no longer propagated up the FSM tree. These operational modes are summarised in figure 3.3 [52].

3.5 Alarms

WinCC OA provides configuration for monitoring and flagging of individual data-points, via the creation of “alert configs” which can be attached to the DPEs. This

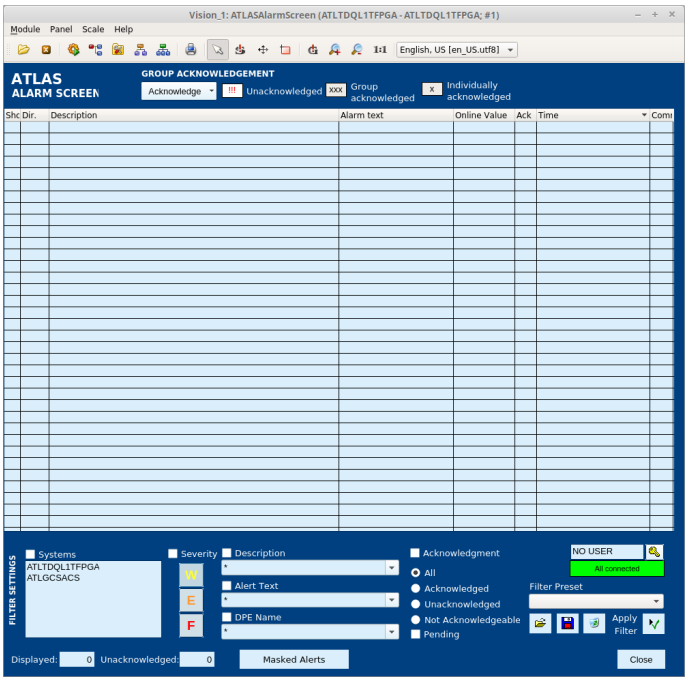

Figure 3.4: The ATLAS Alarm Screen. Alarms attached to specific datapoints are displayed in the large table. This screen also allows the user to view specific information about the alarms, as well as "Acknowledge" them, by clicking on the panel.

configuration uses value ranges for the datapoints, and raises an alarm when the datapoints move outside of these ranges. The different levels for an alarm are the same as the levels used as FSM statuses, in fact the FSM status will usually show the same level as a given alarm, although the alarm system allows more detailed descriptions of the various problem to be given.

WinCC OA also allows summary alarms to be defined. This type of alarm is dependent on other alarms in the system, so that the system does not get congested with many of the same type of alarm. The alarms in ATLAS, and for its individual systems, are summarised in a GUI known as the Alarm Screen, seen in figure 3.4 [47].

3.6 Archiving

The DCS also needs to store datapoint values for later analysis. In ATLAS, this is done by exporting the data into the ORACLE online database. The system uses time and value dependent smoothing to limit the rate at which this data export happens. This involves setting a dead-band whenever a datapoint value is archived. The value must then reach a value outside of this band before it is archived again. However, the dead band is only applied for an alotted period of time, after which the next change in value will trigger it to be archived again.

The online database is designed to only be accessed from within the ATLAS Control Network. However, the archived values may need to be accessed externally for more detailed monitoring. To account for this, the data in the ORACLE online database is exported at regular intervals to the ORACLE offline database, which is externally accessible. In addition to this, data which is needed for offline calibration, reconstruction or analysis is exported to a third database, the Conditions Database [53].

3.7 Security

Security is another important aspect of the DCS. This is because the detector can become compromised through the DCS, either intentionally by bad faith actors or unintentionally by inexperienced users.

The first line of defense is that the network of the ATLAS control room and the detector, the ATLAS Control Network, is kept isolated from the CERN general purpose network (GPN). This means that a security breach in the GPN does not put the ATLAS hardware at risk. A gateway does, however, exist between the two networks, but access to this gateway is only granted to a number of approved users, limiting the number of potential risks.

For the DCS machines, access is only permitted to very specific users. This permission is allocated strictly based on who absolutely needs access, i.e. usually system experts only. Shift operators will not normally need access to these machines.

Access to the DCS in the control room is controlled by the JCOP Access Control framework. In this, the different subsystems of ATLAS are defined to be within specific domains. Then, for each domain, different actions are defined which will require different privileges. These privileges are then assigned to a Role. Users are then assigned to different groups, which define their roles. Under this system, users may only perform actions assigned to the privileges within their role. This allows privileges to be contained within their appropriate domains, for example a user with expert privileges in the TDQ (Trigger/DAQ) domain may only have operator privileges in the PIX (Pixel Detector) domain. The administration of these privileges is performed using a Lightweight Directory Access Protocol (LDAP) [47, 54].

Chapter 4

DCS in the L1Calo Phase-I Upgrade

This chapter is focused on the DCS for the Level-1 calorimeter (L1Calo) trigger, specifically, the eFEX module being introduced in the Phase-I upgrade, and the FTM (FEX Test Module) being used in the testing phase. The details of the upgraded L1Calo trigger are presented in Chapter 2. The following sections present the scope of the DCS project, and describe the technology used in the front-end and back end of the system.

4.1 Requirements and Scope

The L1Calo system consists of eight Advanced Telecommunications Computing Architecture (ATCA) crates, each containing 14 boards which house the different modules of the calorimeter trigger. At the front-end, the DCS project needs to remotely access these crates, and then access the modules therein using both the Intelligent Platform Management Interface (IPMI) [55] and IPBus [56] protocols. The state of this hardware is then reported to the back-end, using "middleware" OPC UA servers. In the back-end datapoints are created using WinCC OA to describe this hardware, and a graphical interface is designed to visually display the state of each module. The user interface is structured via an FSM that summarises the entirety of

the system. This FSM also needs to flag any faults or problems within the system.

The DCS project designed for eFEX also needs to describe the FEX test module (FTM), a module designed for outside of the main L1Calo system, used to test the different FEX modules by sending them simulated calorimeter signals via optical fibre. The FTM is designed for use in the commissioning and testing of the FEX machines, in order to test both their fibre optic inputs and their elctronics. Although FTM modules are not planned to be used during normal Physics running, DCS is required for their use in CERN test facilities. In addition other FEX module DCS systems may use similar concepts to those developed in the eFEX project.

For each module, the DCS must monitor a range of devices, split broadly into three categories. The first category is FPGAs, and both modules employ a number of these for processing and control (five per eFEX and three per FTM) for which the temperature and voltages must be monitored. The second category comprises of the optical miniPOD transceivers, and for these the DCS needs to monitor the temperature and the optical power input/output. The third category concerns power related components, such as the main power supply or various DC-DC converters contained in the modules. For the FTM, these power components are all contained within one component, whereas for the eFEX there are many different components across the board. The quantities to be measured within this category varies from component to component, but in general the temperature, input voltage, output voltage and output current are usually monitored.

The DCS must also be able to monitor signals from the ATCA crates themselves, including the presence of a board in each slot and the power states and error states of those boards. Through the connection to the ATCA crates it must be able to power the modules on and off.

4.2 Front-End

As stated in the requirements, the goal of the front-end is to communicate with the L1Calo hardware, using the ATCA, IPMI, and IPBus protocols. The following sections give an overview of the technologies used.

4.2.1 ATCA

Advanced Telecommunications Computing Architecture is a widely used specification for communication technology developed by PCI Industrial Computer Manufacturers Group (PICMG) [41, 57]. Using the ATCA standard for crates provides the L1Calo modules with several benefits, including redundant 48V power supplies along the backplane of the crate, as well as fully managed fan systems provided for cooling. Each crate contains dual shelf managers, which can monitor and control the boards contained within the crate, as well as the power and cooling systems. It is therefore the role of the shelf managers to implement cooling management, i.e. by adjusting fan speeds, or even to deactivate modules in the case of high temperatures. These shelf managers communicate with the boards via IPMI. The shelf managers act as an itermediary between the DCS and the boards in IPMC communications, whereas IPBus communications are performed directly with the modules. Furthermore, WinCC OA can use Simple Network Management Protocol commands to communicate with the shelf managers and steer the crates. As long as 48V power is provided to the system, the shelf managers can read shelf and module data, even if the modules are inactive. In fact, the modules can have one of eight states within the ATCA infrastructure, of which inactive is one, defined by how the boards are inserted and communication between the board and the shelf. These states are read and interpreted by WinCC, and summarised by three datapoints: present, healthy and powerState. The eight states M0 - M7 are defined in [58]. The redundant operation of two shelf managers, complemented by a hot-swap system for the modules, allows the overall system to run with very low levels of downtime [57].

Table 4.1: Hardware addresses for each slot (in decimal format) in the L1Calo ATCA crates, in terms of the physical slot number, as well as the logical slot number, from which the addresses are derived. These addresses are used in the configuration of the datapoints.

Slot	1	2	3	4	5	6	7	8	9	10	11	12	13	14
Logic #	13	11	9	7	5	3	1	2	4	6	8	10	12	14
H/W Addr.	77	75	73	71	69	67	65	66	68	70	72	74	76	78
I^2C Addr.	154	150	146	142	138	134	130	132	136	140	144	148	152	156

4.2.2 IPMI

Intelligent Platform Management Interface is a standard for setting up monitoring systems independently of local properties such as OS, CPU or firmware. It is also designed to work before the system boots, when it is powered down or in the event of system failure, making it very useful in the context of DCS. An IPMI system consists of a main controller, called the baseboard management controller (BMC), and smaller Intelligent Platform Management Controllers (IPMCs). Each of the IPMCs connects with the BMC via an Intelligent Platform Management Bus (IPMB) [55]. In the L1Calo ATCA crates, each board contains a CERN designed IPMC mezzanine [59] which connects via an IPMB contained within the crate. IPMI is used to monitor the voltages and temperatures of various electrical components across the eFEX boards, such as the power supply and several DC-DC converters, as well as the temperatures of the FPGAs. For the sake of redundancy, the crates run with two IPMBs, IPMB-A and IPMB-B.

The IPMBs themselves are based on the Inter-Integrated Circuit (I^2C) bus protocol [60]. The various temperature, voltage and current sensors are accessed via their I^2C addresses, through which their readings and safety thresholds can be read.

The L1Calo upgrade uses 19-inch width ATCA crates, which have capacity for 14 boards (sometimes referred to as blades) each. The I^2C and hardware addresses for the slots in each crate are shown in table 4.1.

4.2.3 IPBus

IPBus is a simple ethernet-based protocol for monitoring and controlling hardware via its IP address [56]. IPBus monitoring is transactional in nature; the IPBus client begins by sending a "read-request" data packet to the device being monitored, and the device responds with a data packet containing an error code and, if the transaction is successful, the requested data. The same protocol is used for writing to an IPBus device, aside from the detail that the return data packet contains only an error code. In networks containing many IPBus clients and devices, a control program known as ControlHub must be used to mediate the various transactions by buffering the incoming data packets and resetting their IDs [56]. Various components on the eFEX boards are monitored via IPBus, most crucially the input and termination voltages of the FPGAs, the FPGA internal temperatures and the measured optical power at the transmitting and receiving MiniPODs (twelve channel transceivers of fibre-optic signals) as well as the temperatures of those MiniPODs.

4.2.4 OPC UA

Open Platform Communication Unified Architecture (OPC UA, or just OPC) is the middleware that facilitates communication between the front-end and the back-end in the L1Calo DCS. This allows several different communication protocols to be used (such as IPMI and IPBus) on the front-end, while the back-end PCs will only have to communicate with servers using OPC. There are two main advantages to using OPC for communication in this way. The first is simply that WinCC OA contains an in-built system for connecting with OPC servers. The second advantage is more structural: using an OPC server as a middle-man means that when a piece of hardware is changed, only that server needs to be updated, rather than any number of back-end PCs that may be connected to the particular piece of hardware. In the L1Calo eFEX project, two separate OPC servers are deployed: one each for the two communication protocols used.

In the L1Calo system installed at LHC point 1, there will be eight shelves, each housing 14 modules, each containing over 100 sensors. In this case, creating OPC servers by hand to connect to the thousands of different datapoints is unfeasible, so a method of generating the servers based on the available hardware must be employed. For this purpose, QUASAR (**Q**uick OPC **UA** **S**erver gener**A**tion f**R**amework) [61, 62] is used. With QUASAR, a user creates an xml design file, describing the structure of a system as a class hierarchy. One such design, used in this project for IPBus communications, is shown in figure 4.1. QUASAR can then create logic for the devices of the system based on this design, and implement the instances of this logic based on the availability of existing devices. It can then be used to build a server.

For the eFEX project, there are two OPC servers. The first is AtcaOpcUaServer which handles IPMI datapoints from the modules and from the shelves, including shelf managers, power supplies, boards and sensors. The ATCA shelf-related datapoints are probed using underlying Simple Network Management Protocol (SNMP) functions, and the server also has an automatic discovery mode that probes the IPMI datapoints. The other is OpcUAEFEXServer which handles IPBus datapoints from the modules via Python script. As the DCS uses the same IPBus space as the trigger readout, these Python scripts must include an arbitration function in order to prevent interference between the two systems. Both servers are built using QUASAR. A schematic of the entire front-end can be seen in figure 4.2.

4.3 Back-End

As described in section 3.3, the back-end consists of a set of networked PCs running WinCC OA. Within WinCC, datapoints are defined based on the sensor readings available over the OPC servers. Each of these datapoints has an address config defining its connection to the hardware via OPC, as well as an alert config defining the acceptable operating parameters, by default. WinCC is then used to generate an FSM tree based on the existing datapoints, with an in built user interface to

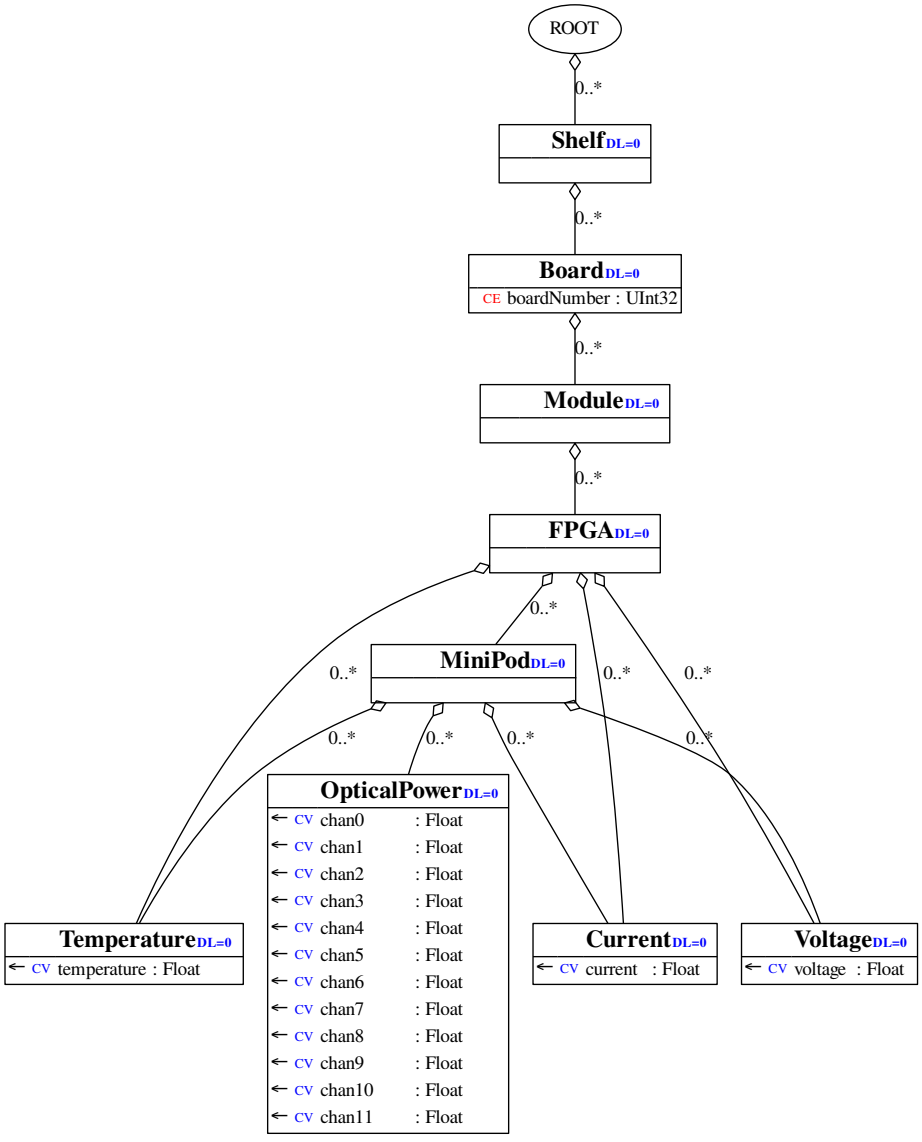

Figure 4.1: Diagram of the class hierarchy for the model used by QUASAR to create the OPC UA server for IPBus communications

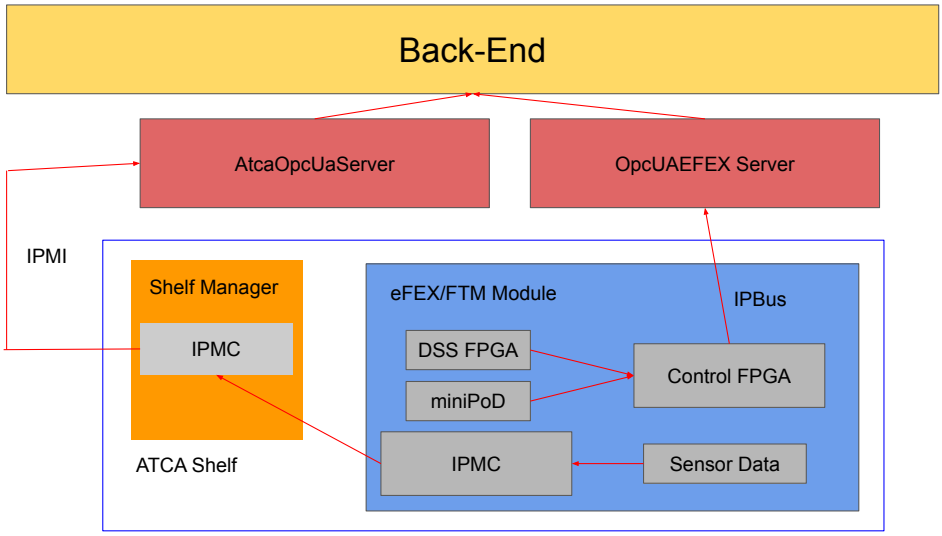

Figure 4.2: Schematic diagram of the DCS front-end

be used in the ATLAS control room. For the components accessed through IPMI, via the ATCA shelf, a framework tool "fwATCA", currently in development within ATLAS, is used to create some of this structure.

4.3.1 Datapoint Creation

In order to create the DPs used by WinCC to access the hardware, an extension to QUASAR called Cacophony [63] is used. Cacophony reads the server design and datapoint addresses from the server's config file, and then automatically creates data structures following the same tree design as the server (for example the class hierarchy shown in figure 4.1) within WinCC OA. In the case of AtcaOpcUaServer, this creates DPTs, and then DPs, describing the shelf itself, the shelf mangers, the boards, the fan trays, the power supplies, the IPMCs and the sensors connected to those IPMCs. Each of the sensor datapoints contains an ID string DPE, identifying the components associated with the sensor, as well as threshold DPEs which are used to define the alert handling configuration of the reading. The ATCA board DPT contains a lot of elements, but for the purposes of this project the most important ones are the powerState, present and healthy DPEs.

Table 4.2: Summary of the aliases used within the eFEX/FTM DCS project. Examples are chosen based on the board in slot 7 of an ATCA shelf, containing an FTM module.

OPC	Datapoint Type	Example Datapoint	Alias
AtcaOpcUaServer	fwAtcaBoard	shelf0/Board7	shelf0/Board7_ATCA
AtcaOpcUaServer	fwAtcaIpmc	shelf0/IPMC130	shelf0/Board7_IPMC
OpcUAEFEXServer	EFexModule	Shelf0/Board7/FTM3	shelf0/Board7_IpBus

The IPBus datapoints are also created using Cacophony. The DPTs are defined based on the classes in figure 4.1, with the DPEs shown. The DP names are structured based on the class hierarchy. A second extension to QUASAR, named Poverty, is used to create Python libraries to operate the server and publish the OPC datapoints.

The servers themselves also need to be represented within WinCC OA, so that problems with the server connections can be distinguished from hardware issues. WinCC connects to the OPC servers using OPC UA clients, and these are represented by DPs of a pre-existing DPT. The most important DPE of this DPT is called connState and represents the state of the WinCC project's connection with an OPC server.

For the ease of use in user interface scripts, some of the datapoints are given aliases. In particular the ATCA DPs for each board and each IPMC, and the IPBus DPs for each module are given an alias, and then by accessing these aliases, scripts can build lists of the datapoints from the lower levels of the class hierarchy. The aliases are chosen to match the names of the FSM nodes, with a suffix added. This is because the FSM provides the names of the nodes to the scripting layer (as so-called $-parameters), allowing for some replication of the user interface design.

4.3.2 FSM

The FSM is the final layer of the DCS project, and is the layer that users in the control room interact with. The entire structure of the FSM tree, including control units and device units, is created by fwATCA and then the behaviour of the device units is configured via script, to depend on the particular devices in each slot. Each device unit has an associated user interface panel, which shows a more detailed summary of the status of the components contained in the board than the status shown in the FSM tree.

4.3.2.1 Control Units

The top node in the FSM tree is a control unit of type FW_ATCA named TDQ_ATCA. Below this, fwATCA defines a control unit type FW_ATCA_SHELF, and creates instances of this control unit to describe each shelf. The shelf control units have the possible states READY, NOT_READY, SHUTDOWN, UNHEALTHY and UNKNOWN, and these states are defined by the states of the contained device units. The top control unit has the possible states READY, TRANSITION, STANDBY, NOT_READY, SHUTDOWN and UNKNOWN, and these states are defined by the states of the shelf control units. These control units are created directly by fwAtca, with standard pre-built states, statuses and panels. The user interface for an FW_ATCA_SHELF control unit is shown in figure 4.3, while a summary of the possible control unit states is shown in table 4.3.

4.3.2.2 Device Units

The device units for the FSM are all contained under the control unit for the shelf. The device units used are of type FWATCABOARD_ATCA_SLOT to describe each board module, type FWATCAPOWERSUPPLY_ATCA_PS to describe the power supplies and type FWATCASHELFMANAGER_ATCA_SHM to describe the shelf man-

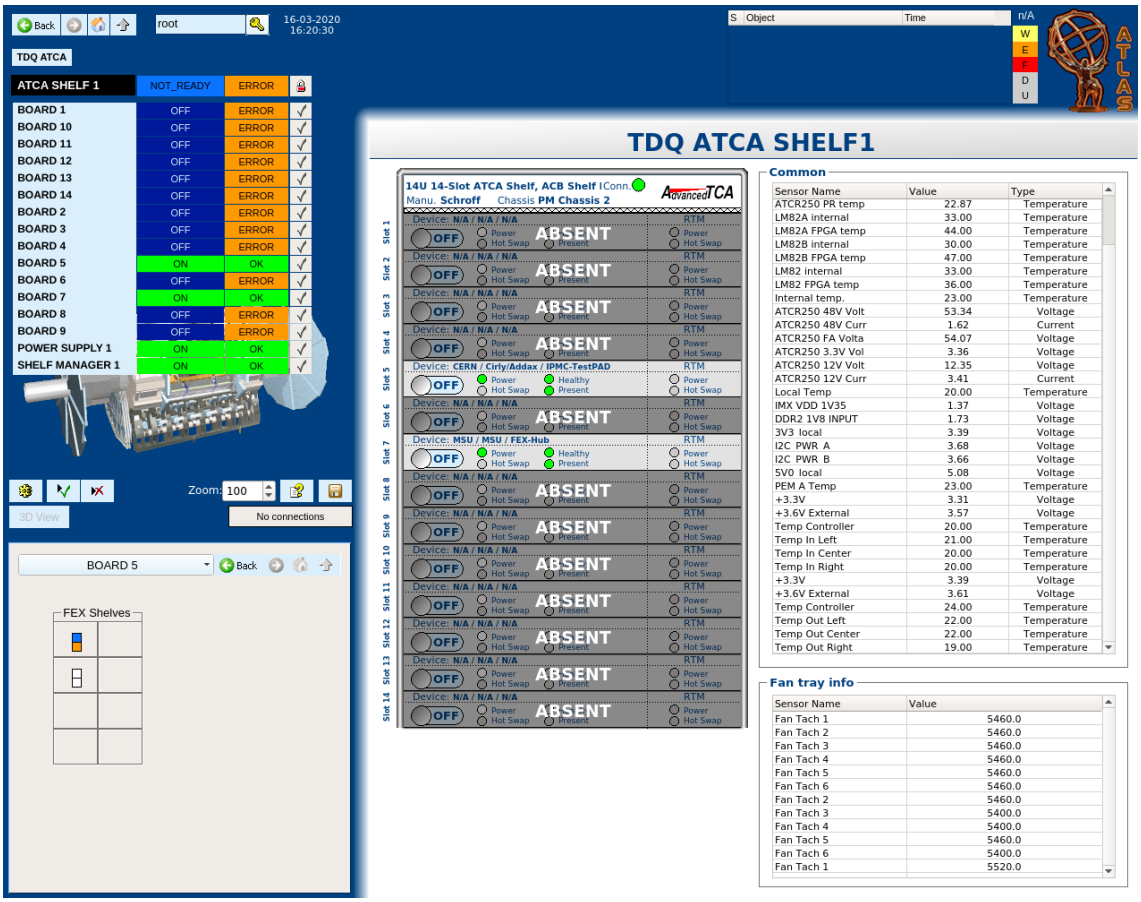

Figure 4.3: FSM view of the top level control node for an ATCA system.

Table 4.3: Summary of the possible states of the FW_ATCA and FW_ATCA_SHELF control units of the FSM.

State	Condition
READY	All children in the state ON, EMPTY, or READY
NOT_READY	Any children in the state OFF, ABSENT, SHUTDOWN or NOT_READY
SHUTDOWN	All children in the state OFF or SHUTDOWN
UNHEALTHY	Any children in the state UNHEALTHY
UNKNOWN	Any children in the state UNKNOWN or all children of the type FWATCASHELFMANAGER_ATCA_SHM in the state STANDBY
TRANSITION	Any children in the state TRANSITION

agers. The full structure of an FSM tree for one ATCA shelf is shown in figure 4.4. The slots and power supplies have the possible states ON, OFF, UNKNOWN, ABSENT and UNHEALTHY, and the slots have an additional state EMPTY. The shelf managers have the possible states ON, STANDBY and UNKNOWN. These states are described in table 4.4. The only command available directly through the FSM is ToggleShouldBePresent, which tells the FSM whether a board is expected in a particular slot. For an empty slot, this command effectively toggles between the ABSENT and EMPTY states. The states and statuses for the power supply and shelf manager device units are again pre-defined by fwAtca, as are their user interface panels.

However, the slot DU types require extra tuning to rely on the various datapoints from sensors on the contained modules. In the FSM functionality this is as simple as passing a list of datapoints through the FSM generation script. The slot DUs also require a new panel, in order to qualitatively describe the overall state of the module in a way that is easy to understand. This panel is designed using the same datapoints that define the FSM states and statuses. The panel itself contains five sub-panels. The first is an information display showing the identity and power state of the board, as well as the connection states of the OPC servers. The second and third sub-panels display the values of specific datapoints, either chosen by the user or picked up when they enter an alert state. The fourth sub-panel is a table showing the value of each datapoint as well as its alert limits. Finally a schematic diagram of the module is shown, to graphically display the temperatures of the various module components. A secondary panel is also shown, showing the status of all the ATCA shelves in the system. A user panel designed for the FTM module is shown in figure 4.5.

In the FSM views shown in figure 4.3 and 4.5, one can see the complete status of an ATCA system. The individual boards in an ATCA crate can be switched on and off using the switches seen in figure 4.3. The info from all the sensors on a module is summarised through its node on the FSM tree, while details of the individual sensors can be seen through the UI panels. Statuses of alerts within the sensors

Table 4.4: Summary of the possible states of the FSM's device units.

State	Description
ON	The device is switched on
OFF	The device is switched off
ABSENT	The device is missing and is expected to be present. This state automatically puts the node in ERROR status
EMPTY	The device is missing, but is not expected to be present
UNKNOWN	The OPC server associated to this device is disconnected, so its condition is unknown. This state automatically puts the node in ERROR status
UNHEALTHY	The shelf manager is receiving an unhealthy signal from the device. This is indicative of a fault in the ATCA communication or hardware, rather than the OPC server. This state automatically puts the node in the WARNING status
STANDBY	The device is in standby. This state only applies to the shelf manager device unit

are shown through both the FSM tree and the alarm screen. Trending graphs of datapoint values are also available through the UI, by rightclicking on the value in the reading panel.

4.4 Conclusion

The L1Calo DCS system is responsible for monitoring the wellbeing of all of ATLAS's running equipment remotely from the ATLAS control room. To this end, the system as described in this chapter has been designed to access the thousands of necessary datapoints and summarise them in a way that can be understood by shifters with little prior knowledge of the upgraded L1Calo system itself. This is done through the combination of an FSM, capable of pinpointing modules on which issues have arisen, as well as a series of user interface panels designed to quickly ascertain what those issues are. The datapoints and FSM are created using a combination of QUASAR and WinCC OA. Following testing over the course of long shutdown 2, this DCS system will be deployed at LHC point 1 for use in Run-III and beyond.

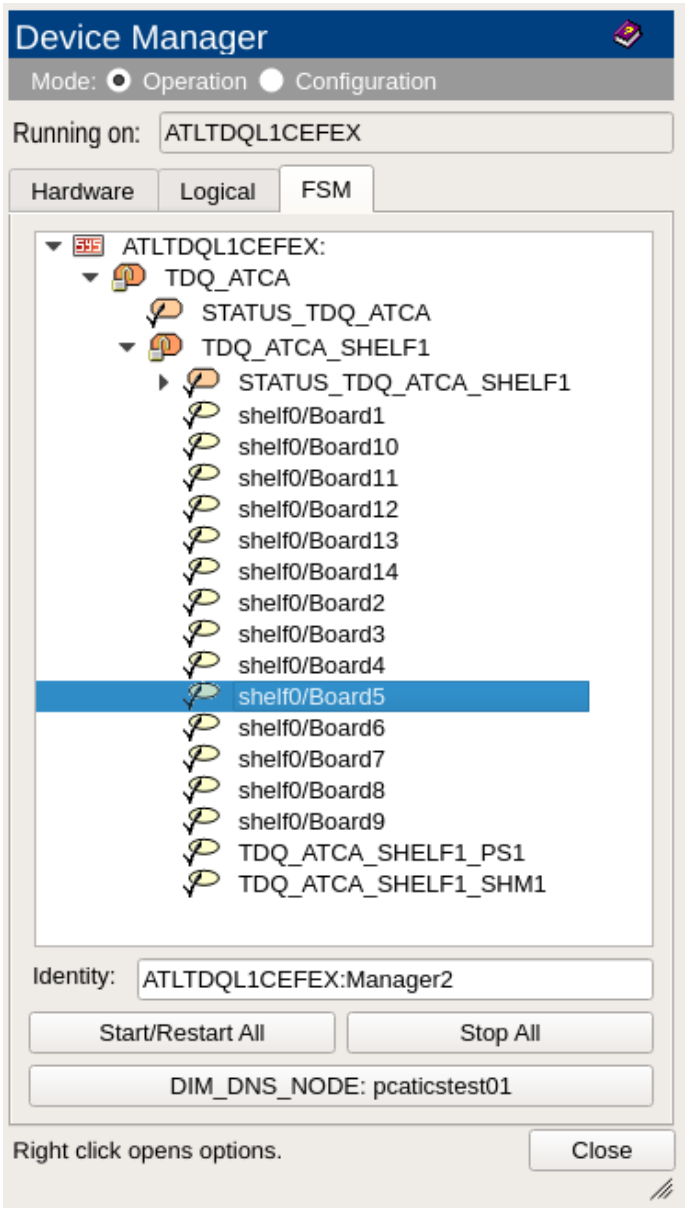

Figure 4.4: Full FSM tree of a system containing one ATCA shelf carrying fourteen slots.

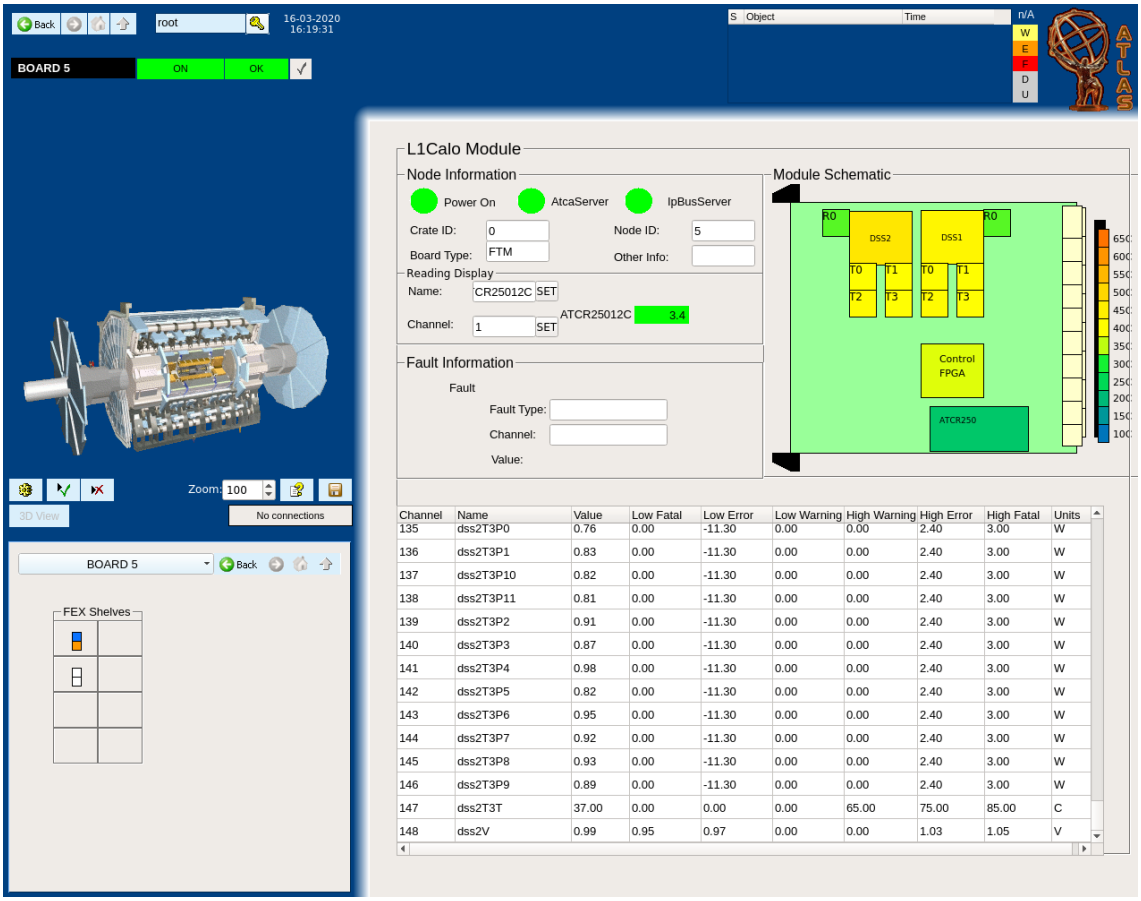

Figure 4.5: FSM view of a FWATCABOARD_ATCA_SLOT device unit, specifically for a slot containing an FTM module.

Chapter 5

The Standard Model and the Higgs Boson

The Standard Model of particle physics describes all known fundamental matter particles and their interactions with each other. This consists of twelve particles, each with half-integer spin, known as fermions. The fermions are split into three generations of increasing mass, and each generation consists of an up-type quark with electrical charge $+2/3$, a down-type quark with charge $-1/3$, a charged lepton with charge -1 and its corresponding electrically neutral neutrino. In addition, each fermion has a corresponding anti-particle, with the same mass and quantum numbers, but opposite charge. Despite the electrically neutral nature of the neutrinos, they are still thought to have corresponding antineutrinos with opposite lepton number and chirality.

Fermions interact with each other through three fundamental interactions. In decreasing order of strength, these are the strong interaction, which only affects the quarks, the electromagnetic interaction, which only affects charged particles, and the weak interaction, which affects all the fermions. Each interaction is mediated by the exchange of gauge bosons with integer spin. The mediators for the strong and electromagnetic interactions are the massless gluon (g) and photon (γ) respectively, while the mediators for the weak interaction are the massive $W^{\pm}$ and Z^0 bosons. These interactions are described by quantum field theories, specifically quantum

Table 5.1: Summary table showing the twelve fermions and three fundamental interactions. The fermions are split into three generations (I, II and III), of increasingly large mass.

	I	II	III	Interaction (Mediator)		
Quarks	u d	c s	t b	strong (gluon)	electromagnetic (photon)	weak (W/Z)
Leptons	e ν_e	μ ν_μ	τ ν_τ			

chromodynamics (QCD) for the strong interaction and electroweak (EW) theory for the weak and electromagnetic interactions. These theories are described in sections 5.1 and 5.2 respectively. A summary of the twelve fermions, and the three fundamental interactions between them, is shown in table 5.1.

In addition to the described particles, the Standard Model predicts a spin-0 particle known as the Higgs boson. This particle was predicted by the theorists Brout, Englert and Higgs [64, 65], as well as Guralnik, Hagen and Kibble [66], due to the process of electroweak symmetry breaking described in section 5.3. A Higgs-like boson was later discovered by the ATLAS and CMS experiments [3, 4], and this is now thought to be a Standard Model Higgs boson. The Higgs boson is predicted to interact with all massive particles, as described in section 5.4, and these interactions are the subject of the physics analyses of this thesis.

Sections 5.5 and 5.6 present results of the fundamental theory described, in terms of the physically observable behaviour of the Higgs Boson at the LHC. The focus is on the production and decay channels of the Higgs boson, as these topics are the most relevant to the analyses presented in this thesis. Finally, an overview of the most relevant current Higgs results from ATLAS and CMS is given in sections 5.7 and 5.8, in order to contextualise the presented analyses in terms of existing measurements.

5.1 Quantum Chromodynamics

Quantum chromodynamics is the field theory of the strong interaction. It is based around the $SU(3)$ symmetry group [67]. The strong interaction only interacts with quarks (and particles containing quarks) as every quark has a corresponding colour charge, which can have a value of r, g or b (or $\bar{r}$, $\bar{g}$, $\bar{b}$ for antiquarks). This colour charge cannot be observed in nature, and so quarks naturally form into composite particles with an overall neutral colour, known as hadrons. Overwhelmingly, the most common hadrons formed are baryons, made up of three quarks or three anti-quarks (rgb or $\bar{r}\bar{g}\bar{b}$), or mesons, made up of a quark-antiquark pair ($r\bar{r}$, $g\bar{g}$ or $b\bar{b}$). On rare occasions, more exotic hadrons such as pentaquarks can be formed, as observed by the LHCb experiment in 2015 [2].

The mediator of the strong interaction, the gluon, also carries colour charge. The colour states of the gluon consist of combinations of a colour and an anti-colour. This detail means that the gluon can self-interact, setting it apart from the photon that mediates the electromagnetic interaction. The self-interaction of the gluon causes the strength of the strong interaction to increase with distance, and this is what leads to the process of hadronisation, in which the bound hadron states are formed.

In fact, the length scale variation of the coupling of the strong force (α_s) is due to dependence on the energy scale of the interaction, q^2. At high values of q^2 (low range) the interaction is characterised by relatively weak normalisable interactions. This effect is known as asymptotic freedom [68], and here perturbative QCD can be used.

At low q^2 (high range), the interaction is much stronger, and the large coupling means results are no longer renormalisable, and so perturbative QCD can no longer be used. Therefore, in full QCD calculations, factorisation theorems must be used to separate the high energy behaviour, calculated theoretically, from the low energy

behaviour which must be determined from empirical measurements. In practice, the low scale behaviour is described by a parton distribution function (PDF), which describes the probability density of quarks and gluons (partons) within a hadron as a function of the parton's fractional contribution to the hadron's total momentum, x. At the energy scale of the LHC, the PDF of the proton is largely dominated by gluons.

The use of both PDFs and perturbative calculations in QCD requires the introduction of two parameters: the renormalisation scale μ_R and the factorisation scale μ_F. The choice of these scales in a calculation can affect the final result, so the uncertainty due to this choice must be accounted for.

5.2 Electroweak Theory

While the electromagnetic and weak interactions behave distinctly at low energies, at higher energies (for instance, in the LHC) they unify and behave as described by the combined electroweak theory [69, 70, 71]. This theory is based on the combined $SU(2)_L \otimes U(1)_Y$ symmetry group. In this formalism, the $SU(2)_L$ group accounts for the weak isospin, and the $U(1)_Y$ group accounts for the weak hypercharge (a combination of the electromagnetic charge and the isospin) of particles.

The electroweak Lagrangian contains four gauge bosons: B_μ and $W_\mu^{1,2,3}$. These bosons are not physically observed, but mix to create the physical gauge bosons $W^\pm$, Z^0 and γ that mediate the interactions. However, the electroweak Lagrangian in isolation does not predict masses for the $W^\pm$ and Z^0 bosons and as these bosons have observed masses [72, 73, 74, 75], the theory must be adjusted to account for this.

5.3 Electroweak Symmetry Breaking: The Brout Englert Higgs Mechanism

One of the foundations of the gauge theory of particle interactions is the local invariance of the Lagrangian under the gauge symmetries. The introduction of simple mass terms for the W and Z boson in the Lagrangian breaks this invariance. The solution to this is known as the Brout Englert Higgs (or usually just Higgs) mechanism [64, 65] and involves introducing a new scalar field to the Lagrangian. This scalar field restores the local $SU(2)_L \otimes U(1)_Y$ invariance of the Lagrangian, but breaks the invariance of the vacuum. This concept is known as spontaneous symmetry breaking.

The foundational concept of the Higgs mechanism is the introduction of a left handed, complex, isospin doublet field:

$$\phi = \begin{pmatrix} \phi^+ \\ \phi^0 \end{pmatrix} = \begin{pmatrix} \phi_1 + i\phi_2 \\ \phi_3 - i\phi_4 \end{pmatrix}, \tag{5.1}$$

and a corresponding potential

$$V(\phi) = \mu^2(\phi^\dagger\phi) + \lambda(\phi^\dagger\phi)^2, \tag{5.2}$$

where μ^2 is chosen to be less than 0 and λ is a free parameter describing the self-coupling of the field. The shape of this potential is shown in figure 5.1. Due to the shape, this potential is commonly known as the mexican hat or champagne bottle potential. As the global minimum of the potential occurs at a non-zero value, the field has a non-zero expectation value, chosen to be entirely real:

$$\phi_1 = \phi_2 = \phi_4 = 0, \tag{5.3}$$

$$\phi_3 = v \approx 246\text{GeV}, \tag{5.4}$$

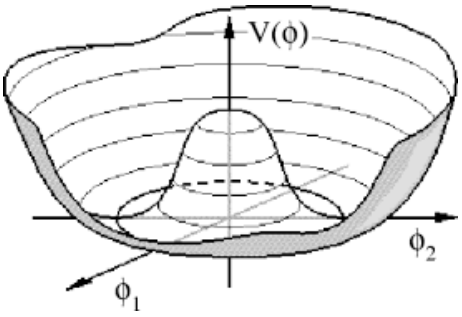

Figure 5.1: Diagram of the shape of the Higgs potential, in terms of the imaginary and real components of the field. Taken from [76]

where v is the vacuum expectation value. For small oscillations around this value, the field takes the form

$$\phi = \frac{1}{\sqrt{2}} \begin{pmatrix} 0 \\ v + h \end{pmatrix}, \tag{5.5}$$

where h is known as the scalar Higgs field.

The introduction of the Higgs field breaks the generators of the $SU(2)$ and $U(1)$ groups, such that the $W^{1,2,3}$ and B boson acquire mass. From here, the W^1 and W^2 bosons mix to create the $W^{\pm}$ bosons, and the W^3 and B bosons mix to create the Z^0 and the photon. This mixing allows the photon to remain massless, while giving the W and Z mass. The new Lagrangian shows interactions between the Higgs field and the W and Z bosons, as well as a new mass term due to the field's self-coupling, indicating the existence of a scalar Higgs boson:

$$m_H = \sqrt{2\lambda} v. \tag{5.6}$$

As the self coupling parameter λ is a free parameter, the Standard Model provides no prediction for the mass of the Higgs boson.

5.4 Yukawa Couplings

While the Higgs mechanism directly implies the mass of the W and Z boson, this is not the case for the fermions. The fermion mass terms must be added to the Lagrangian, in a way that preserves the overall $SU(2)_L \otimes U(1)_Y$ invariance. This can be achieved by introducing an interaction term between the Higgs doublet ϕ and the fermionic fields ψ. This interaction takes the form of an $SU(2)_L$ and $U(1)_Y$ singlet: $-\lambda_f \bar{\psi}_L \phi \psi_R$, where λ_f is the Yukawa coupling for the fermion f. The mass terms in the Lagrangian imply couplings between the Higgs boson and the other massive particles, proportional to the mass for fermions and to the squared mass for vector bosons:

$$g_{Hf\bar{f}} = \frac{m_f}{v}, \tag{5.7}$$

$$g_{HVV} = \frac{2m_V^2}{v}. \tag{5.8}$$

The analyses presented in this thesis are related to the linear mass dependence of the coupling between the Higgs boson and fermions.

5.5 Higgs Boson Production at the LHC

As the Higgs boson only couples to particles with mass, it is produced mainly by two types of vertex: HVV vertices and $Hf\bar{f}$ vertices, where either two massive vector bosons or two fermions interact to create a Higgs boson, or in some cases a vector boson or fermion radiates a Higgs boson. The self coupling of the Higgs boson theoretically allows for tri-Higgs vertices, but no processes involving this vertex have been observed. In the context of a proton-proton collider such as the LHC, this leads to four main production modes:

- **Gluon-gluon fusion (ggF):** Two gluons from the protons collide and fuse

via a virtual quark loop to form a Higgs boson.

- **Vector boson fusion (VBF):** A quark from each proton beam radiates a W or Z boson, and these bosons fuse to form a Higgs boson.
- **Associated VH production:** Two quarks from the protons collide to form a vector boson, and this boson radiates a Higgs boson. This process is sometimes called Higgs-strahlung.
- **Associated $t\bar{t}H$ production:** Two gluons each decay into a $t\bar{t}$ pair. One top quark and one anti-top quark fuse to create a Higgs boson. $b\bar{b}H$ production also occurs at the LHC, but less often due to the lower mass of the bottom quark.

The Feynman diagrams for these processes are shown in figure 5.2. Assuming a Higgs boson mass consistent with current measurements (see section 5.7), Higgs production at the LHC is by far dominated by gluon-gluon fusion, which makes up 89% of the total cross-section. This is mostly due to the large abundance of gluons within high energy protons. This is followed by vector boson fusion at 7% of the cross-section, VH production at 2.3%, then $t\bar{t}H$ and $b\bar{b}H$ at a combined 1.8% [77]. With a total production cross-section of 55.62 pb at 13 TeV [78], approximately 7.8×10^6 Higgs bosons are expected to have been produced within the 140 fb^{-1} of data collected by ATLAS during Run-II.

5.6 Higgs Boson Decay Channels

The decays of the Higgs boson are again driven by the $Hf\bar{f}$ and HVV vertices. For vector bosons, this causes the Higgs boson to decay into VV pairs directly. Considering that the Higgs mass is less than twice the mass of the vector bosons, one of the produced bosons must be off-shell, due to energy conservation. These processes lead to the $H \to ZZ^*$ and $H \to WW^*$ decay channels, with branching ratios of 2.64×10^{-2} and 2.15×10^{-1} respectively. For fermions, this leads to decay

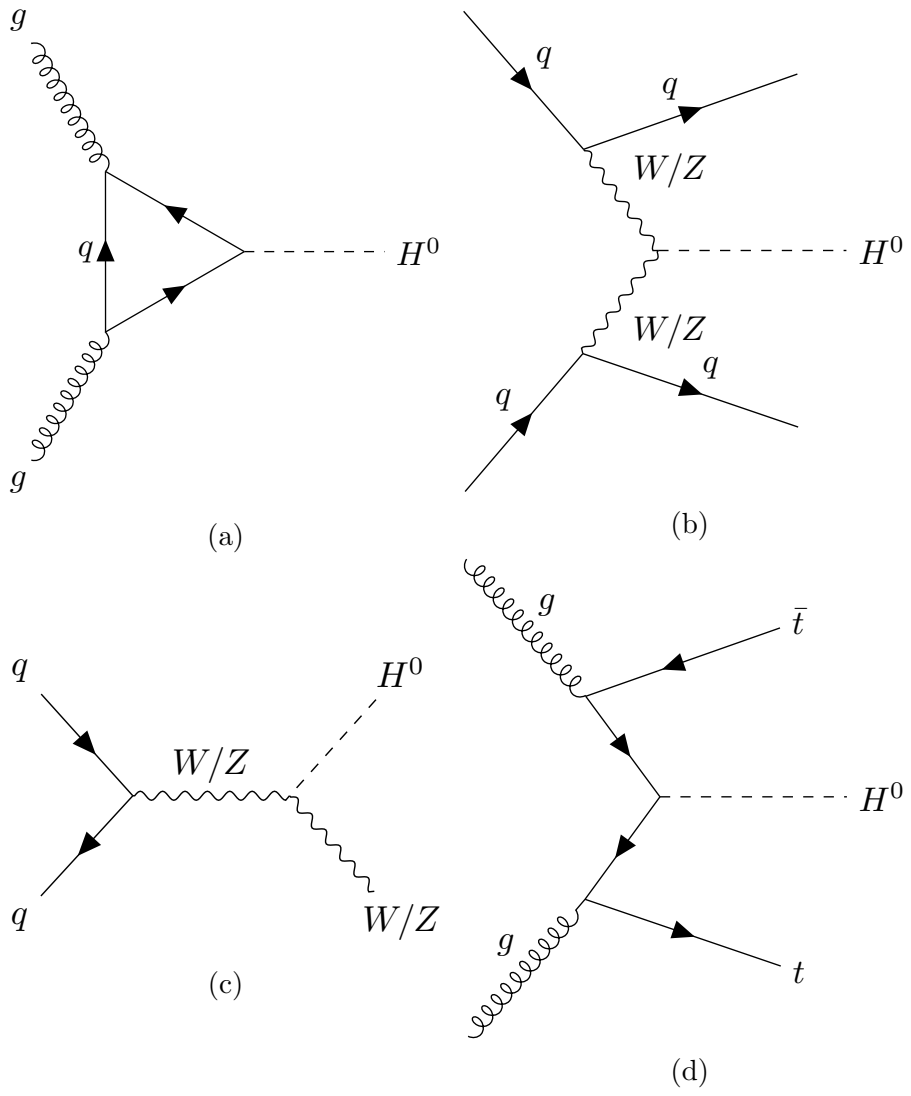

Figure 5.2: Feynman diagrams showing the four largest cross-section production mechanisms of the Higgs boson at the LHC: (a) gluon-gluon fusion, (b) vector boson fusion, (c) associated VH production and (d) associated $t\bar{t}H$ production

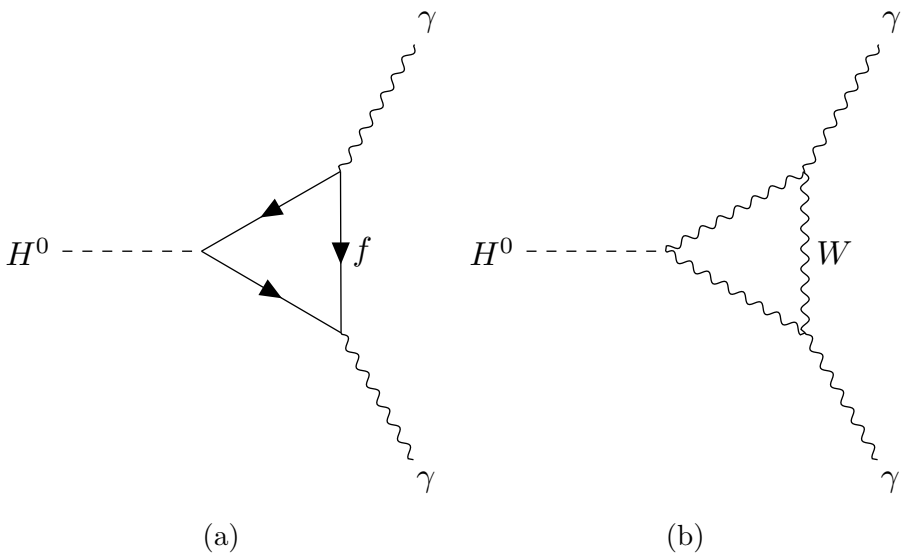

Figure 5.3: Feynman diagrams showing the $H \to \gamma\gamma$ decay channel.

channels for each possible $H \to f\bar{f}$ process. A variety of signatures are considered in the searches for these processes, due to the variation in types of background. The Standard Model branching ratios of $H \to b\bar{b}$, $H \to \tau^+\tau^-$, $H \to c\bar{c}$ and $H \to \mu^+\mu^-$ have been calculated as 5.809×10^{-1}, 6.256×10^{-2}, $2.884 \times 10{-}2$ and 2.171×10^{-4} respectively [78].

The Higgs boson can also decay via the the $H \to \gamma\gamma$ decay channel. This decay is forbidden directly as the photon is massless. The decay can still happen, however, via a loop of either top quarks (other fermions are theoretically possible but insignificant due to their lower mass) or W bosons. The Feynman diagram for this process is shown in figure 5.3. The $H \to Z\gamma$ decay is also predicted through the same diagrams. In this process, the top and W loops interfere destructively, which leads to the W loop dominating. The Standard Model branching ratios of $H \to \gamma\gamma$ and $H \to Z\gamma$ are 2.270×10^{-3} and 1.541×10^{-3} respectively [78].Figure 5.4 shows the branching ratios of the different decay channels of the Higgs boson, as a function of its assumed mass. From this it can be seen that the dominant decay process is $H \to b\bar{b}$, whereas low mass leptonic decay channels such as $H \to \mu^+\mu^-$ are much less common.

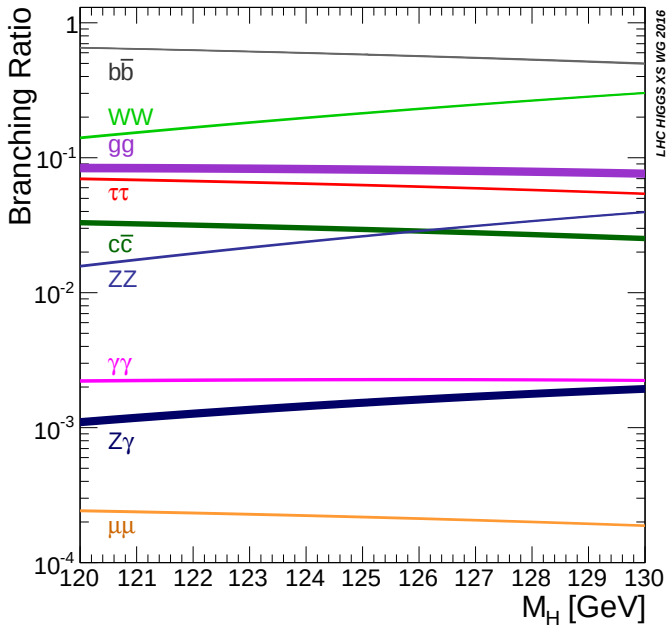

Figure 5.4: Higgs boson branching ratios and their uncertainties for the mass range around 125 GeV [78].

5.7 Higgs Boson Measurements at the LHC

A Higgs-like boson was discovered in 2012 by both CMS and ATLAS. The measurement by ATLAS was performed using the $H \to ZZ^* \to 4l$, $H \to \gamma\gamma$ and $H \to WW^* \to e\nu\mu\nu$ decay channels. ATLAS reported a measured mass of $126.0 \pm 0.4(\text{stat.}) \pm 0.4(\text{syst.})$ GeV, with a global significance of 5.1σ and a signal strength of $\mu = 1.4 \pm 0.3$, relative to the hypothesis of a Standard Model Higgs boson [3]. CMS used the $H \to ZZ^*$ and $H \to \gamma\gamma$ decay channels in their mass measurement, combining these with the $H \to WW^*$, $H \to \tau\tau$ and $H \to b\bar{b}$ decay channels in the calculation of the overall significance. This yielded a mass measurement of $125.3 \pm 0.4(\text{stat.}) \pm 0.5(\text{syst.})$ GeV, a signal strength of 0.87 ± 0.23 and a global significance of 4.5σ [4].

Since the discovery of the Higgs boson, its physical properties have been measured to greater and greater precision. The latest combined measurement between ATLAS and CMS [79] was performed with Run-I data, and finds a mass

of $125.09 \pm 0.21(\text{stat.}) \pm 0.11(\text{syst.})$ GeV. The latest Run-II results find masses of 124.97 ± 0.24 GeV (ATLAS) [80] and 125.38 ± 0.14 GeV (CMS) [81]. Both ATLAS and CMS have found evidence that the Higgs boson is a spin-0 particle, by analysing the angular distribution of its decay products, and comparing this with several different spin hypotheses [82, 83].

The interactions between the Higgs boson and the third generation of fermions are very well explored. The $H \to \tau^+\tau^-$ decay has been observed by both ATLAS and CMS, using both the leptonic and hadronic decays of the τ in the final state. The decay was observed with a significance of 6.4σ by ATLAS [84] and a significance of 5.9σ by CMS [85]. As the observed Higgs boson does not have enough mass to decay into a pair of top quarks, the best way to study the interaction between the top and the Higgs is to measure the $t\bar{t}H$ production mechanism. This process has also been observed by both experiments, first by CMS at a significance of 5.2σ [86] and then later by ATLAS at a significance of 6.3σ within a larger dataset [87]. Finally, the $H \to b\bar{b}$ decay has been observed by ATLAS and CMS. In both cases the large hadronic background at the LHC was overcome by focusing on events fitting the signature of the VH production mechanism, although the results are combined with searches using the VBF and $t\bar{t}H$ production processes. In this search ATLAS observed the decay with a significance of 5.4σ [88] and CMS with a significance of 5.6σ [89].

Searches for second generation fermionic couplings of the Higgs boson are not as sensitive, due to the low branching ratios of the lower mass particles. The latest searches for the $H \to c\bar{c}$ decay by ATLAS and CMS have set upper limits on the branching ratio of around 100 and 70 times the Standard Model value respectively, and have not yielded any observations[90, 91]. The same is true for the $H \to \mu^+\mu^-$ decay, albeit with limits much closer to the Standard Model value. Given that the ratio between the masses of the charm quark and the muon is approximately 10, one would expect the search for the $H \to c\bar{c}$ decay to be more sensitive, due to the larger Standard Model branching ratio. This disparity is due mainly to the smaller backgrounds. The latest limits set on the $H \to \mu^+\mu^-$ branching ratio by ATLAS

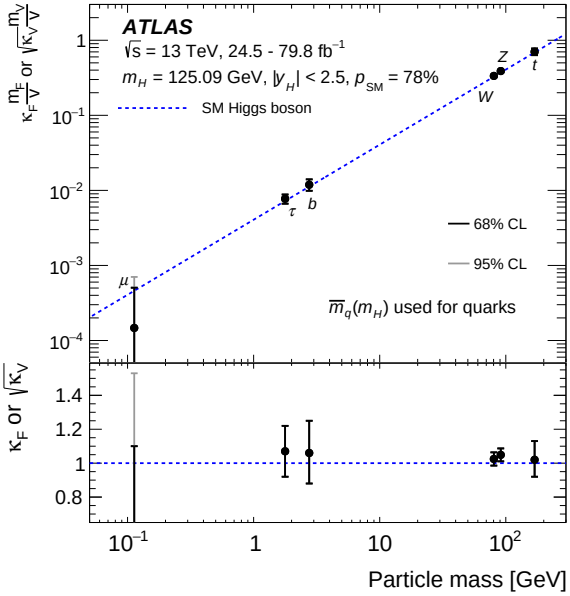

Figure 5.5: Measured reduced coupling-strength modifiers calculated using combined measurements from ATLAS data corresponding to integrated luminosities of up to 80fb^{-1}, as a function of particle mass. The blue dotted line represents the Standard Model prediction. The measurements shown here assume no beyond the Standard Model contributions to the Higgs boson decays [96].

and CMS are at 1.7 and 3.0 times the Standard Model expectation value respectively [92, 93]. The second generation fermions are also probed through searches for the $H \to \phi\gamma$ [94] and $H \to J/\psi\gamma$ [95] decays.

Figure 5.5 shows combined measurements of the reduced coupling strength modifiers $\kappa_f m_f/v$ and $\sqrt{\kappa_V} m_V/v$, where κ_f and κ_V are the effective coupling strengths to fermions and vector bosons respectively, so that $\kappa_f = \kappa_V = 1$ corresponds to the Standard Model expectation. The p-value measured for the compatibility between the SM hypothesis and the best-fit of these measurement is 78%, and so it can be seen that the hypothesis appears to be consistent with currently available measurements [96].

5.8 Searches for Higgs Boson Decays to First Generation Fermions

The couplings of the Higgs boson to the first generation fermions are by far the least studied. The main studies into the Higgs coupling with these lightest matter particles are a search for the $H \to e^+e^-$ decay by CMS [97] and a search for the $H \to \rho^0\gamma$ decay by ATLAS [94].

The main analysis presented in this thesis is a search for the $H \to e^+e^-$ decay. The Standard Model branching ratio is calculated to be 5×10^{-9}, which is below what is considered measurable at the LHC. This is approximately equal to the Standard Model branching ratio for $H \to \mu^+\mu^-$, 2.171×10^{-4}, multiplied by a factor of m_μ^2/m_e^2, as there are two fermions invlolved in the decay, introducing a square dependence on $g_{Hf\bar{f}}$. In addition to this, there are non-resonant contributions, such as the Dalitz decay $H \to ee\gamma$, that do not depend on the Yukawa coupling, which also have a large contribution to the overall cross-section. Because of this the Standard Model branching ratio is yet to be calculated fully.

However, the $H \to e^+e^-$ process is of particular interest because the Standard Model branching ratio is so small, as this means that small contributions from beyond the Standard Model processes can have a more significant effect on the overall measurement. A full description of such a process is beyond the scope of this thesis, but examples could be the mixing of new massive vector-like leptons with electrons, the mixing of the Higgs boson with a new massive scalar doublet that also couples to electrons, or the presence of a new massive vector boson. These processes are illustrated in figure 5.6. More details on this and other possible BSM contributions are given in [98]. In brief, changes to the Standard Model branching ratio beyond the Yukawa coupling can be described by the interaction of higher order operators with the electron field:

$$\mathcal{L}_{\text{BSM}} = \frac{c_0}{M^2}\varphi^\dagger\varphi\bar{l}_L\varphi e_R, \tag{5.9}$$

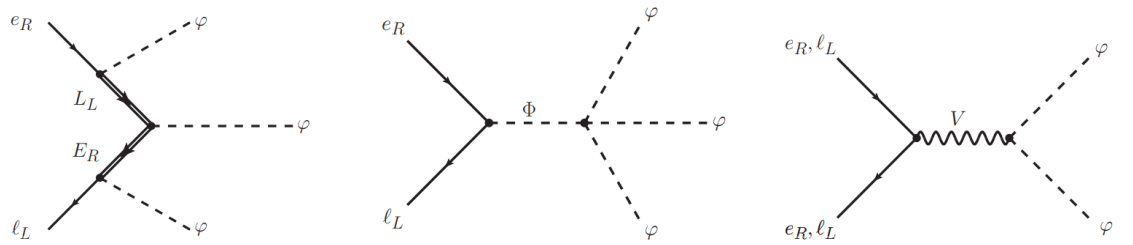

Figure 5.6: Diagrams showing the possible origins beyond the Standard Model contributions to the Lagrangian. Left: mixing of the electrons with heavy vector-like leptons. Middle: mixing of the SM Higgs doublet with a heavy scalar doublet that couples to electrons. Right: exchange of a heavy vector boson [98].

where M is a new physics scale, c_0 is a complex coupling, and φ is the Higgs doublet. These operators could be explained by various kinds of mixing, such as those mentioned earlier. The coupling c_0 would generally be expected to have the form of a 3×3 matrix in lepton flavour space, so the new physics process would also be expected to interact with other Higgs-lepton couplings, possibly even introducing lepton flavour violating Higgs boson decays [99].

When the Higgs doublet in this Lagrangian is expanded around the vacuum expectation value, a new term to the Higgs electron coupling, in addition to the Yukawa coupling y_e:

$$g_{Hee} = y_e + \frac{3c_0 v^2}{2M^2} = \frac{\sqrt{2}m_e}{v} + \frac{c_0 v^2}{M^2}. \tag{5.10}$$

Since the electron's mass is much smaller than the vacuum expectation value, the effect of these higher order operators can be relatively large, even for high values of the new physics scale M. However, this also means that even higher order operators may also have a significant contribution, and so in order to parameterise the modification in a more model-independent way, the coefficient κ_e is introduced:

$$g_{Hee} = \kappa_e \frac{\sqrt{2}m_e}{v}, \tag{5.11}$$

and, assuming only the corrections discussed here have an effect, then the measured

value of κ_e can be used to examine the possible scale of new physics:

$$\kappa_e = 1 + \frac{c_0 v^3}{\sqrt{2} m_e M^2}. \tag{5.12}$$

Through comparison of the measured $H \to e^+e^-$ branching ratio and that predicted by the Standard Model, a value for κ_e can be obtained:

$$\mathrm{BR}(H \to e^+e^-) = \frac{|\kappa_e|^2 \mathrm{BR}(H \to e^+e^-)_{\mathrm{SM}}}{1 + (|\kappa_e|^2 - 1)\mathrm{BR}(H \to e^+e^-)_{\mathrm{SM}}}. \tag{5.13}$$

In the case of the limit set by CMS using Run-I data of 0.0019 [97], this gives an upper bound on the value of $|\kappa_e|$ of 611. If the value of c_0 is set to 1, this corresponds to a lower bound on the new physics scale, $M > 5.8$ TeV. Extrapolating this result, the LHC could achieve a sensitivity of the scale $|\kappa_e| \sim 150$ by the end of high luminosity running [98].

The $H \to e^+e^-$ analysis presented in this thesis is published in [1], along with a search for the lepton flavour-violating decay $H \to e^{\pm}\mu^{\mp}$, which is not discussed in this thesis.

Chapter 6

Prospects Study for the $H \to \mu\mu$ Decay Channel in the HL-LHC with the ATLAS Upgrade

6.1 Introduction

Since the discovery of the Higgs boson in 2012, its couplings with the vector bosons W and Z and with the 3rd generation fermions t, b and τ have been observed, through various searches for particular decay channels and production modes. Many of the decay channels which have been observed are direct decays, which directly involve the particular coupling, such as $H \to VV \to llll$, where V is a W/Z boson and l is either a lepton or neutrino [3] and $H \to \tau^+\tau^-$ [100]. Analyses have also been performed finding indirect decays such as $H \to \gamma\gamma$, which has contributions from the W and top couplings via a virtual loop [3].

The remaining couplings of the Higgs boson, namely to first and second generation fermions, are yet to be confirmed. The largest of these, the coupling to the c quark, would most obviously be searched for through the $c\bar{c}$ decay, but the large QCD

background at the LHC makes this decay difficult to observe, although it has been attempted, and in this analysis an upper limit on $\sigma(pp \to ZH) \times \mathcal{B}(H \to c\bar{c})$ was calculated at around 100 times the Standard Model value of 26 fb[90]. There are some lower background searches for this coupling, like searches for the exclusive decay to bound $c\bar{c}$ meson states, such as the decay $H \to J/\psi\gamma \to \mu^+\mu^-\gamma$, but searches such as this have not yet yielded an observation [101]. Despite the low background, the measured limit on the branching ratio for this analysis is around 1000 times the Standard Model value, as the SM value of 2.8×10^{-6} is so low. A more viable prospect, then, would be the coupling of the Higgs field to the muon, via the $H \to \mu^+\mu^-$ decay. Such a search would eliminate the problem of QCD background, however its low Standard Model branching ratio of 2.18×10^{-4} [102] means it cannot be observed with the amount of data currently available at ATLAS [103], although a discovery is expected with the addition of Run-III data, assuming the branching ratio is at least as large as the Standard Model prediction.

This should not be the case at the HL-LHC, where ATLAS is expected to record approximately 3000 fb^{-1} worth of data at a centre of mass energy of 14 TeV, and with a Standard Model cross-section times branching ratio of 62.6 pb $\times 2.17 \times 10^{-4} = 13.6$ fb [78] this amounts to around 41000 expected produced events, making the observation of the $H \to \mu^+\mu^-$ decay a certainty, if the associated Yukawa coupling has its Standard Model value. As seen in table 6.1, 63% of these events are expected to be accepted in the signal region, however an observation is still expected. This study investigates the possible sensitivity with which this rare decay can be measured, using simulated $H \to \mu^+\mu^-$ data, smeared according to the proposed performance of the upgraded ATLAS detector. This is a continuation of the study presented by ATLAS in 2018 [104], using more reliable models to simulate the $Z \to \mu^+\mu^-$ background and using a newer detector scenario to smear the generated Monte Carlo events.

6.2 Analysis

This analyis is broadly split into four main steps:

- Truth level Monte Carlo events are created for the relevant background and signal processes, smeared using functions that approximate the performance of the upgraded ATLAS detector and scaled to the expected statistics for the 3000 fb^{-1} of data expected at the HL-LHC
- Basic selection and classification is applied to the Monte Carlo events, in order to maximise the expected significance of the result
- Analytical functions are fitted to the invariant mass distributions of the selected events, in order to find the expected shapes of the signal and background
- An Asimov dataset is produced from these shape functions, profiled at the expected Standard Model normalisations, and the final result is extracted from a maximum likelihood fit to this dataset.

6.2.1 Upgrade Performance Functions

For the purpose of "prospect studies" such as this, the use of full Monte Carlo simulation, which simulates the full physical structure of the detector requires intensive use of limited computing resources. A much less intensive way to account for the detector performance is to parameterise it into simple functions, depending on the kinematics of the particles involved in each event. This way, rather than simulating the full path of every particle, one can find the expected momentum and energy resolution, as well as the expected trigger and reconstruction efficiency, and then use random number generation to "smear" the kinematics to a new "measured" value, and decide whether to record the particle or event. Similarly, parameterised functions can be used to quickly generate a collection of pileup jets for each event, rather than simulating around 200 minimum bias events for every Monte Carlo event. The

functions used in this analysis are based on the upgraded ATLAS detector described in Chapter 2, including the fully silicon tracker ITK and the upgraded trigger system. This approximation provides good enough precision to reliably predict an expected result, as shown in section 6.3.4, where studies have been performed into the accuracy of the method.

6.2.2 Monte Carlo Samples

The only "data" in this analysis comes from truth level information extracted from event generator samples. The signal is a combination of gluon gluon fusion (ggF) and vector boson fusion (VBF), the two most common production mechanisms of the Higgs boson in hadron collisions. The combined cross section of these two production mechanisms,

$$\sigma_{ggF} + \sigma_{VBF} = 58.87pb \tag{6.1}$$

is 94% of the Higgs boson's total production cross section at a centre of mass energy of 14 TeV [78]. The two signal samples used here are generated using POWHEG [105, 106], interfaced to PYTHIA8 [107], and the produced Higgs bosons are forced to decay to dimuon final states in 100% of the events.

The decay channel being studied has three dominant background processes with two oppositely charged muons in the final state which need to be considered:

- $Z \to \mu\mu$ ($\sigma = 2340$ pb)
- $t\bar{t} \to b\bar{b}\mu\nu\mu\nu$ ($\sigma = 896$ pb)
- $WW \to \mu\nu\mu\nu$ ($\sigma = 12.8$ pb)

with the Z background being the most prominent of the three. The contribution of events with a non-isolated muon, or hadrons faking muon signals, is expected to be small so are neglected.

Four samples are produced for the Z background, split between the electroweak production, such as vector boson fusion to form a Z boson, and QCD production, such as direct Z production from two quarks, and each of those between the invariant mass ranges $40 < m_{\mu\mu} < 95$ GeV and $m_{\mu\mu} > 95$ GeV. The split in invariant mass is used so that the Z resonance does not dominate the statistics of the samples. These samples are produced entirely using Sherpa 2.2.2 [108]. The QCD samples are produced at next to leading order in α_s for events with 0 - 2 jets and at leading order for events with 3 or 4 jets, while the electroweak samples are produced at leading order in α_{EM} for events with 2 or 3 jets.

Both the $t\bar{t}$ and WW samples are produced using MC@NLO [109, 110], interfaced to HERWIG [111], and using JIMMY [112] for multi-parton interactions. All nine final states (i.e. combinations of $W \to e\nu$, $W \to \mu\nu$ and $W \to \tau\nu$) are considered for the WW background, although only the $\mu\nu\mu\nu$ final state has a large contribution. This is done as the extra diboson samples already exist and can be run over without a substantial increase in required computing resources. The $t\bar{t}$ sample has a filter applied which selects events with at least one leptonically decaying W boson in the final state. Each W has a leptonic branching fraction of $\mathcal{B}(W \to l\nu) = 0.1057$ [102], so the final filter efficiency is $1 - (1 - 3 \cdot (0.1057))^2 \approx 53\%$.

6.2.3 Event Selection

Selection criteria are applied in order to cut out as much background as possible while still retaining a reasonably large signal. The criteria used here are similar to those used in the 8 TeV analysis [113], but with tighter jet requirements, to account for the large pileup (an average of 200 interactions per bunch crossing) expected at the HL-LHC. The criteria are:

- Exactly two oppositely charged muons, neither of which are within $\Delta R = 0.4$ of a good jet, where muons are required to have a transverse momentum of $p_T > 15$ GeV and a pseudorapidity of $|\eta| < 2.5$. Jets in the selected events may

be pile-up jets, but jets are also produced in some of the signal and background processes, such as in vector boson fusion. Good jets are defined as jets with transverse energy of $E_T > 30$ GeV which pass an algorithm which suppresses pile-up jets.

- The leading p_T muon has $p_T > 25$ GeV
- Either of the selected muons passes a single muon trigger designed to trigger on muons with a minimum p_T of 20 GeV

The single muon trigger used is expected to have an efficiency between 60% and 99%, dependent on the pseudorapidity of the muon. The invariant mass distribution after event selection can be seen in Figure 6.1. Here it can be seen that the Higgs peak and the Z peak have a different shape. The large tails of the Z peak are due to the production of off-shell Z bosons in the Monte Carlo samples. Due to the lower overall production cross-section, off-shell Higgs boson production is not considered.

6.2.4 Event Classification

The selected events are split up into seven different kinematic categories. The first of these is designed to select events that resemble the VBF signal process, and events that are not selected for this category are then split into one of six categories based on the transverse momentum and pseudorapidities of the selected muons. This ensures that each event belongs to exactly one category. The momentum and pseudorapidity boundaries of the latter six categories are chosen to increase the significance of the result by exploiting the higher average di-lepton transverse momentum that signal events have in comparison to the $Z \to ll$ background as well as the better momentum resolution of the detector at central pseudorapidities.

Events are chosen for the VBF-like category if they pass the following cuts:

- The two leading jets must have an invariant mass $m_{jj} > 650$ GeV

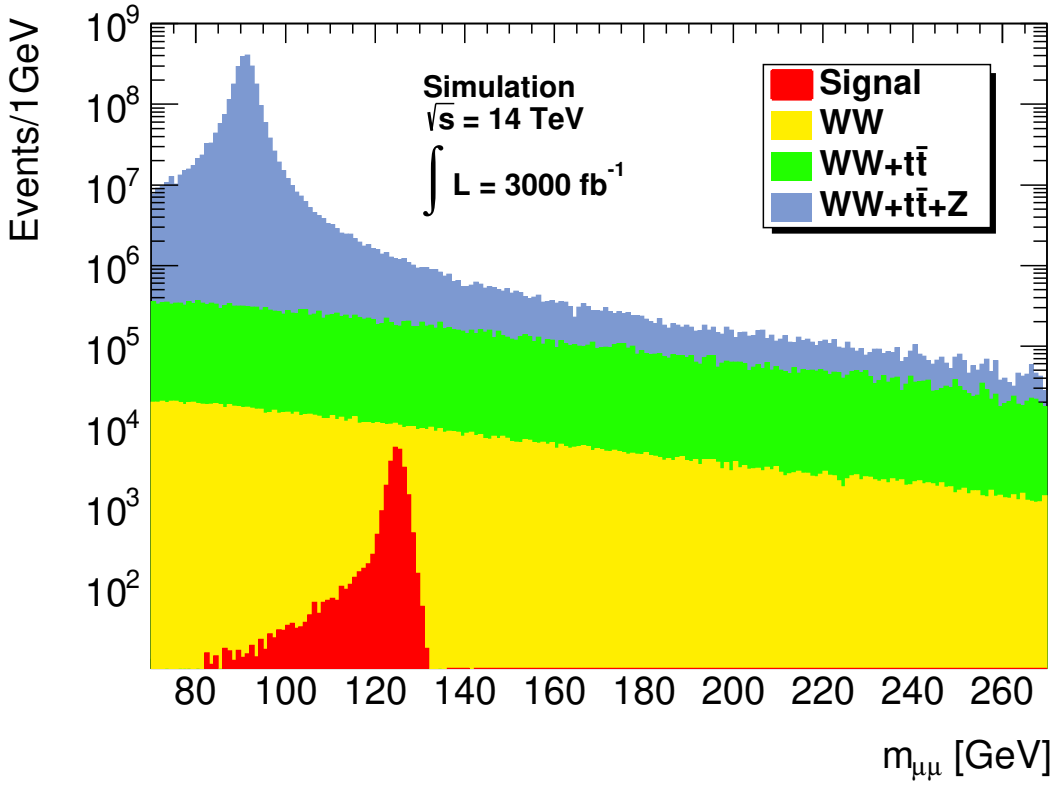

Figure 6.1: Distribution of di-muon invariant mass after full selection

- They must also have a large separation in pseudorapidity $|\Delta\eta_{jj}| > 3.6$
- The Higgs candidate must have a large transverse momentum $p_T^{\mu\mu} > 80$ GeV
- The Higgs candidate must be broadly in line with the average of the pseudorapidities of the two leading jets $\eta^* = \left|\eta_{\mu\mu} - \frac{\eta_{j1}+\eta_{j2}}{2}\right| < 2.0$

These cuts were chosen to reflect the Physics of the VBF interaction, for example the second cut is to find events with two very far separated jets and the fourth is ensuring the Higgs candidate is to some extent between the jets. The exact values that are cut on are chosen based on an optimisation performed in an earlier analysis, based on a lower pile-up. This optimisation chose the values that provided the best VBF significance in this VBF-like category.

The remaining categories are based solely on the pseudorapidity and transverse momentum of the muons. These categories are chosen to exploit the changing muon resolutions at different momenta and pseudorapidities. They consist of a central and non-central category, where the central category is defined as having both muons detected within $|\eta| < 1.0$, and then both of these categories are split into three based on the di-muon transverse momentum:

- Low $p_T^{\mu\mu}$: $p_T^{\mu\mu} < 15$ GeV
- Medium $p_T^{\mu\mu}$: $15 < p_T^{\mu\mu} < 50$ GeV
- High $p_T^{\mu\mu}$: $p_T^{\mu\mu} > 50$ GeV

6.2.5 Signal and Background Modeling

Before the final fit, the shape of both the signal and background must be parameterised as mathematical functions. These functions are used in the final fit, with shape parameters fixed and their normalisations floating, and they are also used to generate a dataset in which all the observed quantities are set to their expected

values, upon which the final fit is performed. This is known as an Asimov dataset. Models are created for each of the seven kinematic categories, as well as for the inclusive total of the selected events. The parameters of the models are found using a binned likelihood fit to the invariant di-muon mass of the Monte Carlo events, with a bin size of 0.4 GeV.

The signal is parameterised as the sum of a Crystal Ball function [114] and a Gaussian, where both functions are assumed to have the same mean:

$$S(m_{\mu\mu}) = F \cdot G(m_{\mu\mu}; < m_H >, \sigma_G) + (1 - F) \cdot CB(m_{\mu\mu}; < m_H >, \sigma_{CB}, \alpha, N). \quad (6.2)$$

The shape parameters (mean, widths, the fractional contribution of the Gaussian to the model F, and the cut off α and decay constant N for the Crystal Ball) are found using a fit to the combined ggF and VBF Monte Carlo samples. These are then fixed, allowing just the normalisation to float in the final fit. Plots of the fitted signal model can be seen in the results section.

The background model used is also the sum of two different functions, one to account for the contribution of the Z and another for the continuum background of the W^+W^- and $t\bar{t}$ contributions. The Z background is parameterised as the convolution of a Breit-Wigner peak, with width and mean fixed at the theoretical values for the Z boson Γ_Z and M_Z, and a Gaussian distribution, to account for the resolution of the detector. The remaining backgrounds are parameterised with an exponential decay:

$$B(m_{\mu\mu}) = F_Z \left[BW(m_{\mu\mu}; M_Z, \Gamma_Z) \otimes G(m_{\mu\mu}; M_Z, \sigma_Z)\right] + (1 - F_Z) B e^{a \cdot m_{\mu\mu}}, \quad (6.3)$$

where B is normalization parameters, chosen so the two parts of the model both integrate to unity over the signal region. The overall function is fitted in two steps: first, the shape parameters of the Z function are found with a fit to the selected Z Monte Carlo events in the invariant mass range of $89 < m_{\mu\mu} < 110$ GeV, then these shape parameters are fixed, the function is summed with an exponential function

and the total function is fitted to all the selected background (i.e. Z, WW and $t\bar{t}$) Monte Carlo events in the signal region to find the exponential decay constant a, overall normalisation and fractional contribution of the Z peak F_Z.

6.2.6 Final Fit

The final step of the analysis is a binned log-likelihood fit of the signal and background models to a set of Asimov data, again with a bin size of 0.4 GeV, in order to extract the expected significance at 3000 fb^{-1}. The Asimov data is created using the same models, assuming that the branching ratio of $H \to \mu\mu$ is the SM value of 2.171×10^{-4}. In this fit, the shape parameters of the models are kept constant at the values found in the previous step, but the normalisations of the signal and background models are allowed to float. Two fits are performed:

- An inclusive fit of the model produced from all selected events, with a single parameter of interest $\mu = \frac{N_{sig}}{N_{sig}^{SM}}$
- A simultaneous fit of all seven models across the different kinematic categories again with a single parameter of interest μ

The inclusive fit has one nuisance parameter, the normalisation of the background model, while the simultaneous fit has one nuisance parameter for each category, also corresponding to the background normalisations in each category. Before the fit, all the normalisation parameters are set to 0.5 times the values from the shape fit, to avoid intoroducing bias to the analysis. The final result of the analysis, the significance, is approximated as $\frac{S}{\sqrt{B}}$ where S and B are the integrals of the post-fit signal and background models respectively, within 1.5 standard deviations of the signal mean.

The main systematic uncertainties in the analysis are theoretical uncertainties, including the uncertainty on the SM branching ratio and Higgs production cross-section as well as the QCD uncertainties due to the choice of renormalisation and

Table 6.1: Results of the event selection for the signal (ggF + VBF) and background (Z + WW + $t\bar{t}$) Monte Carlo events, scaled to 3000 fb^{-1}. The overall selection efficiency is also given.

Cut	Signal	Background
All Events	38490 ± 160	$(9.739 \pm 0.029) \times 10^9$
Two reconstructed muons	25400 ± 130	$(3.143 \pm 0.014) \times 10^9$
$p_T^{\mu_1} > 25$ GeV	25300 ± 130	$(2.844 \pm 0.013) \times 10^9$
Passes muon trigger	25280 ± 130	$(2.842 \pm 0.013) \times 10^9$
$110 < m_{\mu\mu} < 160$ GeV	24360 ± 130 (63.2%)	$(5.242 \pm 0.027) \times 10^7$ (0.54%)

factorisation scales, which are currently around 5% altogether and the luminosity uncertainty which is expected to be around 3% at the HL-LHC [104]. Other sources of uncertainty, including lepton ID performance and background modeling uncertainty are assumed to provide vanishingly small contributions [103]. As the uncertainty on the final result is expected to be mainly statistical, and the values of the systematic uncertainties could feasibly change leading up to and during HL-LHC running, the systematic uncertainties are not included in the final fit.

6.3 Results

6.3.1 Event Selection and Classification

This section summarises the results of the selection process on the background and signal Monte Carlo. Table 6.1 compares the effect of the overall selection on the signal and on the background, showing a much greater overall efficiency for the signal than for the background, as desired. Table 6.2 compares the number of events in each of the categories between the ggF and VBF Monte Carlo samples. This shows that the VBF-like region contains a greater proportion of VBF over ggF signal events than any other region. Figure 6.2 shows the final invariant mass distribution in all categories after the selection has been performed.

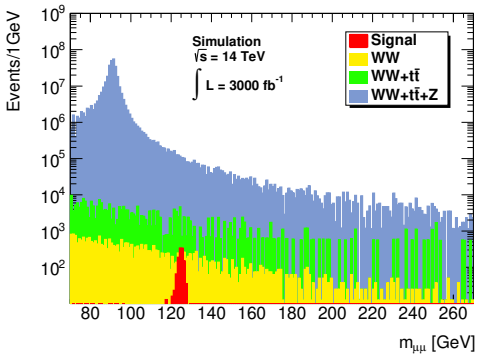

(a) Low p_T, central

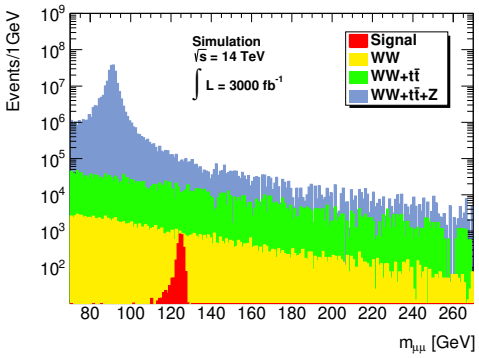

(b) Medium p_T, central

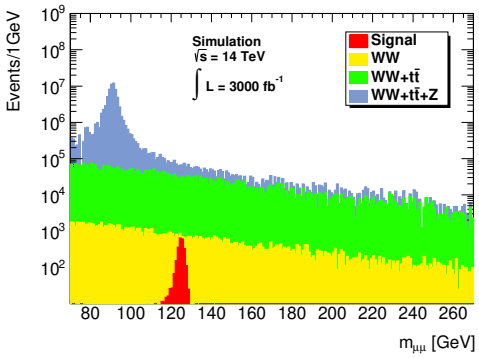

(c) High p_T, central

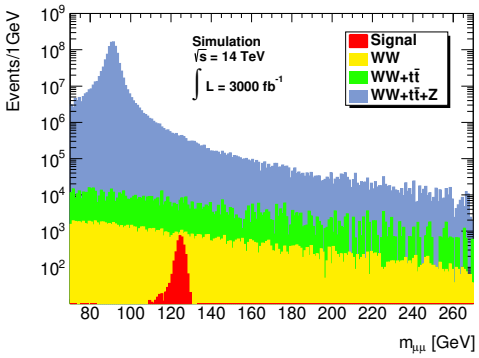

(d) Low p_T, non-central

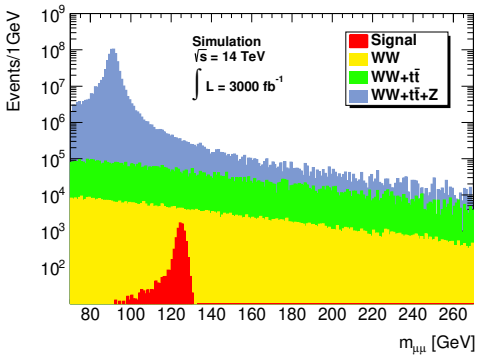

(e) Medium p_T, non-central

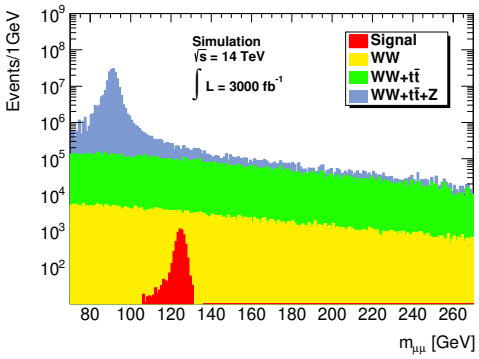

(f) High p_T, non-central

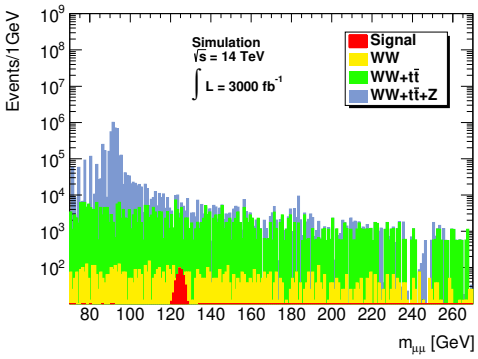

(g) VBF-like region

Figure 6.2: The invariant mass distribution of the selected Monte Carlo events in the seven kinematic categories

Table 6.2: Results of the event classification, comparing the ggF signal Monte Carlo to the VBF signal Monte Carlo

Category	ggF	VBF
VBF	231 ± 13	233.5 ± 3.6
Low p_T, Central	1217 ± 29	15.46 ± 0.93
Medium p_T, Central	2828 ± 45	110.7 ± 2.5
High p_T, Central	2158 ± 39	318.3 ± 4.2
Low p_T, Forward	3324 ± 49	40.6 ± 1.5
Medium p_T, Forward	7626 ± 74	315.3 ± 4.2
High p_T, Forward	5144 ± 61	796.2 ± 6.7

6.3.2 Background and Signal Modelling

Here the results of the fitting of the background and signal shapes to the selected Monte Carlo are presented. Figure 6.3 shows the fitted signal models for each category, as well as for the inclusive selection of the sum of the categories in the signal Monte Carlo events. Figure 6.4 shows the equivalent fitted background models. Tables 6.3 and 6.4 show the fitted shape parameters of these models, as well as the χ^2 value for each, showing that each model describes the events of its category well, with the exception of the VBF category, in which the low statistics make the background difficult to model.

6.3.3 Final Fit Results

The final results of the prospects study are presented here. A fit of the inclusive selection of events, with no division into the seven kinematic categories finds an expected number of 18679 signal events and 4820990 background events, making an expected significance of 8.51. This fit is shown in figure 6.5. Performing the fit across the seven categories gives improved results, which are summarised in table 6.5, summing up to a total expected significance of 9.6σ, an improvement of 12.7% over the uncategorised fit. The sum of all categories and fits is shown in figure 6.6. The final fitted value of the signal strength $\mu = N_{sig}/N_{sig}^{SM}$ is 1.00 ± 0.13.

Table 6.3: Fitted shape parameters of the signal model in each category, in addition to the inclusive fit.

Parameter	Low p_T, central	Medium p_T, central	High p_T, central	Inclusive
$< m_H >$/GeV	124.96 ± 0.05	124.89 ± 0.03	124.99 ± 0.03	124.84 ± 0.01
σ_G/GeV	1.13 ± 0.04	1.14 ± 0.03	1.62 ± 0.08	1.43 ± 0.02
σ_{CB}/GeV	1.0 ± 0.4	1.31 ± 0.02	1.04 ± 0.07	2.34 ± 0.06
α	0.3 ± 0.2	0.6 ± 0.2	1.3 ± 0.1	0.79 ± 0.07
N/GeV^{-1}	3 ± 2	1.8 ± 0.4	1.3 ± 0.1	2.0 ± 0.1
F	0.77 ± 0.07	0.72 ± 0.05	0.43 ± 0.09	0.68 ± 0.02
χ^2/d.o.f.	0.80	1.94	1.52	1.24
Parameter	Low p_T, non-central	Medium p_T, non-central	High p_T, non-central	VBF
$< m_H >$/GeV	124.80 ± 0.04	124.84 ± 0.02	124.82 ± 0.03	124.8 ± 0.1
σ_G/GeV	1.61 ± 0.04	1.56 ± 0.04	1.76 ± 0.04	1.7 ± 0.1
σ_{CB}/GeV	2.3 ± 0.2	2.3 ± 0.1	2.9 ± 0.2	2.8 ± 0.5
α	0.4 ± 0.1	0.8 ± 0.1	0.6 ± 0.1	0.7 ± 0.4
N/GeV^{-1}	6 ± 5	1.6 ± 0.2	3 ± 1	3 ± 3
F	0.79 ± 0.04	0.65 ± 0.05	0.76 ± 0.04	0.7 ± 0.1
χ^2/d.o.f.	0.68	3.23	1.18	0.33

Table 6.4: Fitted shape parameters of the background model in each category, in addition to the inclusive fit.

Parameter	Low p_T, central	Medium p_T, central	High p_T, central	Inclusive
σ_Z/GeV	0.8870 ± 0.0002	0.8780 ± 0.0003	1.1901 ± 0.0004	1.9401 ± 0.00008
a/GeV^{-1}	-0.0674 ± 0.0006	-0.0051 ± 0.0005	-0.0197 ± 0.0001	-0.02488 ± 0.00008
$1 - F_Z$	0.0273 ± 0.0008	0.01026 ± 0.00007	0.091 ± 0.001	0.0245 ± 0.0001
χ^2/d.o.f.	1.13	0.99	0.96	1.24
Parameter	Low p_T, non-central	Medium p_T, non-central	High p_T, non-central	VBF
σ_Z/GeV	1.2747 ± 0.0001	1.2407 ± 0.0002	1.4236 ± 0.0003	0.915 ± 0.002
a/GeV^{-1}	-0.4 ± 0.5	-0.0320 ± 0.0001	-0.01748 ± 0.00008	0.0067 ± 0.0007
$1 - F_Z$	0.0000 ± 0.0002	0.0418 ± 0.0005	0.0902 ± 0.0006	0.069 ± 0.001
χ^2/d.o.f.	0.89	0.82	1.14	98.1

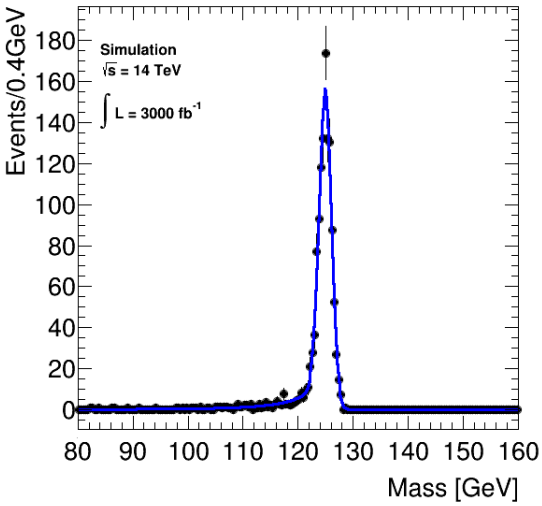

(a) Low p_T, central

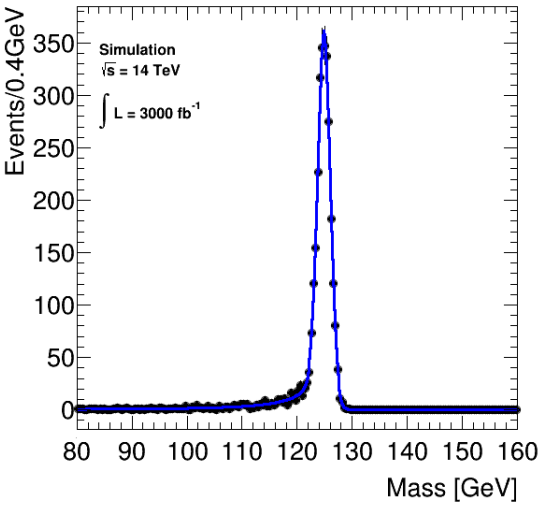

(b) Medium p_T, central

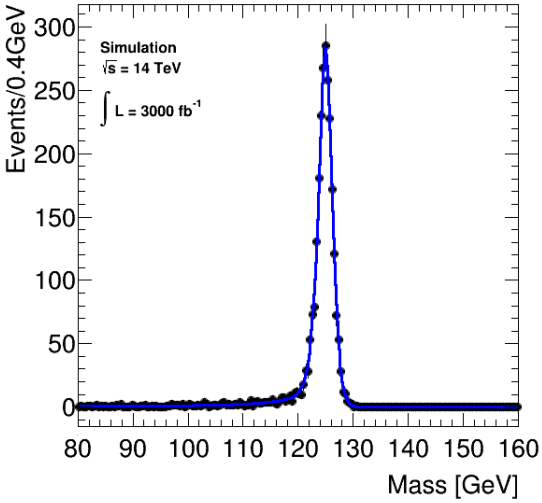

(c) High p_T, central

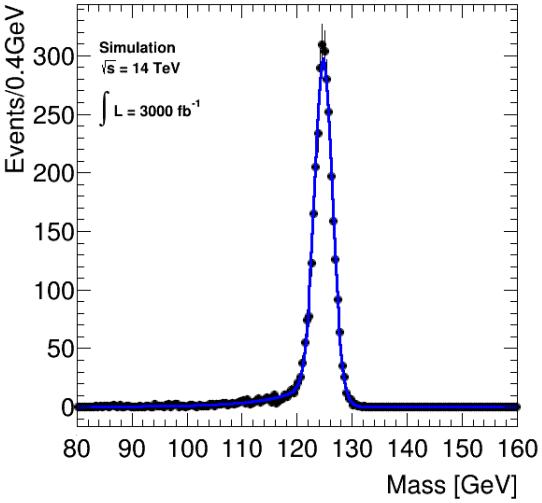

(d) Low p_T, non-central

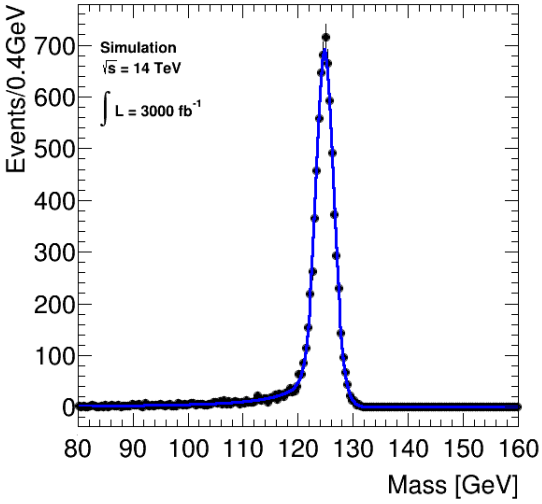

(e) Medium p_T, non-central

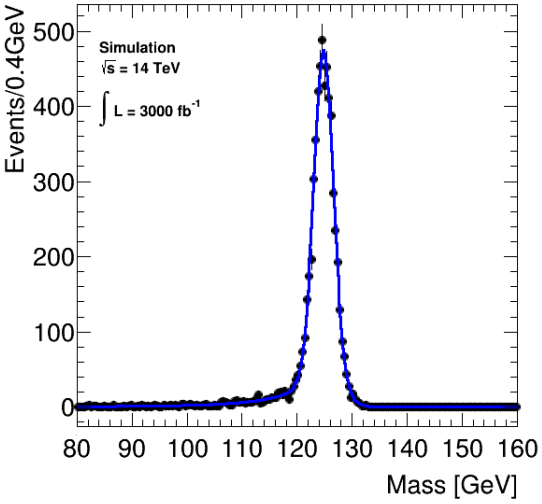

(f) High p_T, non-central

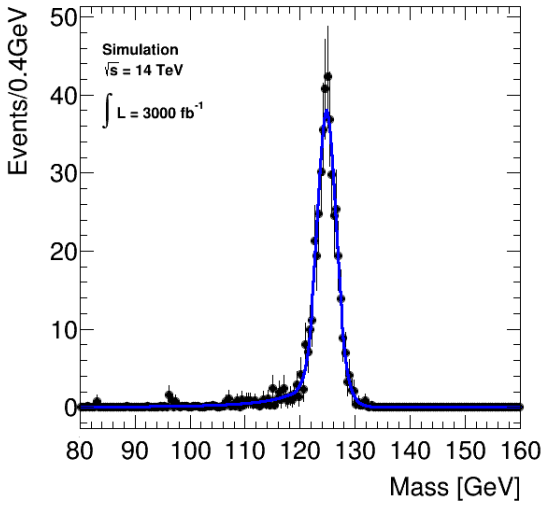

(g) VBF-like region

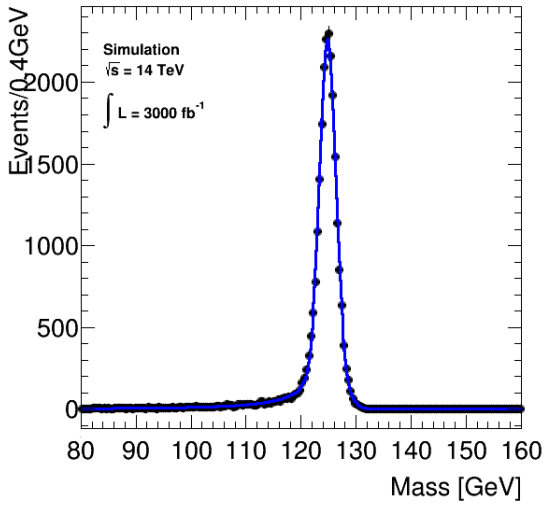

(h) Inclusive, all regions

Figure 6.3: Plots of the fitted Gaussian+Crystal Ball signal models, plotted with the signal Monte Carlo events they are fitted to

Table 6.5: The expected number of signal events and background events, and expected significance for each of the kinematic categories and for the total of the categories. The significance is defined as $\frac{N_{sig}}{\sqrt{N_{bkg}}}$. The uncertainties on N_{bkg} were not taken into account in calculating the significance, as they were observed to be similar to those expected in a Poisson distribution. The total significance is calculated as the sum in quadrature of the individual significances.

Category	N_{sig}	N_{bkg}	Significance (σ)
High p_T, central	2137 ± 49	317800 ± 590	3.79
Medium p_T, central	2283 ± 56	298490 ± 540	4.18
Low p_T, cntral	971 ± 31	337930 ± 550	1.67
High p_T, non-central	4697 ± 70	10331100 ± 1000	4.62
Medium p_T, non-central	6074 ± 74	1381800 ± 1200	5.17
Low p_T, non-central	2678 ± 57	1734600 ± 1300	2.03
VBF	361 ± 20	25100 ± 170	2.28
Total	19270 ± 140	5099000 ± 2300	9.59

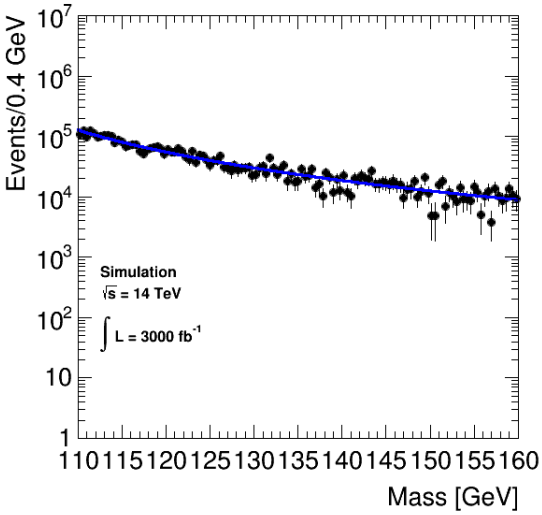

(a) Low p_T, central

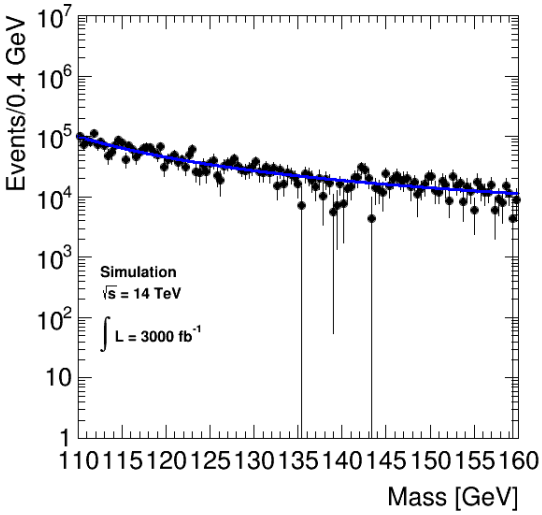

(b) Medium p_T, central

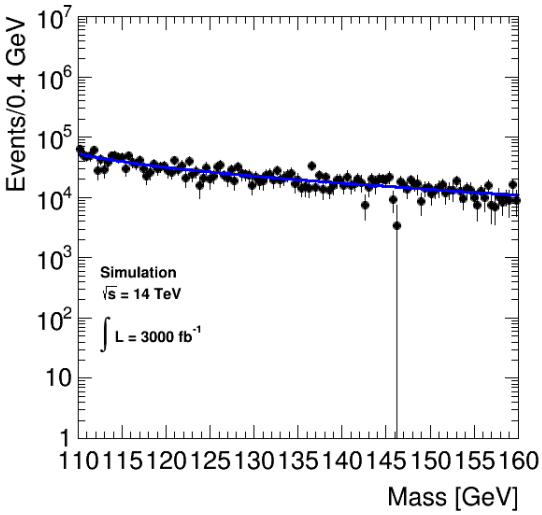

(c) High p_T, central

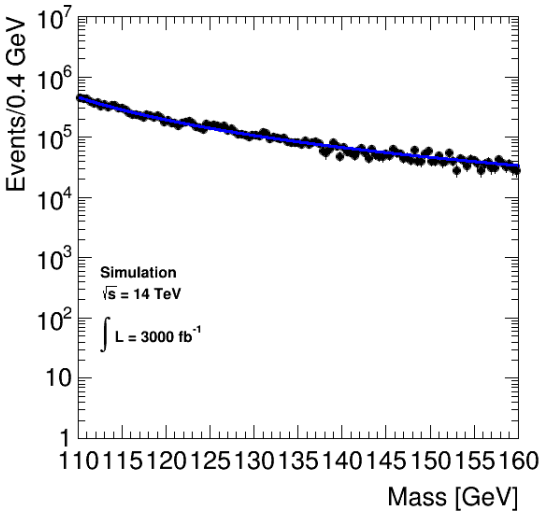

(d) Low p_T, non-central

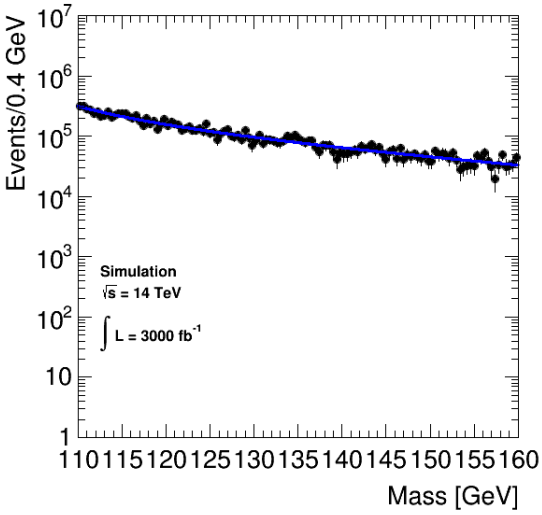

(e) Medium p_T, non-central

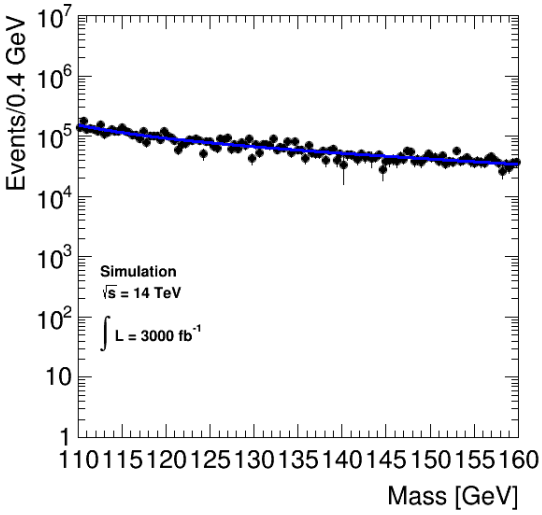

(f) High p_T, non-central

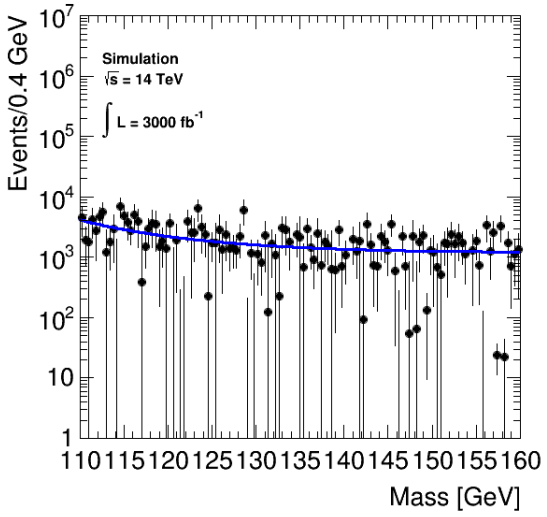

(g) VBF-like region

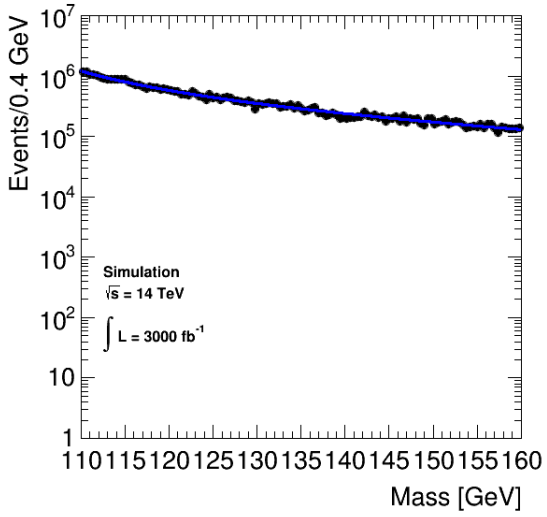

(h) Inclusive, all regions

Figure 6.4: Plots of the fitted Voigtian (Gaussian ⊗ Breit-Wigner) + exponential background models, plotted with the background Monte Carlo events they are fitted to

6.3.4 Validation of Smeared MC Samples Against Fully Simulated MC Samples

The method used in this analysis, of smearing generator level MC, is an approximation of how the Monte Carlo is used in analysis of real data, where the MC events are passed through a full simulation of the ATLAS detector. To validate the accuracy of this method, the smeared MC has been compared to a sample of fully simulated MC, for the case of the ggF signal. The fully simulated MC sample was generated using the same detector conditions that the Upgrade Performance Functions are based on, including a simulated pile-up of $< \mu >= 200$, by passing the same generated events as used to create the smeared Monte Carlo sample through a full simulation of the upgraded ATLAS detector using the GEANT4 simulation toolkit [36, 37]. These fully simulated events were then passed through the same selection as the smeared MC.

Firstly, the samples are validated by comparing the fit of the full signal model for the inclusive selection of all signal events. For this comparison a signal model is

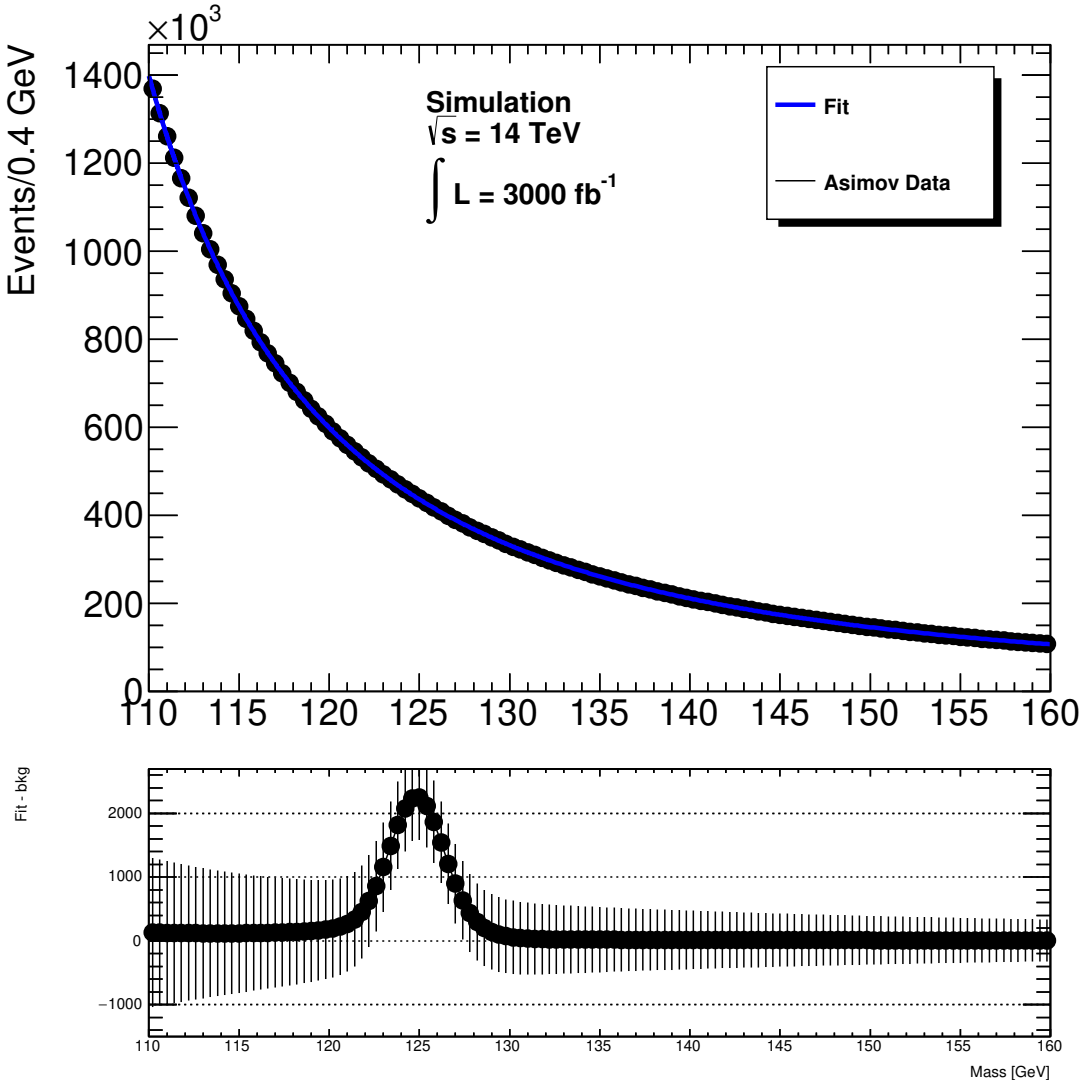

Figure 6.5: The final fitted signal + background model plotted with the Asimov data it is fitted against, in the inclusive region. Also shown is the fit with the background subtracted. As the uncertainties on each bin in the Asimov dataset are generated as $\sqrt{N}$, they are correlated with the number of events in the bin.

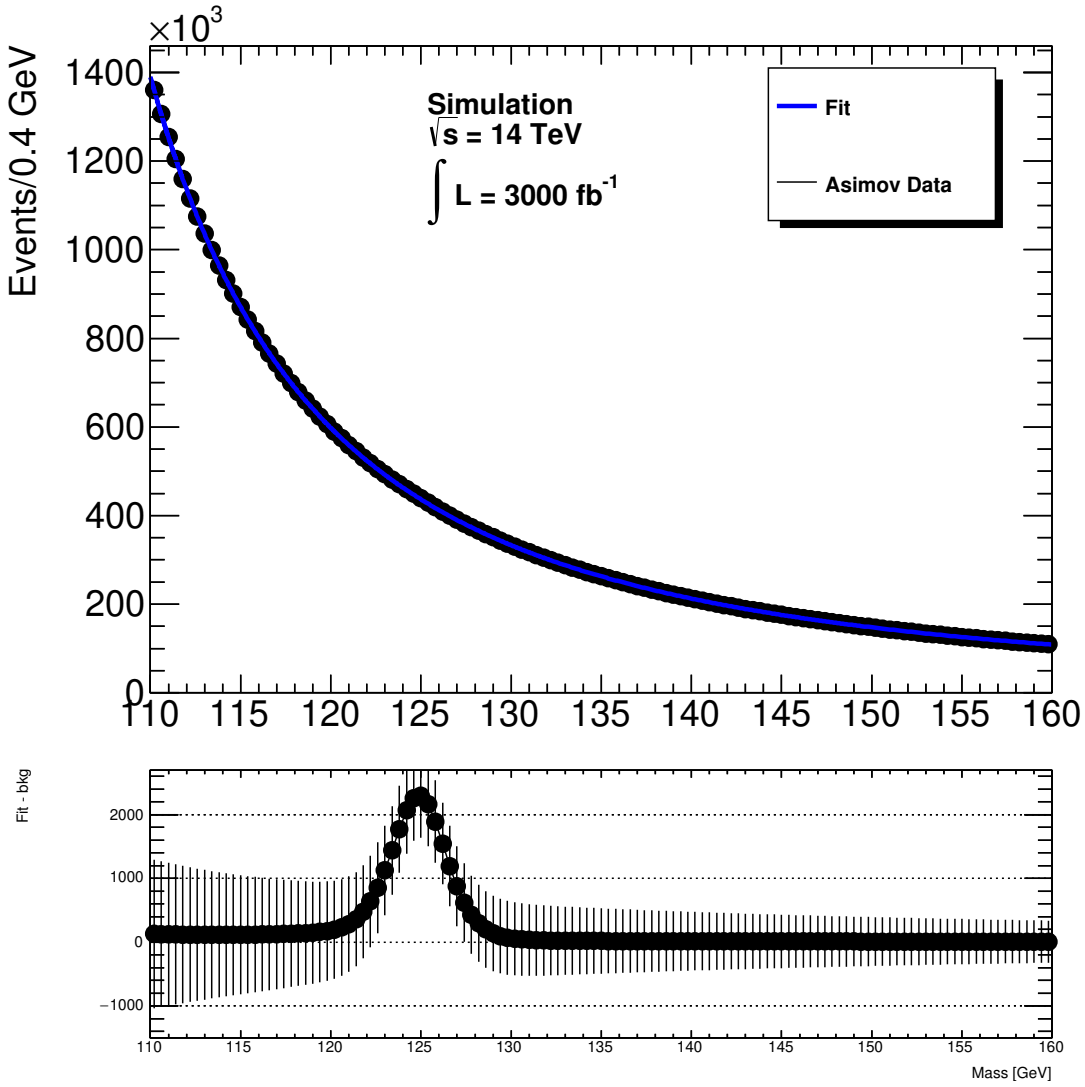

Figure 6.6: The sum of all fitted signal + background models across the seven kinematic categories, plotted with the sum of the Asimov datasets they are fitted against. Also shown is the fit with the background subtracted.

Table 6.6: The shape parameters of the fitted signal model, fitted to the smeared ggF Monte Carlo events and to the fully simulated Monte Carlo events

Parameter	Fitted Value (smeared)	Fitted Value (full simulation)
$< m_H >$/GeV	124.84 ± 0.01	124.830 ± 0.006
σ_G/GeV	1.45 ± 0.03	1.48 ± 0.01
σ_{CB}/GeV	2.34 ± 0.07	2.42 ± 0.03
α	0.7 ± 0.1	0.79 ± 0.06
N/GeV^{-1}	2.1 ± 0.3	2.4 ± 0.3
F	0.69 ± 0.03	0.66 ± 0.01
χ^2/d.o.f.	1.32	2.27

fitted to the invariant mass of the smeared ggF sample, using the same parameterization as the main analysis. This signal model was then compared to the invariant mass distribution of the fully simulated sample. The signal model, plotted with the smeared and fully simulated MC samples, is shown in figure 6.7. As the model retains a good χ^2 value of 2.27 when fitted within the uncertainty on each initially fitted parameter, this shows a good compatibility between the model and the fully simulated sample. The results of the fits are shown in table 6.6.

For further validation, the fitted mass resolution of the two samples is compared in different ranges of η. For the purposes of this comparison, a simple Gaussian fit is performed in the invariant mass range of $120 < m_{\mu\mu} < 130$ GeV, for five absolute pseudorapidity ranges: 0-1, 1-1.5, 1.5-1.9, 1.9-2.3 and 2.3-2.7. A simple Gaussian fit is used, rather than the full Gaussian plus Crystal Ball shape, because the possible mixing between the Gaussian width and the Crystal Ball width would make the results difficult to compare between different fits. The results of these fits are shown in figures 6.8, 6.9 and 6.10. It can be seen that the fully simulated samples show an approximately 3% broader resolution overall, but no substantial deviation in the ratio of the two resolutions is observed. A possible reason for the broader resolution may be the effect of muons being deflected in the calorimeter, as this effect is not included within the upgrade performance functions.

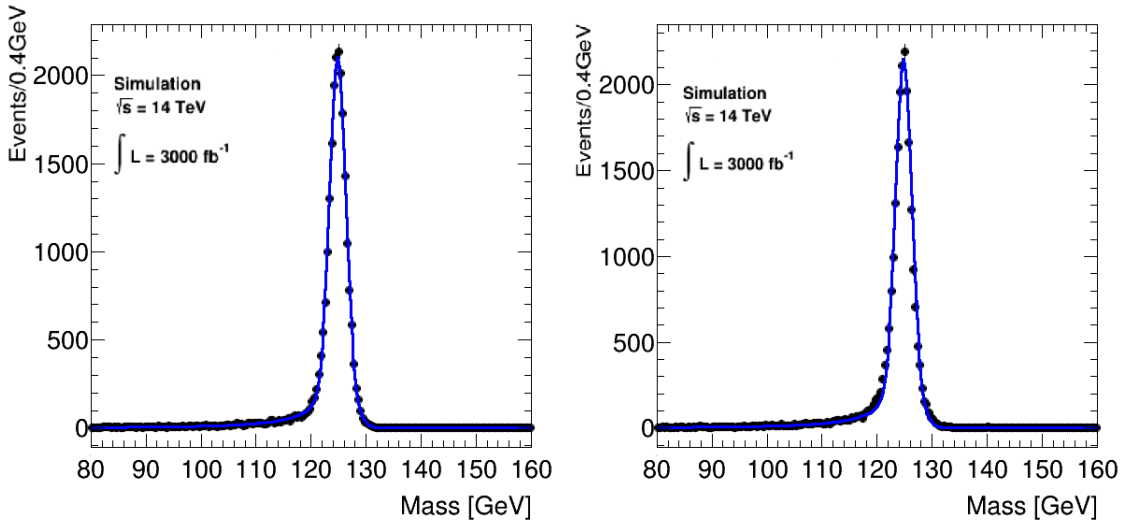

(a) (b)

Figure 6.7: The fitted signal model, for (a) the smeared ggF Monte Carlo events and (b) the fully simulated ggF Monte Carlo events

6.4 Conclusion

This study shows a promising future for the $H \to \mu\mu$ measurement at the HL-LHC. Measuring the decay with such a large significance will allow the previously unseen Yukawa coupling to muons to be measured at a precision of approximately $\pm 6.5\%$, assuming the measured branching ratio is equal to the Standard Model expectation. Not only this, but the expected improvement shown here is down to the increased luminosity alone. Many improvements could also be made to the analysis strategy, such as improved categorisation of the events using multivariate analysis. Such optimisations could feasibly improve the result further and allow even higher precision measurements to be made.

Another study [115] into the prospects of making this measurement at the HL-LHC uses an extrapolation of previous results [116] from the ongoing search for the decay in data collected by the ATLAS experiment between the years 2015-2017, at a centre of mass energy of 13 TeV. This study finds an expected fractional uncertainty of $^{+0.15}_{-0.14}$ (stat. + syst.) on the measured cross-section times branching ratio, assuming

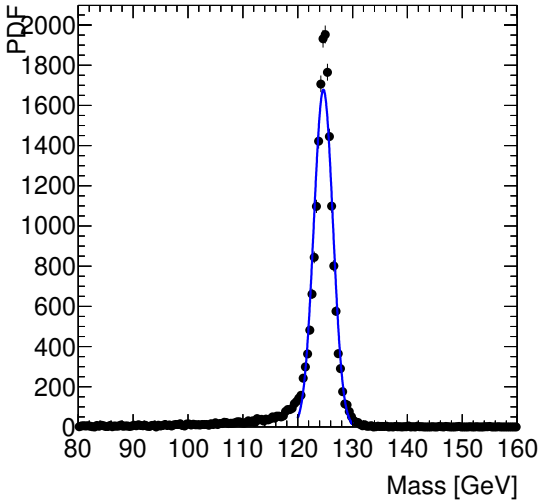

(a) $0.0 < \eta_{\mu\mu} < 1.0$

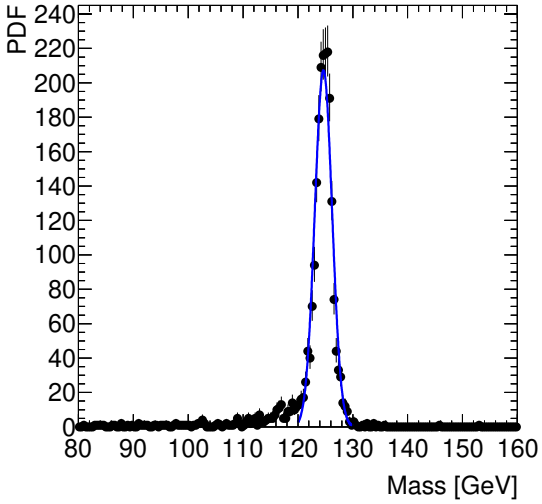

(b) $1.0 < \eta_{\mu\mu} < 1.5$

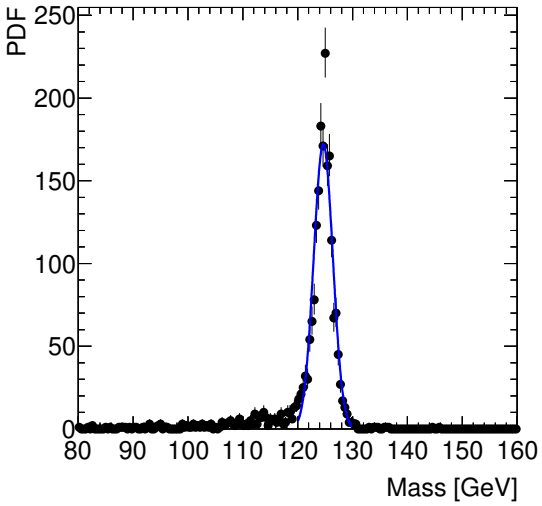

(c) $1.5 < \eta_{\mu\mu} < 1.9$

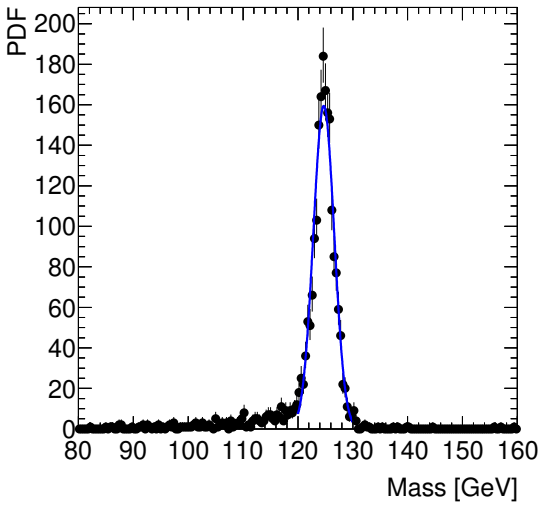

(d) $1.9 < \eta_{\mu\mu} < 2.3$

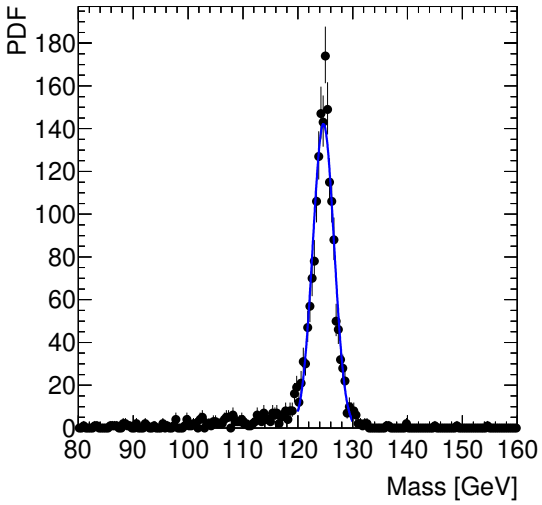

(e) $2.3 < \eta_{\mu\mu} < 2.7$

Figure 6.8: Simple Gaussian distributions fitted to the invariant mass range of fully simulated Monte Carlo events in the five η ranges.

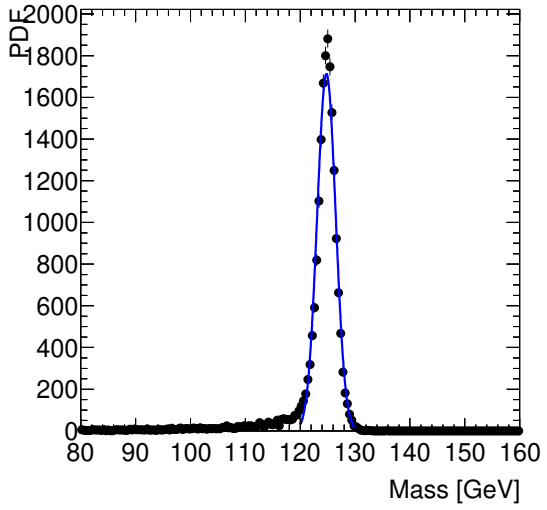

(a) $0.0 < \eta_{\mu\mu} < 1.0$

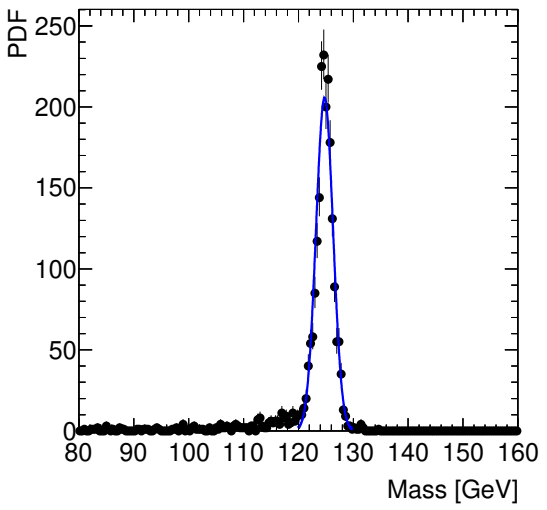

(b) $1.0 < \eta_{\mu\mu} < 1.5$

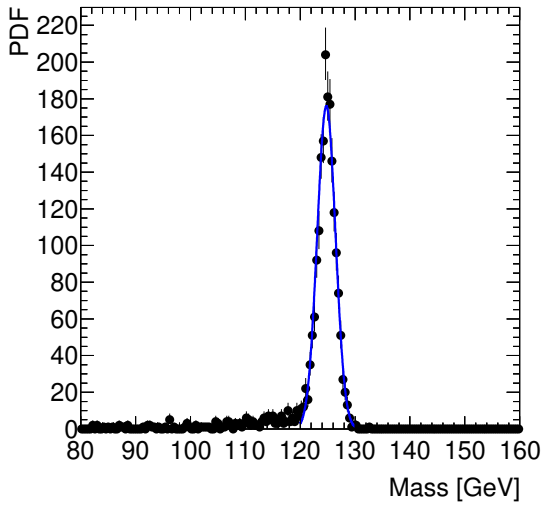

(c) $1.5 < \eta_{\mu\mu} < 1.9$

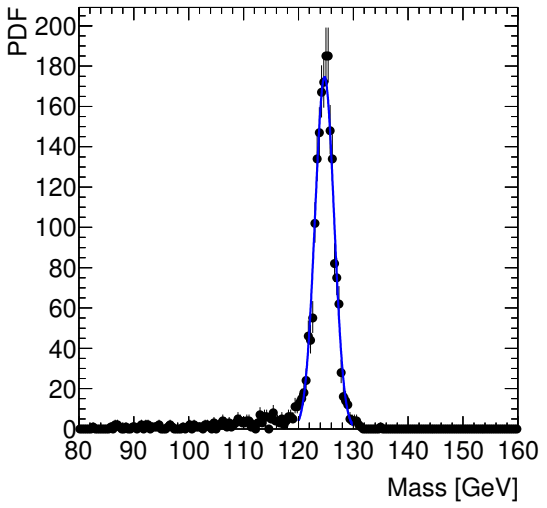

(d) $1.9 < \eta_{\mu\mu} < 2.3$

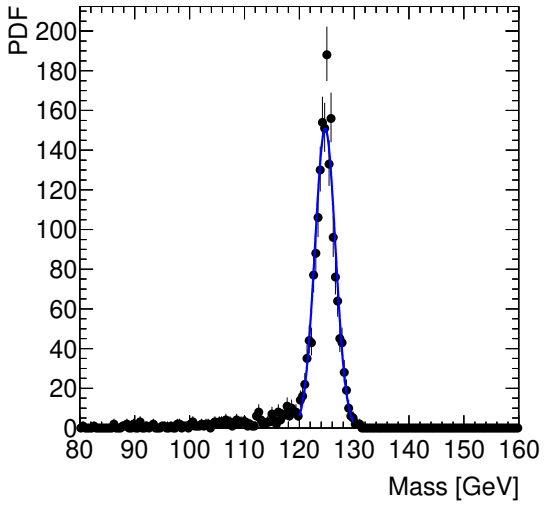

(e) $2.3 < \eta_{\mu\mu} < 2.7$

Figure 6.9: Simple Gaussian distributions fitted to the invariant mass range of smeared Monte Carlo events in the five η ranges.

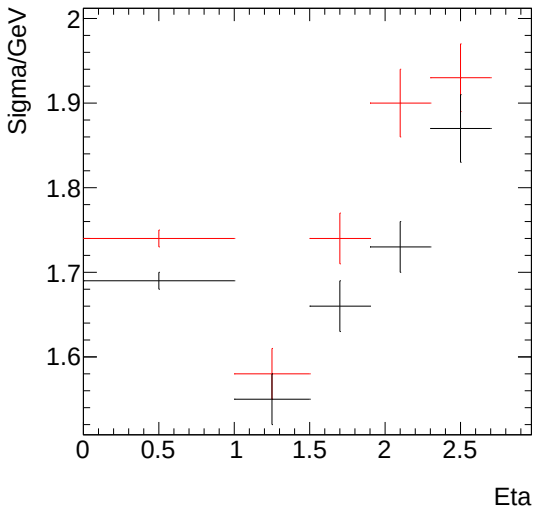

Figure 6.10: Fitted Gaussian resolution of the invariant mass against pseudorapidity (Eta) for fully simulated (red) and smeared (black) Monte Carlo events.

it is measured at the Standard Model value of 13.6 fb, compared to the result shown here with an expected fractional uncertainty of ± 0.13. This analysis uses slightly different classification, as there are two VBF categories which are defined using a boosted decision tree rather than being cut-based. The two different approaches then, despite differences in the method and the centre of mass energy being studied, show comparable results.

A precise measurement of the $H \to \mu\mu$ decay is an important step in understanding the Higgs sector as it could support or contradict the idea that the coupling of the Higgs boson to leptons depends linearly on the mass of the leptons involved. The results of this study therefore support the Physics case for pursuing this analysis at the HL-LHC.

Chapter 7

A Search for the di-electron Decay Mode of the Higgs Boson

7.1 Introduction

As discussed in the previous chapter, the couplings of the Higgs boson to first and second generation fermions are yetto be confirmed. While searches are ongoing for second generation fermionic couplings, the first generation remains largely unexplored during 13 TeV running at the LHC. The only previous result involving the Higgs coupling to first generation fermions is from CMS in 2014 [97], in which a search was performed for the $H \to e^+e^-$ decay using 8 TeV data from the LHC, and a limit of 0.0019 was set on the value of the branching ratio. This is equivalent to around 4×10^5 times the Standard Model value of 5×10^{-9}.

This chapter presents a new search for this decay using the full set of 13 TeV proton-proton collision data collected by the ATLAS detector during Run II of the LHC. This is the first search for the decay at this centre of mass energy, and the first search using the full Run II dataset, with an integrated luminosity of 139 fb^{-1}. It also represents, having been published alongside a search for the lepton flavour violating $H \to e^{\pm}\mu^{\mp}$ decay, the last of the leptonic Higgs decay searches to be performed by

ATLAS, complementing existing searches for $H \to \tau^+\tau^-$ [100], $H \to \mu^+\mu^-$ [103], and the other lepton flavour violating decays [117].

This analysis is a data-driven search using proton-proton collisions data collected by the ATLAS experiment between 2015 and 2018. Monte Carlo events are used to simulate the $H \to e^+e^-$ signal peak, for validation of the background parameterisation, and for estimation of the systematic uncertainty due to mis-modeling of the background. The main backgrounds are similar to those in the $H \to \mu^+\mu^-$ analysis in chapter 6, i.e. a combination of Drell-Yan (Z/γ^*), diboson and top events, but with electrons instead of muons in the final states. For this decay channel, however, the background due to other Higgs decays must also be taken into account, specifically the background due to $H \to \gamma\gamma$ events, where the photons can be mis-identified as electrons.

This analysis differs from the previously discussed $H \to \mu^+\mu^-$ prospects study due to the use of data over simulation, but the overall treatment of this data follows a similar process. The data and Monte Carlo events are first passed through an event selection before the selected events are split into categories to optimise the expected significance. Signal and background models are then parameterised through a fit to the invariant mass spectrum of the signal Monte Carlo and the data respectively. A final fit across all the categories is then used to calculate a limit on the $H \to e^+e^-$ branching ratio, under the assumption of Standard Model Higgs production cross sections.

7.2 Motivation for a Data-Driven Analysis

Rather than using simulated Monte Carlo events to parameterise the background, this analysis uses an analytical function that is fit to the data. The data used is required to pass the ATLAS Good-Run-List, which makes sure the data were recorded when the detector was in a good condition. In addition to this requirement, corrupted and incomplete events, in which some data from the detector is unreliable

due to problems in the SCT, liquid argon or tile calorimeter systems or missing due to restarts undertaken during physics runs, are excluded from the data. The sum of all the included events comes to a total integated luminosity of 138.8 fb^{-1}.

The use of the data for this purpose, as well as in the final fit, is motivated by the comparison between Monte Carlo events and data shown in section 7.5.1. The large background cross section makes the production of enough Monte Carlo events to accurately describe it computationally intensive, and so large discrepancies between the data and the simulation arise, both in terms of the shape of some distributions and in terms of the overall normalisation. The data-driven method used here circumvents this issue, as the background function is found through a fit to the data itself. The use of a function over the invariant mass distribution to describe the non-resonant backgrounds was previously employed in the 13 TeV search for the $H \to \mu^+\mu^-$ decay [103], and is assumed to also be valid here, due to the similar backgrounds.

Performing the analysis in this way, with data being used for both the background parameterisation and the final fit, carries the risk of introducing bias, as changes in the fitted shape of the background function could affect the number of signal events found in the results. However, this potential bias is accounted for in two different ways. The first is the use of a "blinding" in the development of the analysis, in which events within the invariant mass range of $120 < m_{ee} < 130$ GeV are ignored. Secondly, a background modeling (or "spurious signal") systematic uncertainty is included. This systematic is evaluated using a fit to a large amount of fast-simulated $Z/\gamma \to e^+e^-$ events and is explained in more detail in the section 7.8.

7.3 Monte Carlo Samples

Monte Carlo events are produced for the $H \to e^+e^-$ signal and the main backgrounds. The signal Monte Carlo events are used in the parameterisation of the signal model, while the background Monte Carlo events are used in comparisons be-

tween data and Monte Carlo, as well as in the validation of the background model. The signal events generated are for the gluon gluon fusion (ggF), vector boson fusion (VBF) and associated vector boson (WH/ZH) production processes of the Higgs boson. While the background Monte Carlo events are not used in the fit, the form of the background model is motivated by the Monte Carlo shape, and some fits are used to validate this form.

7.3.1 Signal

All the signal samples are generated using a Higgs mass of $m_H = 125$ GeV. The ggF signal sample was produced using Powheg-Box v2 [118] using the NNLOPS prescription [119], which achieves NNLO accuracy in QCD after reweighting according to the Higgs rapidity y_H. The PDF4LHC15 PDF set [31] and Pythia 8 are used for parton showering and hadronization. The VBF signal sample was produced using Powheg-Box v2 [118] at NLO in QCD, using the NNPDF3.0 parton distribution function set [120] and Pythia 8 for parton showering and hadronization. The samples for associated ZH and WH production are produced using the MiNLO [121] version of Powheg-Box [118], again interfaced to the NNPDF3.0 set and Pythia 8 for parton showering and hadronization. The production cross sections used to normalise the signal Monte Carlo samples, calculated at next-to-next-to-next-to leading order (N3LO) for ggF and at NNLO+NNLL for VBF and W/ZH, are listed in table 7.1.

7.3.2 Background

Inclusive vector boson production events are simulated using the Sherpa 2.2.1 generator. Matrix elements for up to two jets at NLO and four jets at LO are calculated using the OpenLoops [122] and Comix [123] matrix element generators. The number of expected events from each are then rescaled by a common factor using the inclusive NNLO cross-sections [124]. The samples are split according to the p_T of

Table 7.1: Production cross sections and theoretical uncertainties for the Higgs boson at $\sqrt{s} = 13$ TeV [78]. "Theory" uncertainty is interpreted as a flat 100% confidence level, whole "gaussian" is a one standard deviation range. PDF + α_s is the uncertainty due to the choice of α_s and PDF set, while QCD scale is the uncertainty due to the choice of factorisation and renormalisations scales.

Production Mode	Cross-section [pb]
ggF	$48.5^{+4.6\%}_{-6.7\%}$(theory) $\pm$ 3.9%(gaussian) $\pm$ 3.2%(PDF + α_s)
VBF	$3.8^{+0.4\%}_{-0.3\%}$(QCDscale) $\pm$ 2.1%(PDF + α_s)
WH	$1.4^{+0.5\%}_{-0.7\%}$(QCDscale) $\pm$ 1.9%(PDF + α_s)
ZH	$0.88^{+3.8\%}_{-3.0\%}$(QCDscale) $\pm$ 1.6%(PDF + α_s)

the vector boson and the $H_T = \Sigma_{\text{jets}} p_T$ of the event, using a cut at generation level that produced different slices in $max(H_T, p_T^{ll})$, where p_T^{ll} is the combined transverse momentum of the truth leptons created in the decay of the vector boson, and H_T is the sum of the transverse momenta of all jets and leptons in the event. The sliced samples are then split further, depending on whether the final state contained c or b hadrons. Finally, the $Z \to \tau\tau$ samples are split even further depending on the presence of leptonically or hadronically decaying tau leptons. In addition to this, large NLO $Z/\gamma^* \to e^+e^-$ samples are generated using POWHEG, as well as some LO $Z/\gamma^* + jj$ samples using ALPGEN, for evaluation of the background modeling uncertainty, as described in section 7.8.3.

The top-quark Monte Carlo samples (both $t\bar{t}$ events and singly produced top quarks) are generated using POWHEG-BOX v2 using CT10 PDF interfaced to PYTHIA 6.428 [125] for parton showering, using the CTEQ6L1 PDF [126] for the underlying event descriptions. The properties of the bottom and charmed hadron decays are simulated using EVTGEN v1.2.0 [127]. The mass of the top quark was set to $m_t = 172.5$ GeV. At least one top quark in each $t\bar{t}$ event was required to decay leptonically. The $t\bar{t}$ production cross section is known to NNLO accuracy in QCD including next-to-next-to-leading logarithmic (NNLL) soft gluon terms, and the reference value used to normalise the Monte Carlo events was calculated using TOP++ 2.0 [128]. The parameter HDAMP, used by POWHEG to regulate high p_T radiation, was set to m_t for improved data-Monte Carlo agreement in the high p_T region [129]. Each single top

production process (t-channel, s-channel and Wt-channel) was generated separately. The single top cross section was calculated as described in Ref. [130, 131].

The WW, WZ, and ZZ processes are simulated using SHERPA 2.2.2(2.2.1) for the fully(semi) leptonic final states. The events are generated using the NNPDF3.0 PDF set and by merging the NLO and LO calculations from Ref. [34]. The diboson processes are normalised directly to the SHERPA prediction.

7.3.3 Simulation

All simulated signal and background events are overlaid with simulated minimum bias events in order to model the effect of pileup in the detector. These events are generated using PYTHIA 8. All the samples are then processed through the full ATLAS detector simulation [132] based on GEANT4 [133], and reconstructed using the same reconstruction algorithms as used for data. Three sets of parameters are used for this simulation, to account for the changes in the amount of pile-up between the 2015/2016, 2017 and 2018 runs.

7.4 Event Selection

The data and Monte Carlo events are passed through a simple event selection designed to reduce the contributions of the different backgrounds in the signal region as well as the contribution of misidentified physics objects in the events. This section summarises the selection used, as well as the definitions of the different physics objects (in this case electrons, jets and missing transverse energy) in the analysis.

7.4.1 Electrons

As described in chapter 2, electrons are reconstructed using information from the electromagnetic calorimeter and the inner detector. Electron candidates are identified using likelihood based criteria [134, 24], chosen to give an identification efficiency of 95%. This is a loose working point as described in chapter 2. The electron candidates are then required to pass kinematic cuts of $p_T > 7$ GeV and $|\eta| < 2.47$, excluding the "crack region" of $1.37 < |\eta| < 1.52$, where the performance for electrons is degraded due to the transition between the barrel and the endcaps. A cleaning cut is then used to remove bad quality electrons, i.e. electrons identified with dead regions along the associated track. Cuts on the impact parameters of the transverse impact parameter, defined from the beam line, d_0^{BL} and the longitudinal impact parameter, defined from the primary vertex, z_0^{PV} are used to ensure the electrons come from the primary vertex of the interaction. These cuts require $|z_0^{PV}\sin(\theta)| < 0.5$ mm and $|\text{significance}(\mathrm{d}_0^{\mathrm{BL}})| = |\frac{\mathrm{d}_0^{\mathrm{BL}}}{\sigma(\mathrm{d}_0^{\mathrm{BL}})}| < 5$. Finally, a loose isolation requirement is applied, as described in the performance section. The actual cuts used in this requirement vary as a function of p_T and η, in order to maintain a 99% efficiency for the signal electrons.

7.4.2 Jets

Jet candidates are reconstructed using the anti-k_T algorithm with a distance parameter of $R = 0.4$. The energy calibration of the jets starts from the EM calorimeter cells, and is corrected for the effects of inactive material, the dependence on jet structures, and for any leakage outside the calorimeter. Reconstructed jets in this analysis are required to have $p_T > 30$ GeV and $|\eta| < 4.5$. A further cut of "BadLoose" [135] jets is then used to reject fake jets caused by noise in the LAr calorimeters. Many quantities are used in this selection, including pulse shape in the LAr calorimeter cells, the ratio of energy deposited in a single cell over total energy of the jet, and the ratio of the jet p_T under the sum of the momenta of its constituent tracks. The

specific values of the cuts are chosen to give an efficiency of 99.5% for $p_T > 20$ GeV jets.

The next step in the jet selection is to distinguish between pile-up jets and hard scattering jets, and cut out as many pile-up jets as possible. Here this is done using the Jet Vertex Tagger (JVT) [136]. The JVT is a likelihood variable calculated as a multivariate combination of two discriminating variables on the jet's associated tracks. The first discriminating variable is the ratio of the scalar p_T sum of tracks originating from the primary vertex over the scalar p_T sum of all tracks (JVF) and the second is the ratio of the scalar p_T sum of tracks originating from the primary vertex over the jet p_T (R_{pT}). Jets are required to either have $p_T > 60$ GeV, or $|\eta| > 2.4$, or are required to have a JVT score of JVT$>$ 0.59. This score has an efficiency of 92% for hard scattering jets and will reject up to 98% of pile-up. The selected jets are used in the event selection, as well as in the definition of the "VBF-like" signal region.

7.4.3 Overlap Removal

An overlap removal process is used to make sure no potential particles are double counted as two different kinds of object. This is carried out in three steps. First, any selected electrons sharing an ID track with a muon candidate are ignored, as this could indicate the muon being duplicated as an electron, due to radiation of a photon. Secondly, jets are removed if they are found within $\Delta R < 0.2$ of an electron or if they have less than three tracks and are within $\Delta R < 0.4$ of a muon, as such a signature is likely due to a prompt muon emitting a photon as radiation. Finally, any electron candidates are removed if they are found within $\Delta R < 0.4$ of any of the remaining jets.

7.4.4 Events

The events, in both the data and the Monte Carlo, that are selected are those triggered by a single electron trigger. The thresholds for these triggers vary based on the year in which the data was recorded. In general, these triggers depend on the measured E_T of the electron, as well as identification, and in some cases isolation requirements. Typically a balance is found between the E_T cut and the ID requirements, with higher energy electrons requiring less ID quality to activate a trigger. The triggers used are listed in table 7.2. The signal region is then defined by a series of linear cuts. Firstly, events are required to have a primary vertex with at least two associated tracks, which are selected in the inner detector with $p_T > 400$ MeV and $|\eta| < 2.5$. The primary vertex is defined as the reconstructed vertex with the highest value of $\Sigma_i p_{Ti}^2$ across all its associated tracks. Trigger matching is then applied to the events, which requires either of the selected electrons to be within $\Delta R < 0.1$ of the electron that caused the trigger to fire.

Events are required to contain exactly two electrons as defined earlier, and events with three or more are discarded. The leading electron must have $p_T > 27$ GeV and the subleading must have $p_T > 15$ GeV. This assists with the trigger matching and reduces the background due to hadrons or photons being misidentified as electrons. The electrons are also required to have opposite charge.

To reduce the background due to $t\bar{t}$ and diboson events, a veto on missing transverse energy (E_T^{miss}) is used. This is used due to the fact that the signal process contains no real E_T^{miss}, whereas the $t\bar{t}$ and diboson processes both may contain neutrinos in their decay chains, which lead to a measured E_T^{miss}. Here, E_T^{miss} is defined as the negative vectorial sum of the transverse momenta of all the reconstructed physics objects, in addition to a "soft term" built from inner detector tracks not associated to any object. The cut, performed on the significance of the missing transverse energy, is quantified as $Sig(E_T^{miss}) = E_T^{miss}/\sqrt{H_T} < 3.5$ GeV$^{1/2}$. Background from $t\bar{t}$ is supressed even further by a veto on events containing one or more b-tagged jet.

Table 7.2: Electron triggers used in the analysis. In the trigger names, the number after "e" represents the p_T requirement, and the following strings describe identification quality requirements of the trigger. The performance of these triggers is described in detail in [138].

Year	Trigger
2015	HLT_e24_lhmedium_L1EM20VH
2015	HLT_e60_lhmedium
2015	HLT_e120_lhloose
2016 - 2018	HLT_e26_lhtight_nod0_ivarloose
2016 - 2018	HLT_e60_lhmedium_nod0
2016 - 2018	HLT_e140_lhloose_nod0
2016 - 2018	HLT_e300_etcut

The b-jets are tagged using the MV2c10 tagger [137] selection at the 60% efficiency working point.

The signal region is then defined in terms of the di-electron invariant mass as $110 < m_{ee} < 160$ GeV.

7.5 Event Classification

The signal region is divided into 7 sub-regions, which have different fractions of signal events, in order to improve the overall signal sensitivity of the analysis.

The first of the regions is chosen to select signal events that were produced by VBF. This region takes priority over the other 6 regions, and so this selection is performed first. The "VBF-like" region is defined by selecting events with two opposite hemisphere jets with a large separation and large invariant mass:

- $\eta_{J1} \times \eta_{J2} < 0$
- $\Delta(\eta_{J1}, \eta_{J2}) > 3$
- $m_{JJ} > 500$ GeV.

Events that do not make it into the VBF-like region are split into the remaining 6 regions based on the electron kinematics. Firstly, they are split into a "central" category (both electrons are within the pseudorapidity range of $-1.0 < \eta < 1.0$) and a "forward" category (one or both electrons are outside of this range). Each of these categories is then further split up into a high, medium and low p_T^{ll} category, with boundaries at 15 GeV and 50 GeV. These categories are chosen to take advantage of the improved resolution in central regions of the detector, as well as at low electron p_T, in order to improve the sensitivity of the final results.

7.5.1 Data/Monte Carlo Comparisons in the Signal Regions

In this section the data collected between 2015-2018 is compared with the generated Monte Carlo events scaled to the corresponding integrated luminosity of 139 fb^{-1}. The comparisons shown are of the sum of all seven signal categories, after the event selection has been performed. The background Monte Carlo samples in these plots are normalised to the Standard Model cross-sections, calculated as described in section 7.3. Figure 7.1 shows the di-electron invariant mass spectrum for an extended range of m_{ee}. Figure 7.2 shows the p_T, η and ϕ distributions of the leading and sub-leading electrons in selected events, in the signal region invariant mass range of $110 < m_{ee} < 160$ GeV. In all of these comparisons, it can be seen that the data typically lies above the Monte Carlo predictions. While the ratio between data and Monte Carlo is fairly flat for the electron η and ϕ, as well as the leading electron p_T, this is not the case for the invariant mass or the sub-leading electron p_T.

Figure 7.3 shows the E_T^{miss}, $Sig(E_T^{miss})$ and p_T^{ee} distributions of selected events in the signal region. The E_T^{miss} and $Sig(E_T^{miss})$ distributions are shown to be poorly described by the Monte Carlo events. However, the E_T^{miss} cut in the analysis is quite loose. The p_T^{ee} distribution is slightly better described, although the Monte Carlo still underestimates the overall number of events.

Overall, the discrepancies between data and Monte Carlo can be down to a number

of other factors than the statistical uncertainty. For instance, the comparisons shown here do not include any estimate of systematic uncertainties or of the background due to particles that are misidentified as electrons. However, as the number of Monte Carlo events is not substantially larger than the number of data events, the use of a data-driven background estimation is chosen for this analysis.

7.6 Signal Model

The signal in this analysis is modeled, as in the $H \to \mu^+\mu^-$ prospects analysis from chapter 6, as the sum of a Crystal Ball function and a Gaussian function:

$$f_s(m_{ee}; f, \mu_C, \sigma_C, \alpha, n, \sigma_G) = (1-f)\cdot CB(m_{ee}; \mu_C, \sigma_C, \alpha, n) + f\cdot G(m_{ee}; \mu_G, \sigma_G) \quad (7.1)$$

where f is the fractional contribution of the Gaussian, μ_C is the mean value of the Crystal Ball function in GeV, σ_C is the width of the Crystal Ball function in GeV, α is the "cut-off" parameter of the Crystal Ball functionin units of σ_C, n is the "slope" parameter of the Crystal Ball function in GeV^{-1}, μ_G is the mean of the Gaussian in GeV, and σ_G is the width of the Gaussian in GeV. Here, the Gaussian represents the detector resolution, and the addition of the Crystal Ball function allows the model to correct for the effect of final state radiation.

The values for the different signal parameters vary depending on the signal category. Across all seven categories, the value of n is fixed to 1. The choice of a constant value for n reduces the degeneracy of the fit, and a value of 1 is thought to describe most $H \to ll$ distributions reasonably. The remaining values are found via a fit to the di-electron invariant mass of the signal (a sum of ggF, VBF and VH) Monte Carlo events in each category. The results of these fits are shown in figure 7.4. From these fits it can be seen that the choice a fixed value for n does not result in a poor description of the signal Monte Carlo events, as the tails of the invariant mass distributions are well described.

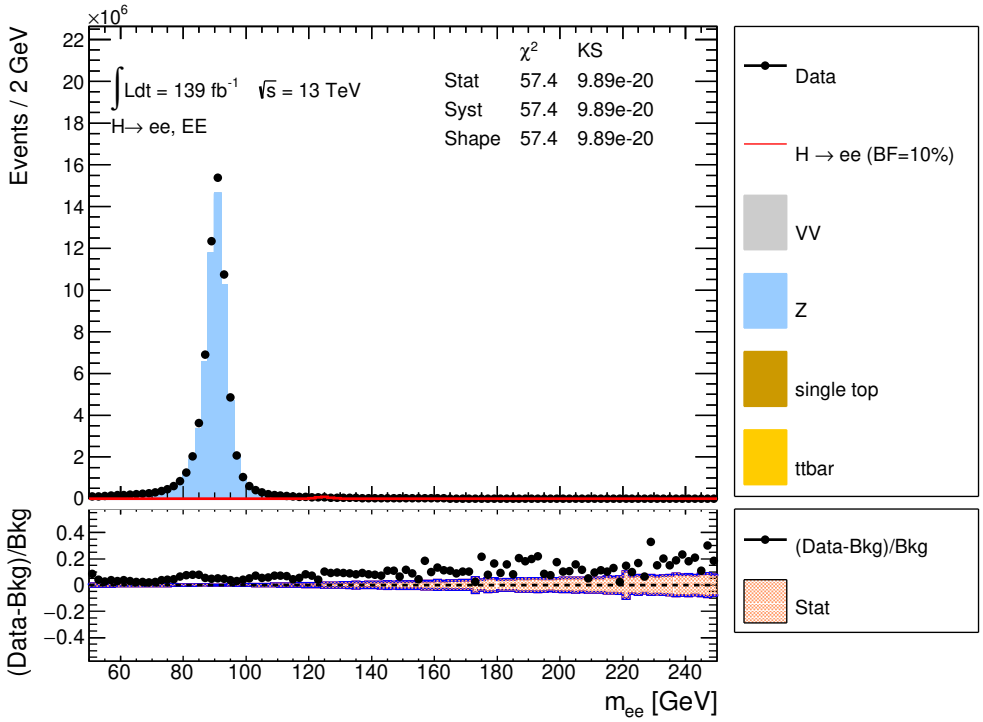

(a)

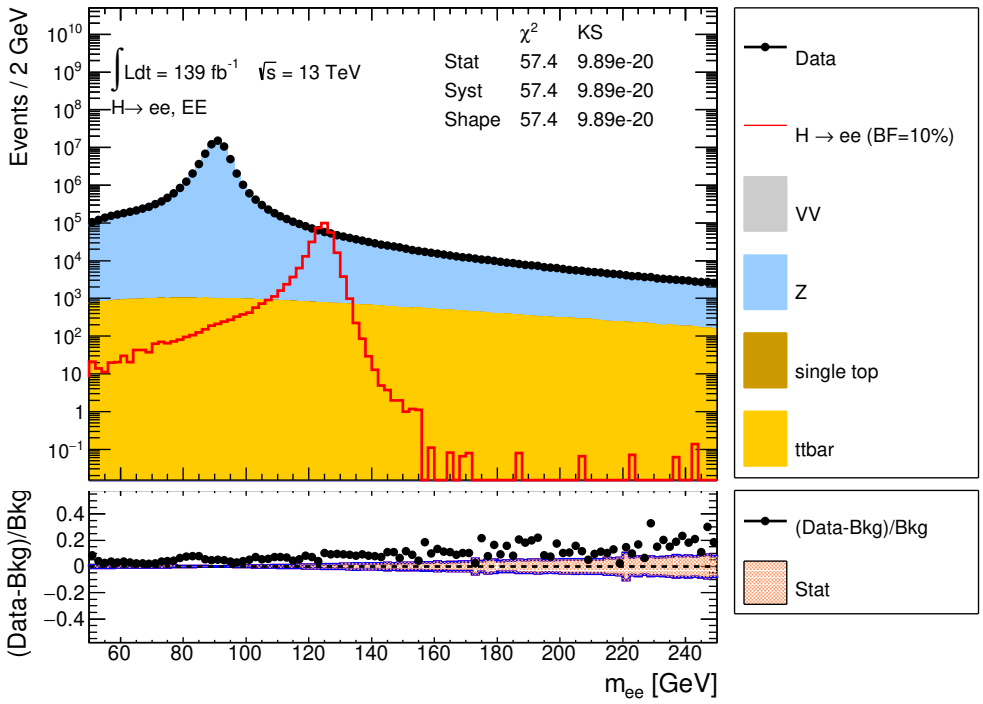

(b)

Figure 7.1: Comparison between data and Monte Carlo predictions of the m_{ee} distrubution for data collected between 2015 and 2018. The distribution is shown on both a linear and logarithmic scale. The error bands in the ratio plot represent the statistical uncertainty on the Monte Carlo events

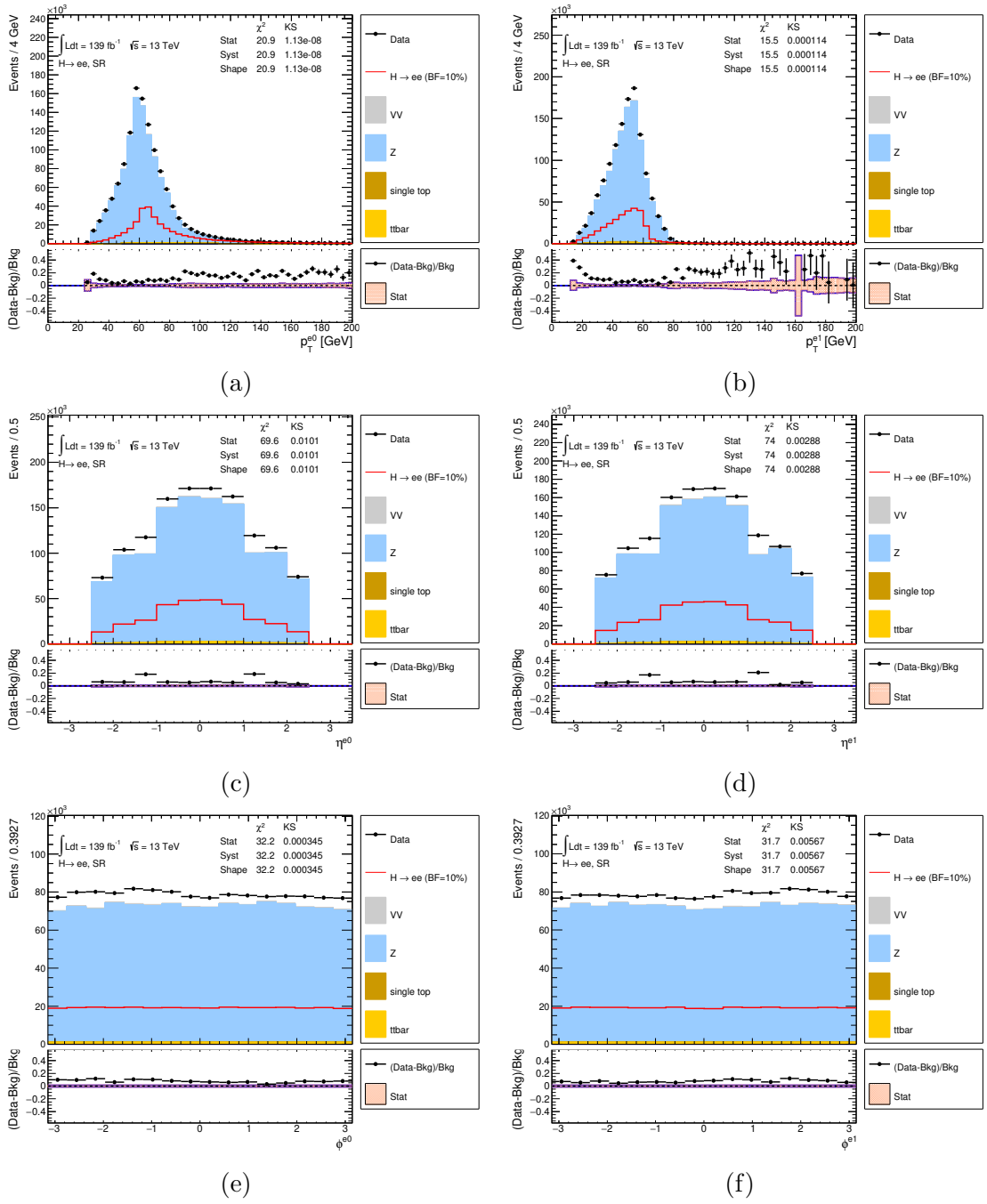

Figure 7.2: Comparison between data and Monte Carlo predictions of the p_T (a,b), η (c,d) and ϕ (e,f) distributions of the two electrons for data collected between 2015 and 2018.

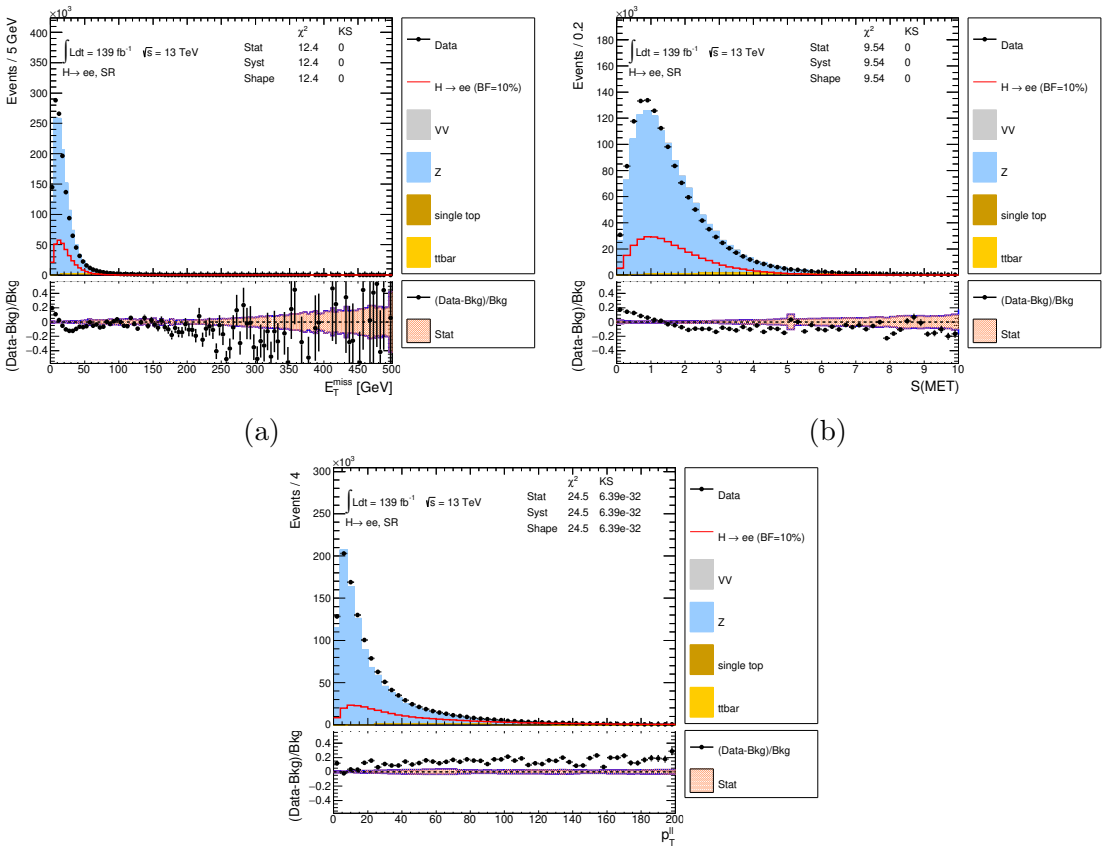

Figure 7.3: Comparison between data and Monte Carlo predictions of the E_T^{miss} (a), $S(E_T^{miss})$ (b) and p_T^{ee} (c) distributions for data collected between 2015 and 2018

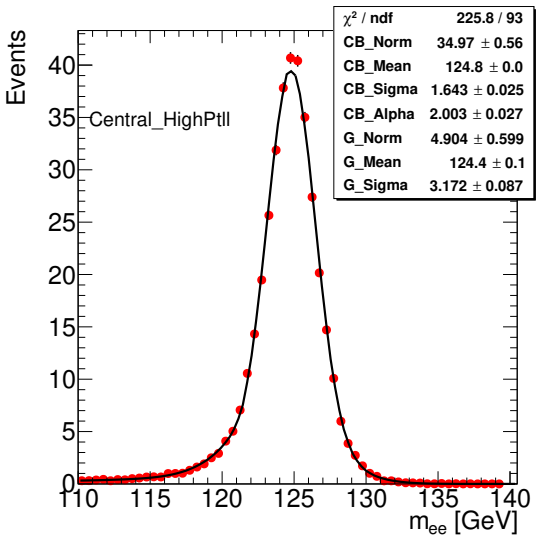

(a) Central, $p_T^{ee} > 50$ GeV

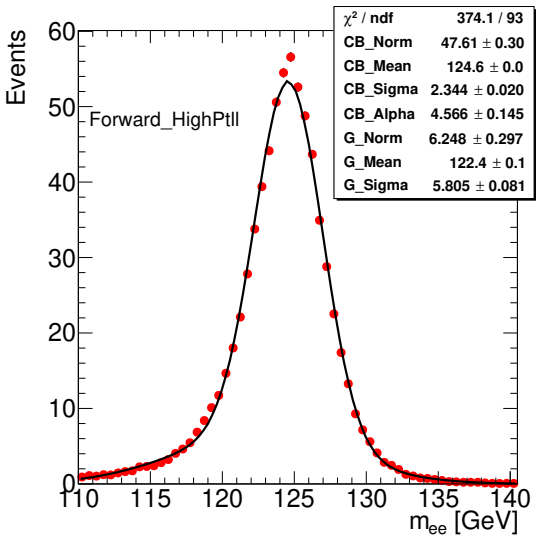

(b) Forward, $p_T^{ee} > 50$ GeV

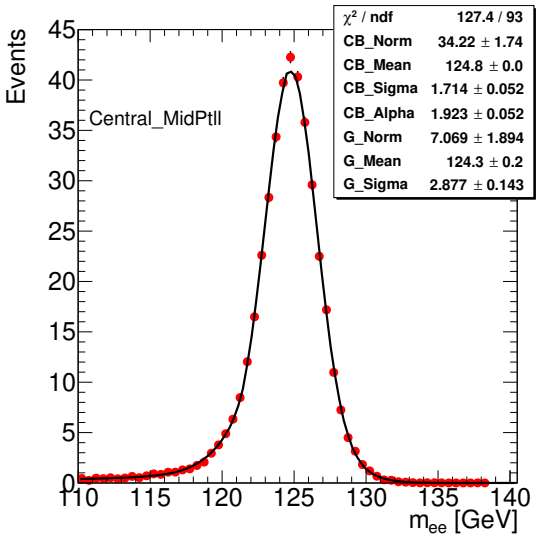

(c) Central, $15 < p_T^{ee} < 50$ GeV

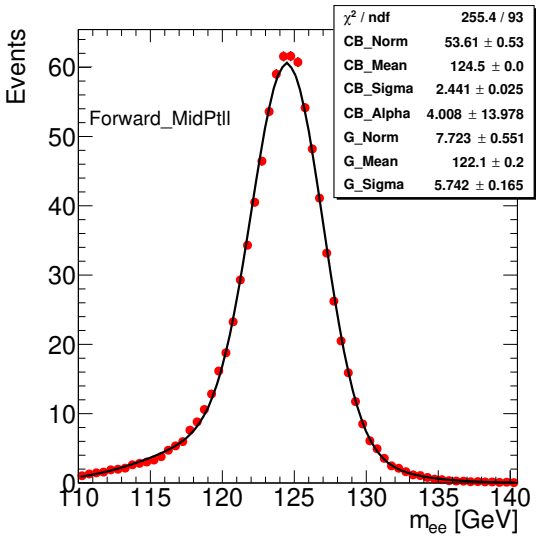

(d) Forward, $15 < p_T^{ee} < 50$ GeV

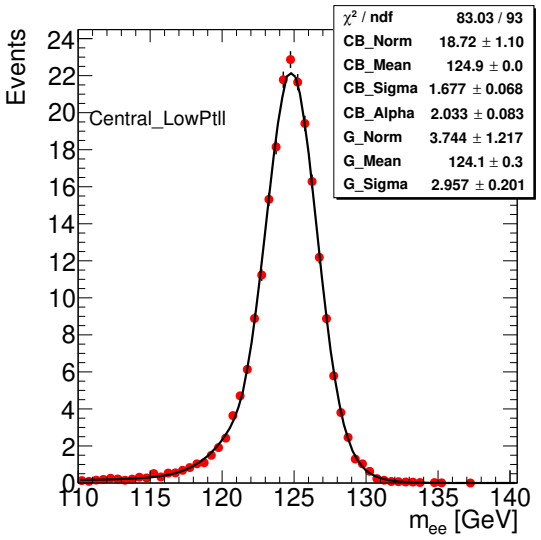

(e) Central, $p_T^{ee} < 15$ GeV

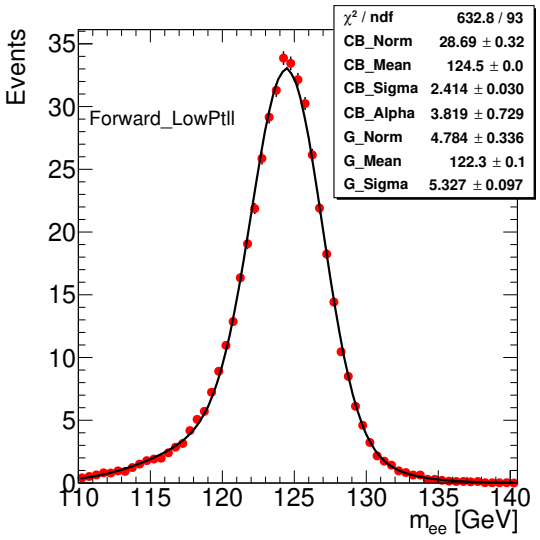

(f) Forward, $p_T^{ee} < 15$ GeV

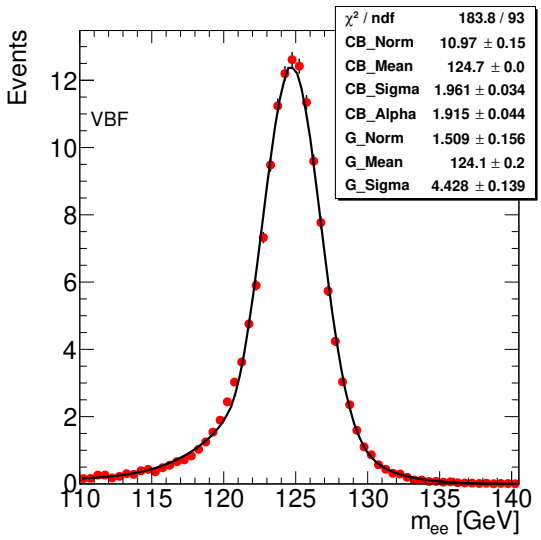

(g) VBF category

Figure 7.4: Invariant mass distributions of the signal Monte Carlo events fitted with the signal model PDF in the different signal categories. The fitted parameters of the signal model are shown in each plot.

7.7 Background Model

The background model used is an empirical model that takes into account the Z/γ^* line shape, with an additional term to correct for the di-boson and top quark backgrounds. This consists of a Breit-Wigner peak convolved with a Gaussian function to describe the Z/γ^* peak and a di-boson plus top term consisting of an exponential divided by invariant mass cubed:

$$f_B(m_{ee}) = f \cdot (BW(m_{ee}; M_Z, \Gamma_Z) \otimes G(m_{ee}; M_Z, \sigma_G)) + (1-f)C\frac{e^{Bm_{ee}}}{m_{ee}^3}, \qquad (7.2)$$

where C is a normalisation coefficient with units of m^3, chosen so the exponential term of the equation normalises to unity. The values of M_Z and Γ_Z are fixed to the known values of the Z peak, 91.2 GeV and 2.49 GeV respectively. The Gaussian width σ_G, which parameterises the width of the Z peak due to the detector resolution, is fixed in each category, with its value obtained by a Gaussian fit to the difference between reconstructed and truth level m_{ee} in the signal MC events of each category.

Table 7.3: Fitted σ_G values used in the background model in each signal region

Category	σ_G/GeV
Central, low p_T^{ee}	1.87 ± 0.05
Central, medium p_T^{ee}	1.92 ± 0.07
Central, high p_T^{ee}	1.82 ± 0.05
Forward, low p_T^{ee}	2.89 ± 0.09
Forward, medium p_T^{ee}	2.88 ± 0.08
Forward, high p_T^{ee}	2.80 ± 0.05
VBF-like	2.49 ± 0.05

The values of σ_G used are shown in table 7.3. It can be seen that the resolution does not vary greatly with p_T, however there is a larger discrepancy between the central and forward regions. The remaining parameters are the fractional contribution of the Z/γ^*, f, and the exponential parameter, B. These are left to float in ranges of 0 to 1 and -1 to 1 GeV^{-1} respectively. While positive values of B could result in a background that increases with invariant mass, the factor of m_{ee}^3 prevents this. This choice of model follows the choice in [103], due to the similarity of the backgrounds of the two analyses. Background only fits excluding the signal region of $120 < m_{ee} < 130$ GeV are shown in chapter 8.

7.7.1 $H \to \gamma\gamma$ Background

In this analysis, unlike other $H \to ll$ analyses, there is an expected background from the $H \to \gamma\gamma$ decay, with either both photons or one photon and one pileup jet being misidentified as electrons. Although the probability of misidentifying an object as an electron is very low (less than 0.8% for a loose identification working point, as seen in chapter 2), the $H \to \gamma\gamma$ branching fraction is a factor of 6 larger than the expected limits from this analysis, so the background must be considered. The overall contribution of the decay is estimated by comparing the invariant mass spectrum of signal Monte Carlo events with that of a simulated sample of $H \to \gamma\gamma$ events. Figure 7.5 shows this comparison for the ggF and VBF processes. The comparison shows that the $H \to \gamma\gamma$ events peak at a lower invariant mass than the

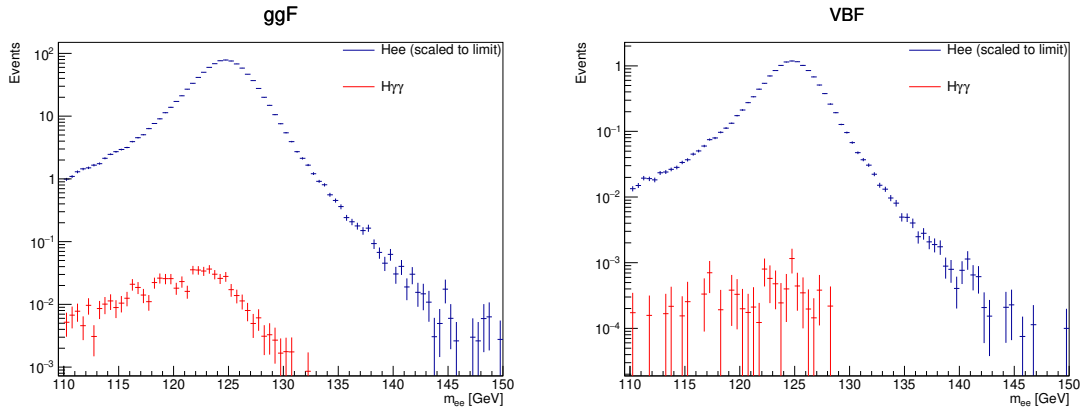

(a) (b)

Figure 7.5: Comparison of the $H \to ee$ and $H \to \gamma\gamma$ processes as a function of the invariant mass of the electron candidates for (a) ggF and (b) VBF processes.

signal events. The $H \to \gamma\gamma$ events also only contribute a very small event yield after the selection, 0.07% of that of the signal Monte Carlo events after scaling the branching ratio to the expected limit. This corresponds to a $\gamma \to e$ mis-identification rate of around 0.6 %. The $H \to \gamma\gamma$ background is therefore neglected and not included in the background model of the analysis. However, the background must be considered in future $H \to e^+e^-$ analyses, as the contribution shown here is larger than the expected Standard Model $H \to e^+e^-$ signal.

7.8 Systematics

There are three main sources of systematic uncertainty in this analysis: the theoretical uncertainties on the signal normalisation, the experimental uncertainties on the signal selection efficiency, and the uncertainty due to mismodelling of the background. As the background model is derived using a data driven method, the detector based systematics for the background do not need to be considered.

For each source of systematic uncertainty, the signal model is re-evaluated for shifts of $\pm 1\sigma$ from the nominal value. From this, the signal normalisation and shape at intermediate shift values is interpolated. Each uncertainty is then represented by a

nuisance parameter in the final fit, representing the shift value for that systematic. For the majority of systematics, the overall shape of the signal is assumed to remain the same and only the normalisation is varied between fits. However, for the electron energy scale and resolution systematics, both the lineshape and normalisation are allowed to vary.

7.8.1 Theoretical Uncertainties on the Signal

The theoretical systematic uncertainties are evaluated through their effect on the signal acceptance, defined as the ratio of the number of selected events in a given category over the total number of truth events in that category before any cuts are applied. The uncertainty on the acceptance is evaluated from the ratio of the acceptance when applying systematic variations to the nominal acceptance.

The effect due to uncertainties on the QCD factorisation and renormalisation scales, parton distribution functions, underlying event tune and parton showering are evaluated using truth level data. The acceptance for each uncertainty is calculated by implementing the event selection of the analysis on the corresponding truth level quantitites, created from the event generation of the different signal Monte Carlo samples.

The theoretical calculations of the uncertainties due to the QCD scale for the ggF process include a total of 26 variations, made up of 8 uncertainties from the POWHEG MiNLO [121] renormalisation and factorisation scales evaluated at nominal, up and down variations, in addition to up and down NNLO variations for the nominal MiNLO scale. The variations that give the largest deviations are chosen as the nuisance parameters. Using the nuisance parameters that give largest deviations means they give correlations between the event categories. For the NNLO variations, the chosen variation is the downward variation "nnlops-nnloDn-pwgNomNom" is described by the nuisance parameter QCDscale_ggF_NNLO in the fit. In the MiNLO variations, the chosen combination is that where both the renormalisation and fac-

torisation are scaled upwards, "nnlops-nnloNom-pwgUpUp". This is described in the fit by the nuisance parameter QCDscale_ggF_NLO.

The QCD scale uncertainty for VBF production is estimated from the factorisation and renormalisation variations of the NLO calculation, and is much smaller than the corresponding ggF uncertainty. The corresponding nuisance parameter is QCDscale_qqH and the uncertainty on the acceptance due to these variations has a value of 0.5%. The PDF and α_s uncertainties are calculated using the PDF4LHC15 [31] recommendations and are also found to be small. The effects of these uncertainties on the ggF and VBF processes are described by the nuisance parameters pdf_gg and pdf_qqbar respectively. The uncertainties due to the QCD scales, PDFs and α_s for the ggF process are shown in figure 7.6.

The uncertainty due to the underlying event tune, multi-parton interactions (MPI) and parton shower (PS) modelling is estimated by showering the events using different tuning parameters and different models. The nominal signal samples are generated using POWHEG and PYTHIA using the AZNLO tune [139] which has two systematic variations covering the initial state radiation (ISR) uncertainties. For the final state radiation (FSR) variations of 2 σ above and 2 σ below the nominal value are considered on the renormalisation (Ren) and MPI cut-off variables. The PS uncertainty is estimated by showering the events using HERWIG7 [140, 141] instead of PYTHIA. The uncertainty on the ggF and VBF acceptance due to the various showering parameters is shown in figure 7.7.

Finally, the uncertainties on the Higgs boson production cross-sections, shown in table 7.1, are taken into account. These amount to fractional uncertainties on the production cross-section of $\pm 4.8\%$ due to the ggF process and $\pm 3\%$ due to the VBF process. The uncertainties on the other production processes are neglected due to their lower overall cross-section. The nuisance parameters for these uncertainties are sig_ggF and sig_VBF.

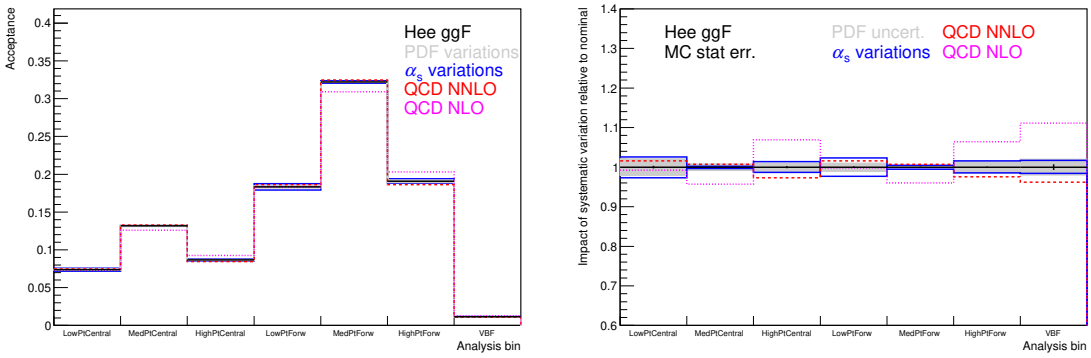

(a) (b)

Figure 7.6: The acceptance (a) and theoretical uncertainty on the acceptance (b) due to QCD scale variations for the ggF process.

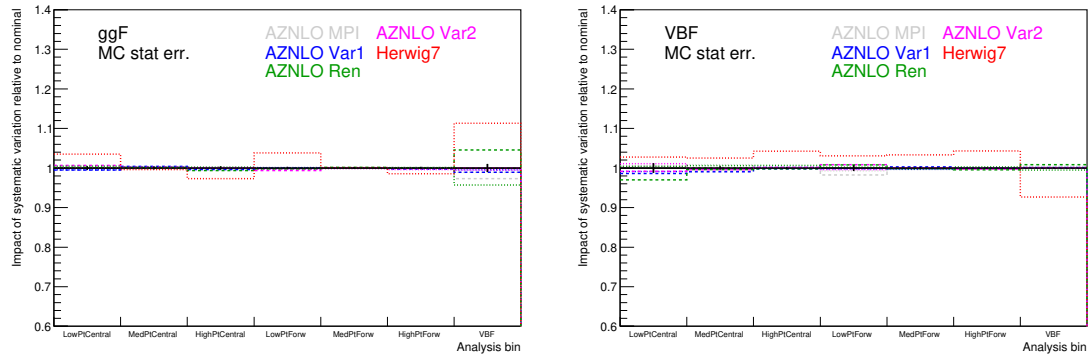

(a) (b)

Figure 7.7: The uncertainty on the signal acceptance due to parton shower effects for the ggF (a) and VBF (b) processes.

7.8.2 Experimental Uncertainties on the Signal

Experimental uncertainties are evaluated using signal MC samples with systematically varied calibrations, such as an alternative electron energy scale, to account for uncertainties in the calibrations themselves. A new signal fit is performed on the recalibrated Monte Carlo events, and if all the fitted shape parameters are in agreement with the nominal fit (within the uncertainties of the fit), the systematic is treated as affecting normalisation only. If not, then the shape parameters in the signal model are replaced with functions dependent on the values of the associated nuisance parameters, interpolating between the values from the nominal and the varied fits. The following sources of experimental uncertainty are taken into account:

- The combined 2015-2018 integrated luminosity measurement (1.7%) [142]
- Electron trigger, isolation, identification and reconstruction efficiencies
- Electron energy/momentum scale and resolution
- E_T^{miss} soft term track scale and resolution
- Jet energy scale and resolution
- JVT efficiency
- b-tagging efficiency

7.8.3 Background Modelling Uncertainty

As the background is modelled based on a fit to data, the exact model chosen may introduce a bias to the analysis. Such a bias can lead to the measurement of signal events that are not really there, a so called "spurious signal". To test for this bias, the model must be fitted to a high-statistics signal-free Monte Carlo sample. As the spurious signal could be replicated by statistical fluctuations, the equivalent

luminosity of the Monte Carlo sample used needs to be significantly larger than that of the data used in the main analysis. The invariant mass spectrum of this large sample is then fitted using the signal and background models of the analysis in order to look for any spurious signal events [143].

The largest background in this analysis is the $Z/\gamma^* \to e^+e^-$ process, so this is the process focused on in the evaluation of this systematic. Due to the large cross-section of this process, more than 10^9 events need to be generated to account for the amount of luminosity needed, more than is computationally feasible if using the full Geant4 based ATLAS simulation. In order to generate the statistics needed, a faster smearing method is used to approximate the performance of the detector.

The Monte Carlo events used are generated with a combination of POWHEG and ALPGEN [144]. POWHEG is used to generate an inclusive NLO $Z/\gamma^* \to e^+e^-$ sample of events, with 10^9 events at an invariant mass of $m_{ee} > 95$ GeV and 0.5×10^9 events in the range of $60 < m_{ee} < 95$ GeV. This split is to ease the load of production, as the higher mass range dominates the signal region even after smearing. ALPGEN is used for the generation of Z/γ^*+ jets events, which are critical for the VBF region of the analysis. For this region, 10^8 events are produced in the $m_{ee} > 95$ GeV range and 2.5×10^8 are produced in the $60 < m_{ee} < 95$ GeV range. For both signatures, the produced Monte Carlo events in the high mass range correspond to an integrated luminosity of approximately 5600 fb^{-1}.

After the Monte Carlo is generated, QED final state radiation is generated for the samples, and then the electrons and jets in the event are smeared to mimic the detector performance, and pile-up jets are overlaid on the events. The events are then reweighted so that the "sidebands" of the Monte Carlo events (events with $110 < m_{ee} < 120$ GeV or $130 < m_{ee} < 160$ GeV) match the "sidebands" of the data. This reweighting is performed in three steps. Firstly, the ratio between the data sidebands and the smeared Monte Carlo is calculated in each bin. Then, a linear fit is performed to these ratios. Finally the number of events in each bin and its uncertainty are both multiplied by the value of the fitted function, evaluated at

the centre of the bin. The smeared, reweighted Monte Carlo is then fitted to the invariant mass spectrum with the signal and background models of the search in order to evaluate the "spurious signal".

7.8.3.1 Spurious Signal fits

The fits to the high statistics Monte Carlo are shown in figure 7.8. It can be seen in all 7 categories that the background model describes the shape of the background-only distribution. The fits shown here correspond to a $H \rightarrow e^+e^-$ signal with a Higgs boson mass of $m_H = 125$ GeV. The fits were repeated for signal masses between 120-130 GeV in intervals in 1 GeV, by introducing an offset in the μ_C and μ_G fitted parameters of the signal function. For the sake of a conservative result to the overall analysis, the mass point with the largest evaluated spurious signal is used in the evaluation of the systematic in each category. The spurious signal yields used are shown in table 7.4.

A simultaneous fit across all categories to the high-statistics Monte Carlo samples, in the absence of any signal Monte Carlo events, yields a signal strength ($\mu = N_{sig}/N_{sig}^{SM}$) of

$$\mu = 0.0095 \pm 0.0673 \tag{7.3}$$

including all previously discussed systematics as well as the spurious signal systematic. This is consistent with the expected value of 0.

7.9 Final Fit

The fit used in the final step of this analysis is performed with a binned maximum likelihood method, where the likelihood is described by analytic functions. The fit is a simultaneous fit across all seven signal categories, and so the likelihood can be

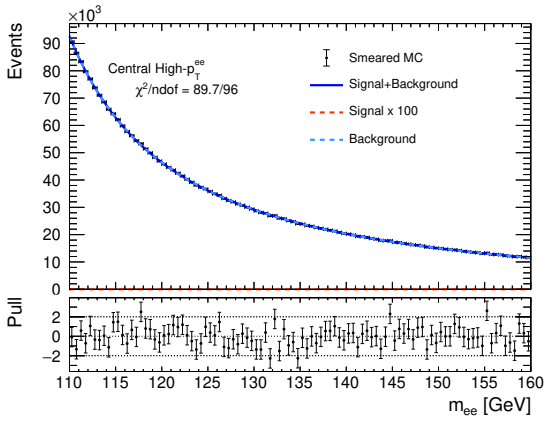

(a) Central, $p_T^{ee} > 50$ GeV

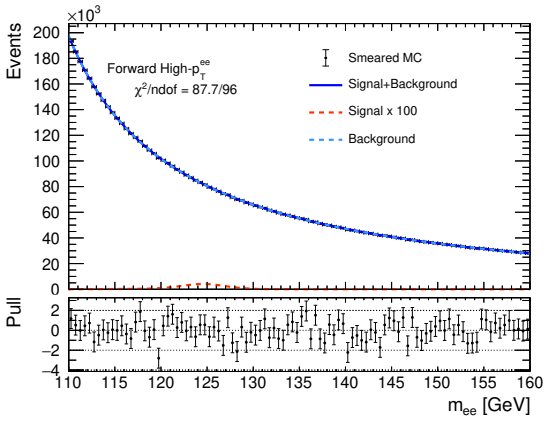

(b) Forward, $p_T^{ee} > 50$ GeV

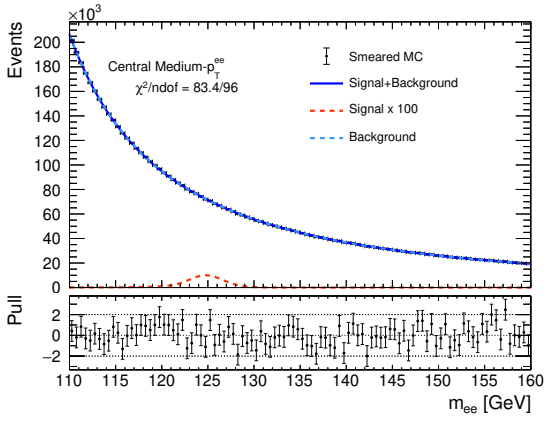

(c) Central, $15 < p_T^{ee} < 50$ GeV

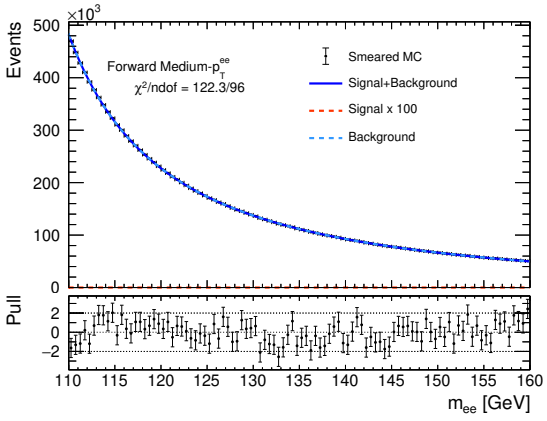

(d) Forward, $15 < p_T^{ee} < 50$ GeV

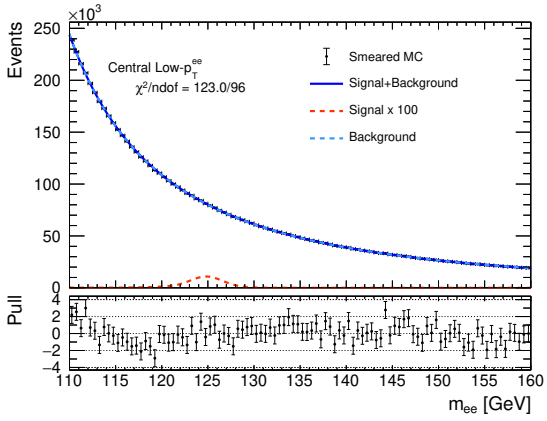

(e) Central, $p_T^{ee} < 15$ GeV

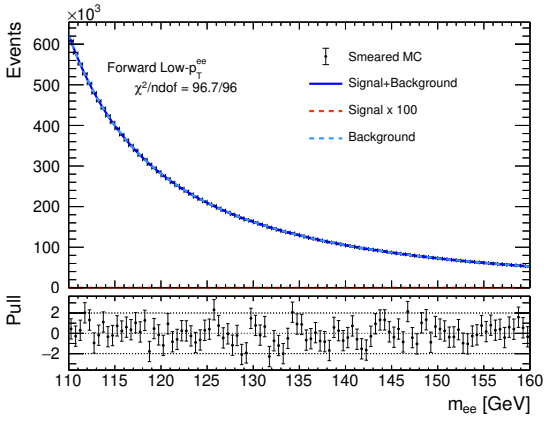

(f) Forward, $p_T^{ee} < 15$ GeV

Table 7.4: Number of spurious signal events (N_{SS}) corresponding to 140 fb^{-1} in the seven signal categories. The values shown are the max values of N_{SS} from a scan of Higgs boson masses between 120-130 GeV. These values are taken as the final uncertainty in the spurious signal error.

Category	max($\lvert N_{SS}\rvert$) in (120,130) GeV
Central, high p_T^{ee}	43
Forward, high p_T^{ee}	65
Central, medium p_T^{ee}	114
Forward, medium p_T^{ee}	220
Central, low p_T^{ee}	176
Forward, low p_T^{ee}	113
VBF	9.9

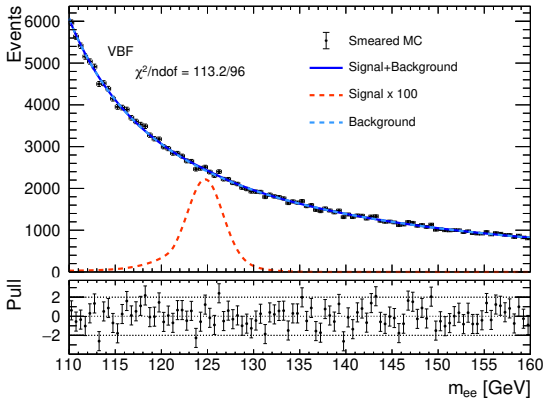

(g) VBF category

Figure 7.8: Signal plus background fits to m_{ee} distributions from fast-smeared $Z/\gamma^* \rightarrow ee$+jets sample, reweighted to the data sidebands with the full selection and categorisation applied. The samples are normalised to 5600 fb^{-1} and the fitted signal is multiplied by a factor of 100. In cases where the signal is not visible, this is due to a negative signal normalisation being fitted. Also shown are the pulls defined as the ratio of the Monte Carlo value subtracted by the model value, over the model value.

written as

$$L\left(\mu, \underline{\theta}\right) = \prod_{c=1}^{n_{\text{cat}}} L_c(\mu, \underline{\theta}) \tag{7.4}$$

where n_{cat} is the number of categories (7) and $\underline{\theta}$ are the nuisance parameters. L_c is the likelihood for category c, which can be written as a product of likelihoods for each mass bin:

$$L_c\left(\mu, \underline{\theta}\right) = \prod_{k=1}^{N_c} \mathcal{L}_c\left(m_{ee}(k); \mu, \underline{\theta}\right) \tag{7.5}$$

where N_c is the number of mass bins in category c and $\mathcal{L}_c$ is the per-category likelihood function. $\mathcal{L}_c$ is expressed in a functional form, dependent on the signal and background functions, the numbers of signal and background events, the parameter of interest μ and the various nuisance parameters:

$$\begin{aligned} \mathcal{L}_c\left(m_{ee}; \mu, \underline{\theta}\right) = \mu \cdot N_{\text{signal,c}}(\underline{\theta}^{\text{signal}}) f_{\text{signal,c}}(m_{ee}) \\ + N_{\text{spurious}}(\theta) f_{\text{signal,c}}(m_{ee}) \\ + N_{\text{bkg,c}} f_{\text{bkg,c}}(m_{ee}; \underline{\theta}^{\text{bkg}}) \end{aligned} \tag{7.6}$$

where $N_{\text{bkg,c}}$ and $N_{\text{signal,c}}$ are the number of signal and background events in category c, $f_{\text{bkg,c}}$ and $f_{\text{signal,c}}$ are the background and signal PDFs for category c, and $\underline{\theta}^{\text{bkg}}$ and $\underline{\theta}^{\text{signal}}$ are the nuisance parameters of the background and signal parameterisations. N_{spurious} is the nuisance parameter associated with the spurious signal. This likelihood fit is used to evaluate a limit on the signal strength parameter μ.

7.9.1 Limit Setting

The final result of this analysis is an upper limit on the signal strength parameter μ, defined as the ratio of the number of measured signal events over the expected number of signal events under the assumptions of the Standard Model. For the

purposes of calculating this limit, a test statistic $\tilde{q}_\mu$ is constructed:

$$\tilde{q}_\mu = \begin{cases} -2\ln\frac{L(\mu,\hat{\hat{\theta}}(\mu))}{L(0,\hat{\hat{\theta}}(0))} & \hat{\mu} < 0 \\ -2\ln\frac{L(\mu,\hat{\hat{\theta}}(\mu))}{L(\hat{\mu},\hat{\theta})} & 0 \leq \hat{\mu} \leq \mu \\ 0 & \hat{\mu} > \mu \end{cases} \tag{7.7}$$

where L is the likelihood as described in the previous section, $\hat{\mu}$ and $\hat{\theta}$ are the best fit values of θ and μ with all other parameters left floating, and $\hat{\hat{\theta}}(\mu)$ is the best fit value of θ for a fixed value of μ. This test statistic uses the ratio between the likelihood for a fixed value of μ and the likelihood for the best-fit value of μ to estimate the compatibility between each μ hypothesis and the data.

The limits are calculated using a modified frequentist (CL_s) method [145]. The CL_s exclusion is calculated as

$$CL_s(\mu) = \frac{p_\mu}{1 - p_b} \tag{7.8}$$

where p_μ is the p-value of the signal+background hypothesis and p_b is the p-value of the background only hypothesis. p_μ and p_b can be calculated as:

$$p_\mu = \int_{\tilde{q}_\mu^{obs}}^{\infty} f\left(\tilde{q}_\mu|\mu, \hat{\theta}_\mu^{obs}\right) d\tilde{q}_\mu, \tag{7.9}$$

$$1 - p_b = \int_{\tilde{q}_0^{obs}}^{\infty} f\left(\tilde{q}_\mu|0, \hat{\theta}_0^{obs}\right) d\tilde{q}_\mu, \tag{7.10}$$

where $\hat{\theta}_\mu^{obs}$ and $\hat{\theta}_0^{obs}$ are the fitted nuisance parameters, and $f\left(\tilde{q}_\mu|\mu, \hat{\theta}_\mu^{obs}\right)$ and $f\left(\tilde{q}_\mu|0, \hat{\theta}_0^{obs}\right)$ are sampling functions [146]. Limits are then set at the 95% confidence level by scanning values of the parameter of interest μ, calculating the CL_s value for each μ hypothesis, and identifying the value of μ for which the value of CL_s is equal to 0.05.

The following chapter summarises the results of the analysis, including the expected signal and background yields in each category, the results of the fits used to model

the signal and background, and the final upper limits set on the $H \to e^+e^-$ branching fraction.

Chapter 8

A Search for the di-electron Decay Mode of the Higgs Boson - Results

This chapter summarises the main results of the analysis described in chapter 7. Firstly, the results of the event selection are shown, including the signal and background yields across the seven signal categories. Then, the results of the signal and background modeling are shown, showing the fitted analytical models against the signal Monte Carlo and the data respectively. Finally, the results of the final fit and limit setting procedure are shown.

8.1 Event Yields

Table 8.1 shows the expected signal and background yields in each of the seven signal categories. These yields are extracted from the signal and background models in each category, defined as the integral of the respective model within the mass range of $120 < m_{ee} < 130$ GeV. For the purpose of these expected yield calculations, the signal models are scaled to an equivalent expected branching fraction of 0.1%. In general, higher $\frac{S}{B}$ ratios can be seen in the central and higher p_T categories, and this ratio is highest in the VBF category, which is expected due to the lower cross

Table 8.1: Expected signal and background yields in each category for $120 < m_{ee} < 130$ GeV and a signal branching fraction of 0.1%

Category	S	B	$\frac{S}{B}$	Data
VBF	123 ± 11	2528 ± 52	0.0487 ± 0.0045	2561 ± 52
Central, low p_T^{ee}	225 ± 15	39190 ± 190	0.00575 ± 0.00038	39870 ± 190
Forward, low p_T^{ee}	387 ± 19	98450 ± 300	0.00393 ± 0.00019	100840 ± 320
Central, medium p_T^{ee}	424 ± 22	30750 ± 170	0.01379 ± 0.00071	31180 ± 170
Forward, medium p_T^{ee}	708 ± 26	74850 ± 270	0.00945 ± 0.00035	76480 ± 270
Central, high p_T^{ee}	380 ± 19	13440 ± 120	0.0283 ± 0.0014	13630 ± 120
Forward, high p_T^{ee}	591 ± 24	29890 ± 170	0.01978 ± 0.00081	3016 ± 170

section of Z events producing two jets. Also shown are the yields of data events in the same mass range for the seven categories. The actual event yields are consistent with the number of expected events from the background model.

8.2 Background and Signal Modeling

The fits of the background model described in section 7.7 to data events, are shown in figure 8.1. As can be seen in the figures, the fits have χ^2 values of between 0.7 and 1.2, and so the model describes the data well. The fitted values of the background model parameters B and f are shown in table 8.2. Although the value of the exponential parameter B is positive in some categories, the overall shape of the background still resembles a falling slope due to the $1/m^3$ term in the model.

As an extra check on the fitted background model, histograms of the pulls from the data fits are shown in figure 8.2. The pull is defined as the fitted value for each bin of the data fit, subtracted from the actual number of data entries in that bin, all divided by the fitted value. The pull histograms are then fitted with a simple Gaussian function. For a good fit, the values of the mean and of σ for this Gaussian are expected to be 0 and 1 respectively. As can be seen in the plots, all of the fits show parameters within one or two standard deviations of this expectation, and they all have χ^2 values between 1 and 3 per degree of freedom, and so they show

Table 8.2: The background function fit parameters, as defined in equation 7.2, in each signal category as obtained from the blinded background-only fit to data.

Category	B/GeV^{-1}	f
VBF	0.0033 ± 0.0035	0.400 ± 0.049
Central, low p_T^{ee}	-0.0273 ± 0.0013	0.220 ± 0.022
Forward, low p_T^{ee}	-0.01748 ± 0.00084	0.274 ± 0.012
Central, medium p_T^{ee}	-0.0119 ± 0.0015	0.267 ± 0.019
Forward, medium p_T^{ee}	-0.00937 ± 0.00075	0.374 ± 0.011
Central, high p_T^{ee}	-0.0032 ± 0.0017	0.408 ± 0.025
Forward, high p_T^{ee}	0.00106 ± 0.00097	0.460 ± 0.014

agreement with this expectation.

8.3 Final Results

The final fit, performed as described in section 7.9, finds no significant excess of events over the expected background. The measured branching fraction from the fit is $\mathcal{B}(H \to e^+e^-) = (0.0 \pm 1.8) \times 10^{-4}$. Figure 8.3 shows the impact of the various systematic uncertainties on the fit. The plot is ordered by the size of the systematics' impact on the final result, so it can be seen that the most important uncertainties are the background modelling uncertainties (labelled ATLAS_bias), followed closely by the electron resolution.

An additional fit is performed using separate parameters of interest for the signal strength in each of the signal categories, leading to an extra six parameters in the overall fit. The compatibility p-value between this fit and the single parameter of interest fit is calculated by taking twice the difference between the fitted value of each channel and the overall fitted value and calculating a χ^2 probability. The results of the fit, along with this p-value, are shown in figure 8.4. It can be seen that the multiple POI fit is compatible with the single POI fit.

The CL_s scan, performed as described in section 7.9.1, is shown in figure 8.5. The

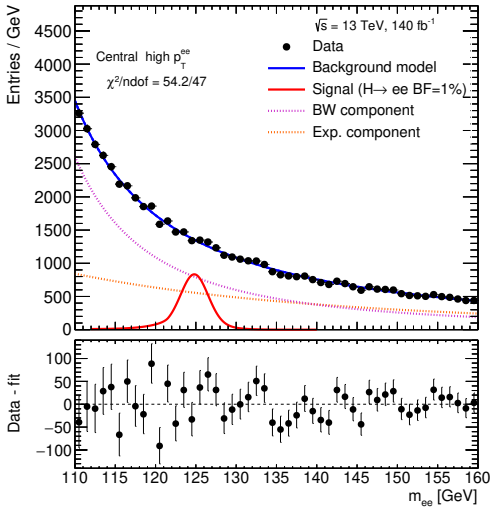

(a) Central, $p_T^{ee} > 50$ GeV

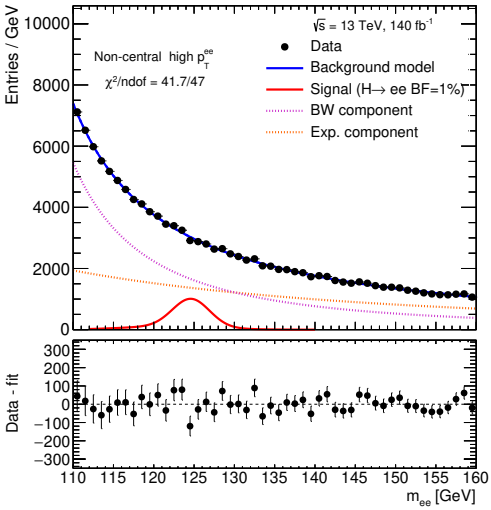

(b) Forward, $p_T^{ee} > 50$ GeV

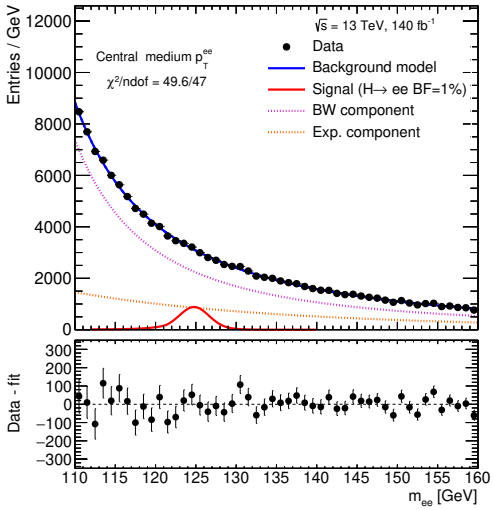

(c) Central, $15 < p_T^{ee} < 50$ GeV

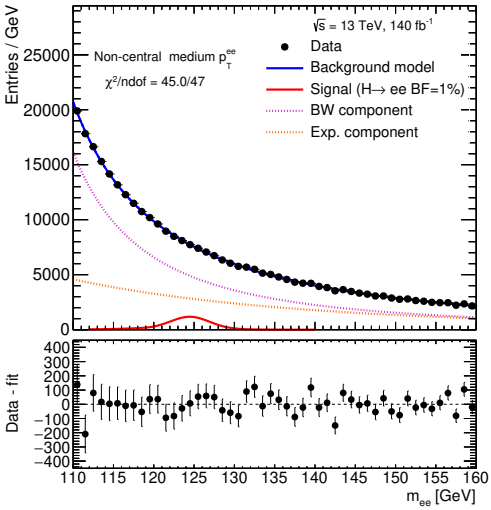

(d) Forward, $15 < p_T^{ee} < 50$ GeV

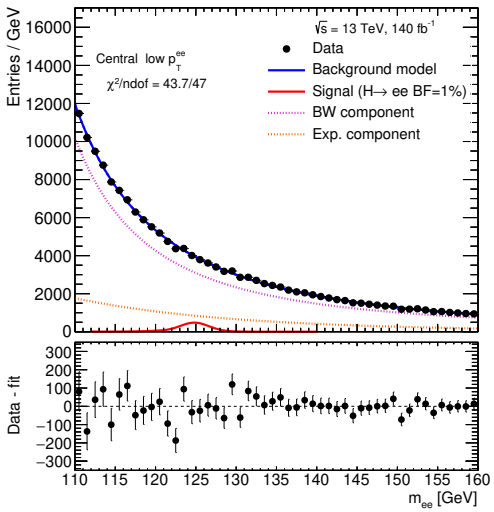

(e) Central, $p_T^{ee} < 15$ GeV

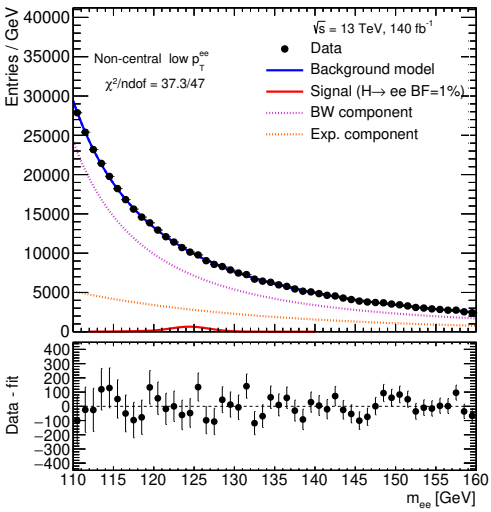

(f) Forward, $p_T^{ee} < 15$ GeV

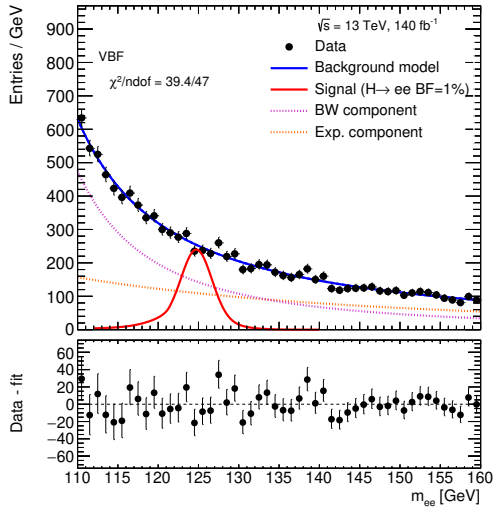

(g) VBF category

Figure 8.1: Invariant mass distributions of the data events fitted with the background model PDF in the different signal categories. The Drell-Yan (pink) and exponential (yellow) components are shown in addition to the full combined background model (blue). The invariant mass range of $120 < m_{ee} < 130$ GeV is excluded from the fit.

Table 8.3: Observed and expected 95% CL_S upper limits on the branching fraction $\mathcal{B}(H \to e^+e^-)$, along with the uncertainties on the expected limit.

Mass [GeV]	Observed	Expected	$+2\sigma$	$+1\sigma$	-1σ	-2σ
125	3.6×10^{-4}	3.5×10^{-4}	6.7×10^{-4}	4.9×10^{-4}	2.6×10^{-4}	1.9×10^{-4}

expected and observed limits are shown in the plot as the points where the CL_s value is equal to 0.05 (marked by the horizontal dashed line). A 95% CL_S upper limit of 3.6×10^{-4} is set on the $H \to e^+e^-$ branching ratio. This result, along with the expected limit and its uncertainties, is also shown in table 8.3.

8.4 Conclusion

The result shown here is a considerable improvement over the previous upper limit of 0.0019, [97], based on 19.7 fb^{-1} of data at $\sqrt{s} = 8$ TeV. This improvement can be

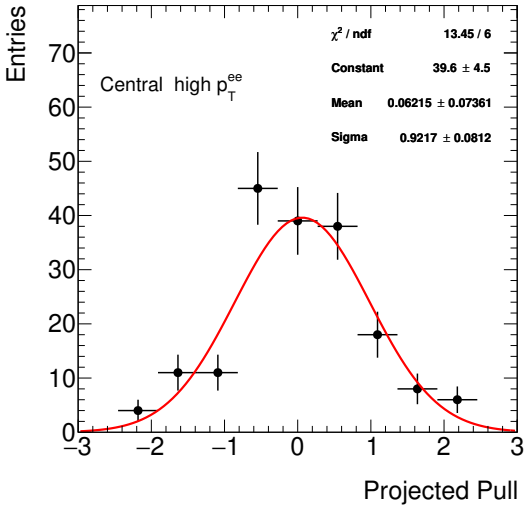

(a) Central, $p_T^{ee} > 50$ GeV

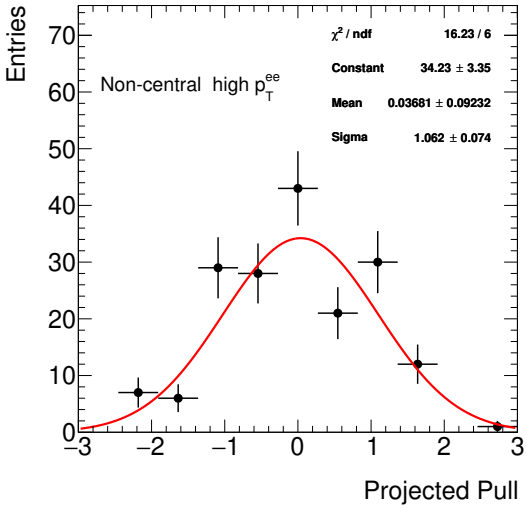

(b) Forward, $p_T^{ee} > 50$ GeV

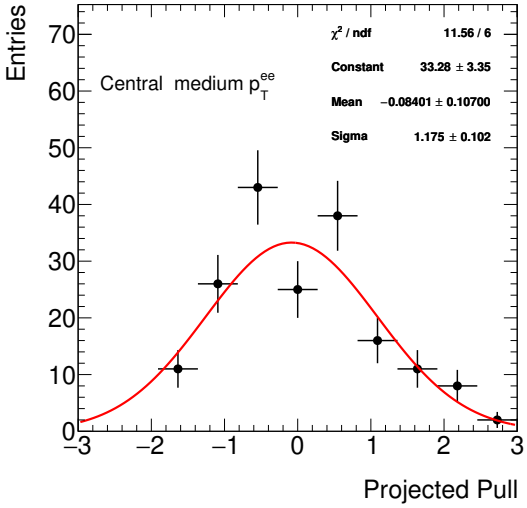

(c) Central, $15 < p_T^{ee} < 50$ GeV

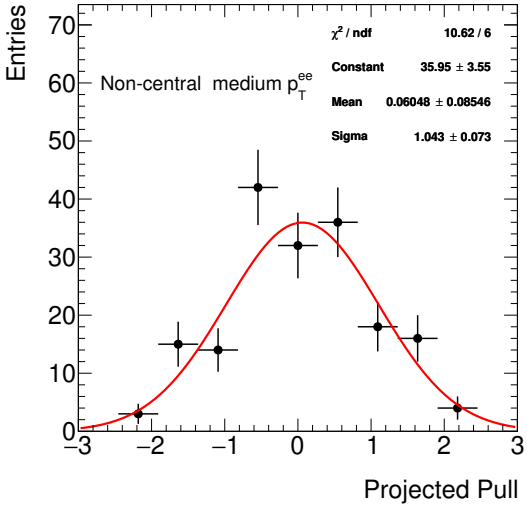

(d) Forward, $15 < p_T^{ee} < 50$ GeV

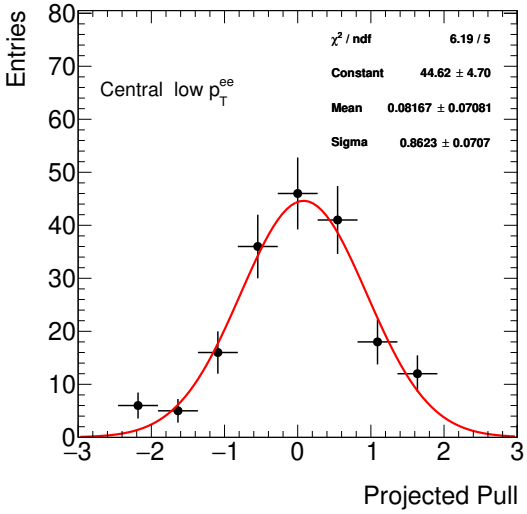

(e) Central, $p_T^{ee} < 15$ GeV

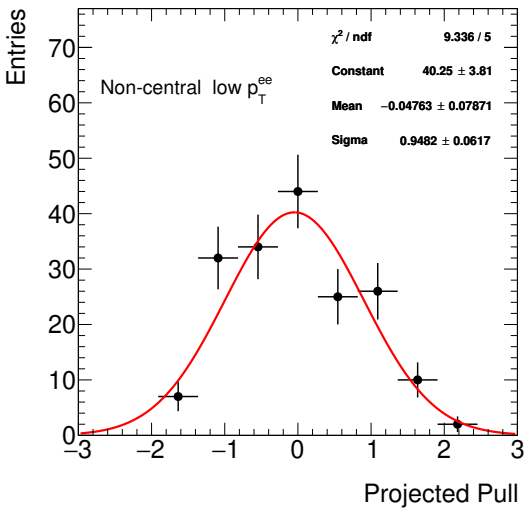

(f) Forward, $p_T^{ee} < 15$ GeV

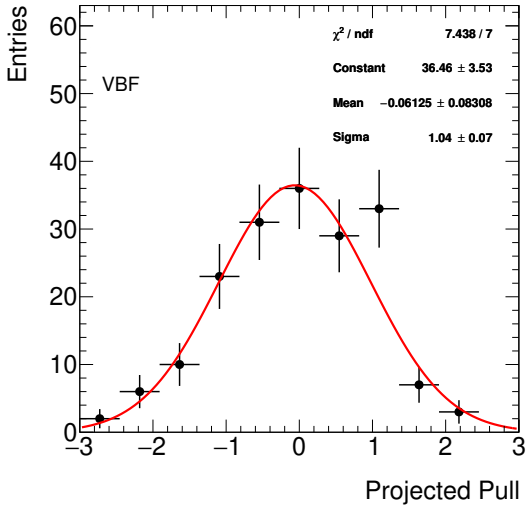

(g) VBF category

Figure 8.2: Pull histograms from fits of the background model to data in each signal category. A simple Gaussian fit to the pulls is also shown.

largely attributed to the approximately factor 7 increase in luminosity, in addition to the increase in the Higgs boson production cross section when increasing the centre of mass energy to 13 TeV. More minor differences in the overall result may arise from differences in the selection and differences in detector performance between the two analyses.

The upper limit of 3.6×10^{-4} on the branching ratio $\mathcal{B}(H \to e^+e^-)$ represents an upper limit of 7.2×10^4 times the expected Standard Model value of 5×10^{-9}. This complements the existing limit of 2.1 times the Standard Model value of 2.2×10^{-4} for the branching ratio $\mathcal{B}(H \to \mu^+\mu^-)$ [116], although at a much higher ratio due to the low expectation for $H \to e^+e^-$. Overall the observed limit of 3.8×10^{-4} on the $H \to \mu\mu$ branching ratio is similar to the observed limit on $H \to ee$ presented here, which is to be expected considering the similarities between the two analyses. Along with the existing searches for $H \to \tau^+\tau^-$ [100], and the lepton flavour violating decays [117], there are now a complete set of $H \to ll$ analyses and results from the ATLAS experiment, and these can continue to be iterated and improved upon in future runs of the LHC.

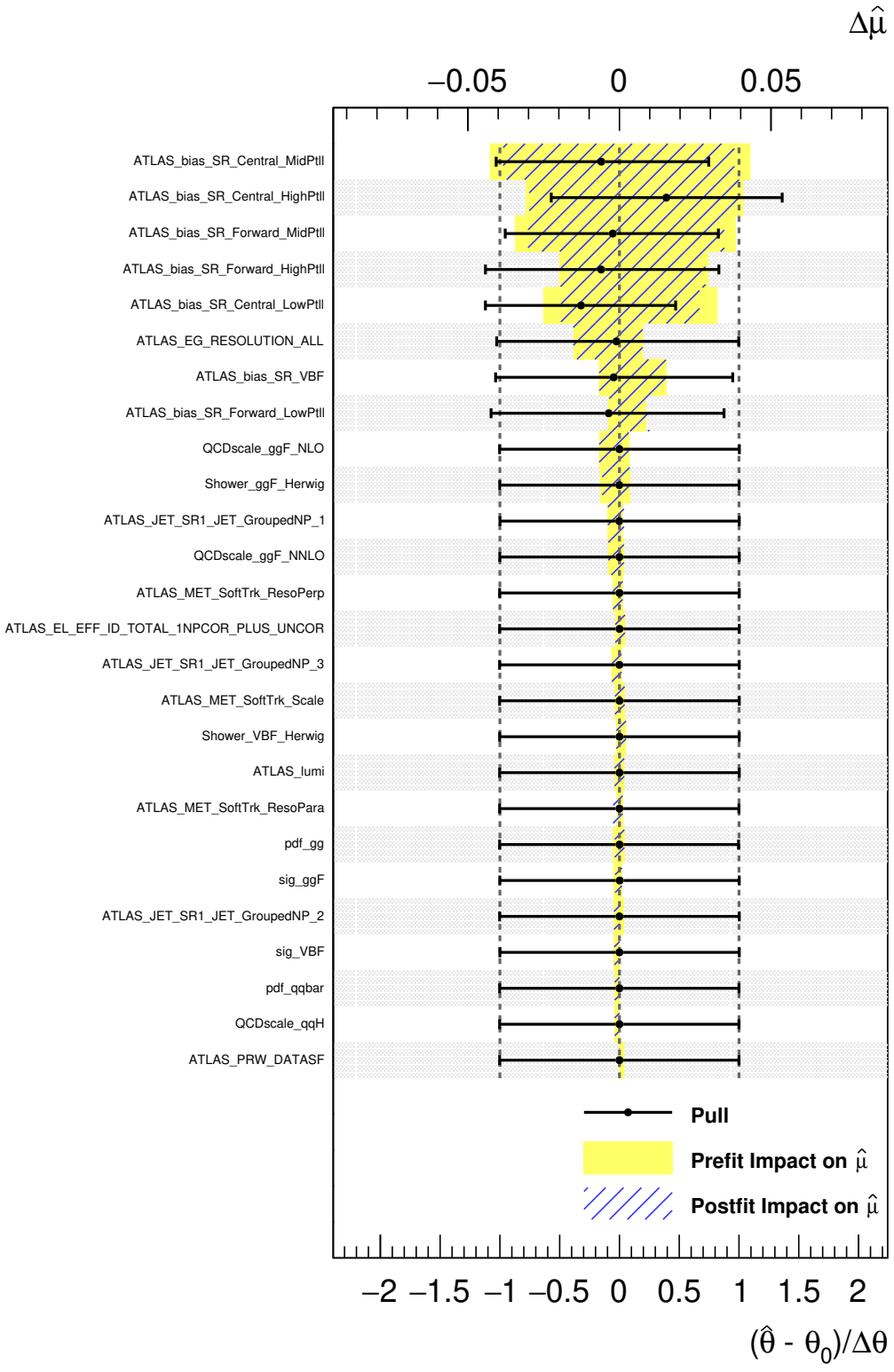

Figure 8.3: The impacts of the systematic uncertainties on the measured signal strength, and the pulls on the values of the systematics in the final fit

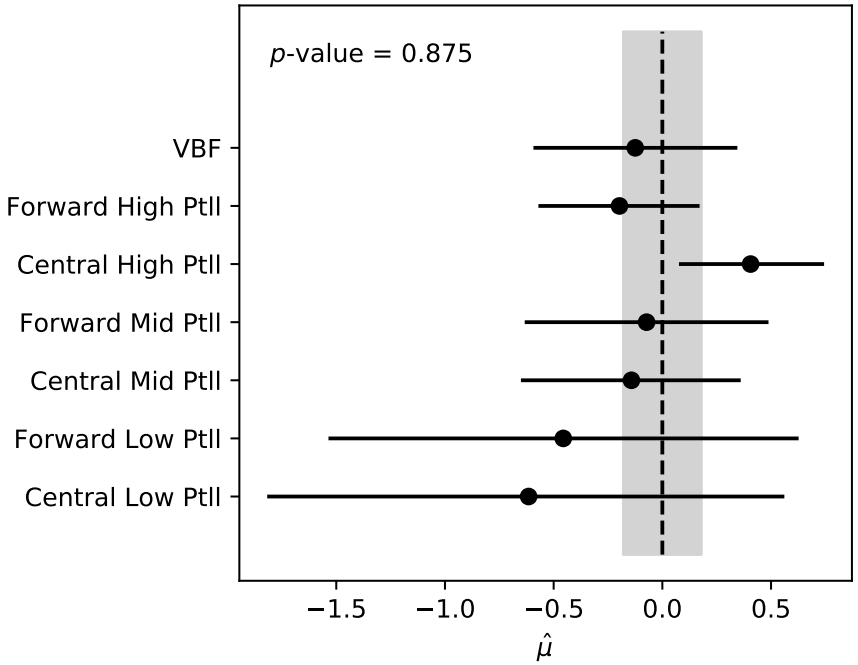

Figure 8.4: Fitted values of the signal strength when each channel is fitted with uncorrelated signal strengths. The fitted value of the signal strength in the correlated fit is shown by the dashed line. The compatibility between the two fits is expressed by the p-value

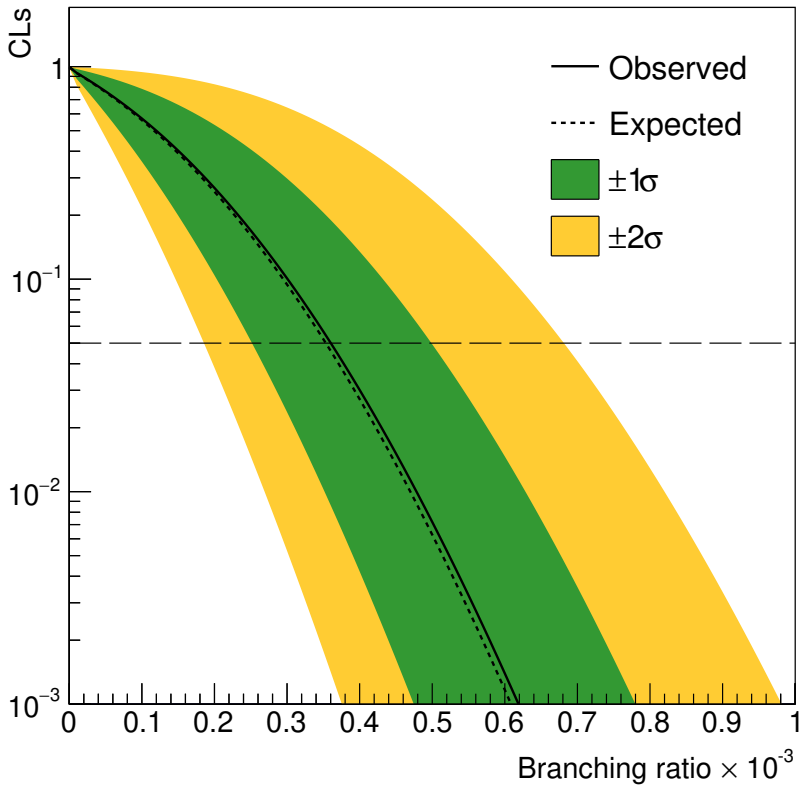

Figure 8.5: CL_s scan of the branching ratio $\mathcal{B}(H \to e^+e^-)$. The dashed line represents the CL_s value of 0.05. The solid and dotted lines represent the upper observed and expected limits respectively, while the coloured bands represent the uncertainties on the expected limit.

The limit calculated here, while showing how far away we are from a measurement of the Standard Model $H \to e^+e^-$ decay at the LHC, still supports the hypothesis that the discovered Higgs boson is a Standard Model Higgs boson, as under Standard Model predictions the decay is beyond the reach of the LHC. Further study of this decay at the LHC could more strongly support the Standard Model hypothesis if it is not discovered, or provide evidence of a non-standard Higgs sector if it is. As the main limitation of the analysis is the amount of statistics available, rather than the size of any of the systematic uncertainties, future analyses of this decay will most likely be driven by the accumulation of larger datasets from the HL-LHC and beyond, rather than any improvement in analysis technique.

Chapter 9

Conclusion

The LHC programme at CERN has been and continues to be a resounding success. Across seven experiments, each consisting of hundreds of collaboration members, each year of LHC running has brought substantial observations and measurements and, as we are approximately halfway through the proposed lifecycle of the machine, this progress is set to continue for years to come. This is evident within the field of Higgs boson physics, in which a particle first discovered in 2012 now has a large array of measurements associated with it, with many more searches ongoing. The work presented in previous chapters represents just a small amount of the work undertook by ATLAS, as well as some plans for the future.

The Phase-I upgrade of the ATLAS detector is set to prepare the experiment for higher data rates and radiation levels, as well as improve performance of the sub-detectors and triggers. In order for these upgraded systems to run smoothly, problems need to be identified quickly and accurately by non-experts in the ATLAS control room. The detector control system project presented is designed to allow this for components of the level one calorimeter trigger. This system forms part of a larger detector control system, both in combination with the other FEX units and other L1Calo components, and on a wider level with the detector control systems of all the sub-detectors and systems within ATLAS.

The discovery of the Higgs boson was a confirmation of the existence of the Higgs field, considered to be the final puzzle piece of the Standard Model of particle physics. With this complete model, future developments can broadly take two forms. The first is to test the predictions of the Standard Model, for example the predicted coupling of the Higgs boson to the mass of the fermions and the squared mass of the vector bosons. The other is in searches for new physics phenomena outside of the Standard Model, as there are many aspects of the universe that the Standard Model does not describe. These two approaches can complement each other, for example there are many theories for the nature of the Higgs field beyond that of the Standard Model, and non-standard measurements of Higgs couplings may indicate towards one of these models.

The two analyses presented are related to measurements of the Higgs boson coupling to fermions. As they are focused towards lower-generation fermions than those already observed couplings to the Higgs, measurements could provide strong further evidence for the couplings' dependence on mass, if no deviation is seen from the linear dependence predicted by the Standard Model. The first analysis presented was based around the Higgs boson coupling to muons, and the prospect of measuring this coupling at ATLAS using future data from the HL-LHC. It is found that we should expect to measure this decay at the HL-LHC with a significance of 9.6σ, and with a relative uncertainty on the branching ratio of 13%. These strong expectations of precision and statistical significance show the potential of the HL-LHC in the Higgs sector, as measuring these results, or large deviations from these expectations, could further confirm or deny the current understanding of the nature of the Higgs.

The final analysis presented relates to the coupling between the Higgs boson and electrons, via the $H \to e^+e^-$ decay. No observation of the decay is made, and an upper limit of 3.6×10^{-4} is set on its branching ratio, similar to the expected limit of 3.5×10^{-4}. The agreement between the expected and observed result provides no indication that the Higgs boson does not behave as we expect, however as the expected branching ratio is several orders of magnitude smaller than the observed limit, the impact of this result on theoretical predictions is not a large one. Nev-

ertheless, the limits set are useful in putting constraints on theories beyond the Standard Model, and would stand to be improved through future analysis of data from Run-III and the HL-LHC.

The possible successes of the HL-LHC and Run-II go beyond the analyses presented here. The HL-LHC in particular is designed with the purpose of measuring di-Higgs production in mind. There are also many avenues to be explored outside of the Higgs sector, from precision measurements of the top quark to searches for beyond the Standard Model phenomena such as supersymmetry or dark matter. However, within the realm of leptonic couplings of the Higgs boson, the expected increases in available data, along with the ever-present possibilities of refinement to the analysis process, make the prospects for these measurements in the future very promising. This is particularly true for the $H \to \mu^+\mu^-$ decay, for which a measurement is expected, but for the $H \to e^+e^-$ decay, improvements to the limits shown in this thesis should also be expected.

REFERENCES

[1] G. Aad *et al.*, "Search for the Higgs boson decays $H \to ee$ and $H \to e\mu$ in pp collisions at $\sqrt{s} = 13$ TeV with the ATLAS detector," *Phys. Lett.*, vol. B801, p. 135148, 2020.

[2] R. Aaij *et al.*, "Observation of $J/\psi p$ Resonances Consistent with Pentaquark States in $\Lambda_b^0 \to J/\psi K^- p$ Decays," *Phys. Rev. Lett.*, vol. 115, p. 072001, 2015.

[3] G. Aad *et al.*, "Observation of a new particle in the search for the Standard Model Higgs boson with the ATLAS detector at the LHC," *Phys. Lett.*, vol. B716, pp. 1–29, 2012.

[4] S. Chatrchyan *et al.*, "Observation of a new boson at a mass of 125 GeV with the CMS experiment at the LHC," *Phys. Lett.*, vol. B716, pp. 30–61, 2012.

[5] R. Assmann, M. Lamont, and S. Myers, "A brief history of the LEP collider," *Nucl. Phys. Proc. Suppl.*, vol. 109B, pp. 17–31, 2002.

[6] D. Cundy and S. Gilardoni, "The Proton Synchrotron (PS): At the Core of the CERN Accelerators: Introduction," *Adv. Ser. Direct. High Energy Phys.*, vol. 27, pp. 39–56, 2017.

[7] "The Super Proton Synchrotron." `https://cds.cern.ch/record/1997188`, Jan 2012.

[8] L. Evans and P. Bryant, "LHC machine," *Journal of Instrumentation*, vol. 3, pp. S08001–S08001, Aug 2008.

[9] M. Stockton, "The ATLAS Level-1 Central Trigger," Tech. Rep. ATL-DAQ-PROC-2011-006, CERN, Geneva, Jan 2011.

[10] T. Nayak and B. Sinha, "Search and study of Quark Gluon Plasma at the CERN-LHC," in *Physics at the Large Hadron Collider* (A. Datta, B. Mukhopadhyaya, A. Raychaudhuri, A. K. Gupta, C. L. Khetrapal, T. Padmanabhan, and M. Vijayan, eds.), pp. 131–144, 2009.

[11] ATLAS Collaboration, "ATLAS Public Results." https://twiki.cern.ch/twiki/bin/view/AtlasPublic/LuminosityPublicResultsRun2. Accessed: 2019-11-20.

[12] G. Apollinari, O. Brüning, T. Nakamoto, and L. Rossi, "High Luminosity Large Hadron Collider HL-LHC," *CERN Yellow Report*, no. 5, pp. 1–19, 2015.

[13] G. Apollinari, A. I. Béjar, O. Brüning, P. Fessia, M. Lamont, L. Rossi, and L. Tavian, *High-Luminosity Large Hadron Collider (HL-LHC): Technical Design Report V. 0.1.* CERN Yellow Reports: Monographs, Geneva: CERN, 2017.

[14] The ATLAS Collaboration, "The ATLAS Experiment at the CERN Large Hadron Collider," *Journal of Instrumentation*, vol. 3, no. 08, p. S08003, 2008.

[15] J. Pequenao, "Computer generated image of the ATLAS inner detector," Mar 2008.

[16] G. Aad *et al.*, "Expected Performance of the ATLAS Experiment - Detector, Trigger and Physics," 2009.

[17] A. La Rosa, "The ATLAS Insertable B-Layer: from construction to operation," *JINST*, vol. 11, no. 12, p. C12036, 2016.

[18] M. Aaboud *et al.*, "Performance of the ATLAS Track Reconstruction Algorithms in Dense Environments in LHC Run 2," *Eur. Phys. J.*, vol. C77, no. 10, p. 673, 2017.

[19] T. Cornelissen, M. Elsing, I. Gavrilenko, W. Liebig, E. Moyse, and A. Salzburger, "The new ATLAS track reconstruction (NEWT)," *Journal of Physics: Conference Series*, vol. 119, p. 032014, Jul 2008.

[20] *ATLAS inner detector: Technical Design Report, 1.* Technical Design Report ATLAS, Geneva: CERN, 1997.

[21] ATLAS Collaboration, "Impact parameter resolution." https://atlas.web.cern.ch/Atlas/GROUPS/PHYSICS/PLOTS/IDTR-2015-007/. Accessed: 2020-03-01.

[22] J. Pequenao, "Computer Generated image of the ATLAS calorimeter." Mar 2008.

[23] M. Aaboud *et al.*, "Measurement of the photon identification efficiencies with the ATLAS detector using LHC Run-1 data," *Eur. Phys. J.*, vol. C76, no. 12, p. 666, 2016.

[24] M. Aaboud *et al.*, "Electron reconstruction and identification in the ATLAS experiment using the 2015 and 2016 LHC proton-proton collision data at $\sqrt{s}$ = 13 TeV," *Eur. Phys. J.*, vol. C79, no. 8, p. 639, 2019.

[25] M. Cacciari, G. P. Salam, and G. Soyez, "The anti-k_t jet clustering algorithm," *JHEP*, vol. 04, p. 063, 2008.

[26] G. Cattani, "The Resistive Plate Chambers of the ATLAS experiment: performance studies," *Journal of Physics: Conference Series*, vol. 280, p. 012001, Feb 2011.

[27] G. Aad *et al.*, "Commissioning of the ATLAS Muon Spectrometer with cosmic rays," *Eur. Phys. J.*, vol. C70, pp. 875–916, 2010.

[28] G. Aad *et al.*, "Muon reconstruction performance of the ATLAS detector in proton–proton collision data at $\sqrt{s}$ =13 TeV," *Eur. Phys. J.*, vol. C76, no. 5, p. 292, 2016.

[29] L. Marchese, "Muon reconstruction performance of the ATLAS detector in 2016," *EPJ Web Conf.*, vol. 182, p. 03008, 2018.

[30] A. R. Martínez, "The Run-2 ATLAS Trigger System," *Journal of Physics: Conference Series*, vol. 762, p. 012003, Oct 2016.

[31] J. Butterworth *et al.*, "PDF4LHC recommendations for LHC Run II," *J. Phys.*, vol. G43, p. 023001, 2016.

[32] S. Dulat, T.-J. Hou, J. Gao, M. Guzzi, J. Huston, P. Nadolsky, J. Pumplin, C. Schmidt, D. Stump, and C. Yuan, "New parton distribution functions from a global analysis of quantum chromodynamics," *Phys. Rev. D*, vol. 93, no. 3, p. 033006, 2016.

[33] L. Harland-Lang, A. Martin, P. Motylinski, and R. Thorne, "Parton distributions in the LHC era: MMHT 2014 PDFs," *Eur. Phys. J. C*, vol. 75, no. 5, p. 204, 2015.

[34] "Multi-Boson Simulation for 13 TeV ATLAS Analyses," Tech. Rep. ATL-PHYS-PUB-2017-005, CERN, Geneva, May 2017.

[35] *HERA - A Proposal for a Large Electron Proton Colliding Beam Facility at DESY*. 1981.

[36] S. Agostinelli *et al.*, "Geant4 – a simulation toolkit," *Nuclear Instruments and Methods in Physics Research Section A: Accelerators, Spectrometers, Detectors and Associated Equipment*, vol. 506, no. 3, pp. 250 – 303, 2003.

[37] J. Allison *et al.*, "Geant4 developments and applications," *IEEE Trans. Nucl. Sci.*, vol. 53, p. 270, 2006.

[38] W. Lukas, "Fast simulation for ATLAS: Atlfast-II and ISF," *Journal of Physics: Conference Series*, vol. 396, p. 022031, Dec 2012.

[39] G. Aad *et al.*, "Technical Design Report for the Phase-I Upgrade of the ATLAS TDAQ System," Tech. Rep. CERN-LHCC-2013-018. ATLAS-TDR-023, Sep 2013. Final version presented to December 2013 LHCC.

[40] R. Schwienhorst, "The Phase-1 upgrade of the ATLAS first level calorimeter trigger," *Journal of Instrumentation*, vol. 11, pp. C01018–C01018, Jan 2016.

[41] PCI Industrial Computer Manufacturers Group, "AdvancedTCA." `https://www.picmg.org/openstandards/advancedtca/`. Accessed: 2020-02-14.

[42] WIENER Company, "Powered VME Crates." `http://www.wiener-d.com/sc/powered-crates/vme/`. Accessed: 2020-03-15.

[43] ATLAS Collaboration, "Letter of Intent for the Phase-II Upgrade of the ATLAS Experiment," Tech. Rep. CERN-LHCC-2012-022. LHCC-I-023, CERN, Geneva, Dec 2012.

[44] A. Collaboration, "Technical Design Report for the ATLAS Inner Tracker Pixel Detector," Tech. Rep. CERN-LHCC-2017-021. ATLAS-TDR-030, CERN, Geneva, Sep 2017.

[45] A. Collaboration, "Technical Design Report for the ATLAS Inner Tracker Strip Detector," Tech. Rep. CERN-LHCC-2017-005. ATLAS-TDR-025, CERN, Geneva, Apr 2017.

[46] "Expected Tracking Performance of the ATLAS Inner Tracker at the HL-LHC," Tech. Rep. ATL-PHYS-PUB-2019-014, CERN, Geneva, Mar 2019.

[47] A. Barriuso Poy *et al.*, "The detector control system of the ATLAS experiment," *JINST*, vol. 3, p. P05006, 2008.

[48] O. Beltramello, H. J. Burckhart, S. Franz, M. Jaekel, M. Jeckel, S. Lüders, G. Morpurgo, F. dos Santos Pedrosa, K. Pommes, and H. Sandaker, "The detector safety system of the ATLAS experiment," *Journal of Instrumentation*, vol. 4, pp. P09012–P09012, Sep 2009.

[49] "Simatic wincc open architecture." `https://new.siemens.com/global/en/products/automation/industry-software/automation-software/scada/simatic-wincc-oa.html`. Accessed: 2019-10-14.

[50] C. Gaspar, R. Jacobsson, B. Jost, S. Morlini, N. Neufeld, P. Vannerem, and B. Franek, "An integrated experiment control system, architecture, and benefits: the LHCb approach," *IEEE Trans. Nucl. Sci.*, vol. 51, pp. 513–520, 2004.

[51] O. Holme, M. González-Berges, P. Golonka, and S. Schmeling, "The JCOP Framework," Tech. Rep. CERN-OPEN-2005-027, CERN, Geneva, Sep 2005.

[52] C. Gaspar and B. Franek, "Tools for the automation of large distributed control systems," *IEEE Trans. Nucl. Sci.*, vol. 53, pp. 974–979, 2006.

[53] F. Viegas, R. Hawkings, and G. Dimitrov, "Relational databases for conditions data and event selection in ATLAS," *J. Phys. Conf. Ser.*, vol. 119, p. 042032, 2008.

[54] OpenLDAP Foundation, "OpenLDAP — community developed LDAP software." http://www.openldap.org. Accessed: 2019-10-29.

[55] Intel, "Intelligent Platform Management Interface Specification - Second Generation." https://www.intel.com/content/www/us/en/products/docs/servers/ipmi/ipmi-second-gen-interface-spec-v2-rev1-1.html. Accessed: 2020-02-14.

[56] T. S. Williams, "IPbus A flexible Ethernet-based control system for xTCA hardware," Tech. Rep. CMS-CR-2014-334, CERN, Geneva, Oct 2014.

[57] R. Larsen and /SLAC, "Atca for machines– advanced telecommunications computing architecture," *Proceedings of LCWS/ILC 2007*, 4 2008.

[58] A. P. Rodrigues, B. Santos, P. F. Carvalho, M. Correia, J. Sousa, C. M. Correia, and B. Gonçalves, "Taking advantage of the intercommunication features of ipmcs in atca cdaq systems," *Fusion Engineering and Design*, vol. 128, pp. 138 – 142, 2018.

[59] CERN, "CERN IPMC." https://cern-ipmc.web.cern.ch/. Accessed: 2020-02-14.

[60] NXP Semiconductors, "I^2C-bus specification and user manual." https://www.nxp.com/docs/en/user-guide/UM10204.pdf. Accessed: 2020-03-17.

[61] S. Schlenker, D. Abalo Miron, B. Farnham, V. Filimonov, P. Nikiel, and C.-V. Soare, "quasar - A Generic Framework for Rapid Development of OPC UA Servers," p. WEB3O02. 4 p, 2015.

[62] P. P. Nikiel, B. Farnham, V. Filimonov, and S. Schlenker, "Generic OPC UA server framework," *Journal of Physics: Conference Series*, vol. 664, p. 082039, dec 2015.

[63] P. P. Nikiel, "Cacophony generates wincc oa bindings for quasar-based opc-ua servers." https://github.com/quasar-team/cacophony.

[64] P. W. Higgs, "Broken symmetries and the masses of gauge bosons," *Phys. Rev. Lett.*, vol. 13, pp. 508–509, Oct 1964.

[65] F. Englert and R. Brout, "Broken symmetry and the mass of gauge vector mesons," *Phys. Rev. Lett.*, vol. 13, pp. 321–323, Aug 1964.

[66] G. S. Guralnik, C. R. Hagen, and T. W. B. Kibble, "Global conservation laws and massless particles," *Phys. Rev. Lett.*, vol. 13, pp. 585–587, Nov 1964.

[67] A. S. Kronfeld and C. Quigg, "Resource Letter: Quantum Chromodynamics," *Am. J. Phys.*, vol. 78, pp. 1081–1116, 2010.

[68] D. J. Gross and F. Wilczek, "Asymptotically free gauge theories. i," *Phys. Rev. D*, vol. 8, pp. 3633–3652, Nov 1973.

[69] S. L. Glashow, "The renormalizability of vector meson interactions," *Nucl. Phys.*, vol. 10, pp. 107–117, 1959.

[70] A. Salam and J. C. Ward, "Weak and electromagnetic interactions," *Nuovo Cim.*, vol. 11, pp. 568–577, 1959.

[71] S. Weinberg, "A Model of Leptons," *Phys. Rev. Lett.*, vol. 19, pp. 1264–1266, 1967.

[72] G. Arnison *et al.*, "Experimental observation of isolated large transverse energy electrons with associated missing energy at $\sqrt{s} = 540$ GeV," *Physics Letters B*, vol. 122, no. 1, pp. 103 – 116, 1983.

[73] M. Banner *et al.*, "Observation of single isolated electrons of high transverse momentum in events with missing transverse energy at the CERN pp collider," *Physics Letters B*, vol. 122, no. 5, pp. 476 – 485, 1983.

[74] G. Arnison *et al.*, "Experimental observation of lepton pairs of invariant mass around 95 GeV/c^2 at the CERN SPS collider," *Physics Letters B*, vol. 126, no. 5, pp. 398 – 410, 1983.

[75] P. Bagnaia *et al.*, "Evidence for $Z^0 \to e^+e^-$ at the CERN anti-p p Collider," *Phys. Lett.*, vol. 129B, pp. 130–140, 1983.

[76] I. J. Martínez Soler, *Neutrino Oscillations in Particle Physics and Astrophysics*. PhD thesis, U. Autonoma, Madrid, 2018.

[77] J. R. Andersen *et al.*, "Handbook of LHC Higgs Cross Sections: 3. Higgs Properties," 2013.

[78] D. de Florian *et al.*, "Handbook of LHC Higgs Cross Sections: 4. Deciphering the Nature of the Higgs Sector," vol. 2/2017, 10 2016.

[79] G. Aad *et al.*, "Combined Measurement of the Higgs Boson Mass in *pp* Collisions at $\sqrt{s} = 7$ and 8 TeV with the ATLAS and CMS Experiments," *Phys. Rev. Lett.*, vol. 114, p. 191803, 2015.

[80] M. Aaboud *et al.*, "Measurement of the Higgs boson mass in the $H \to ZZ^* \to 4\ell$ and $H \to \gamma\gamma$ channels with $\sqrt{s} = 13$ TeV *pp* collisions using the ATLAS detector," *Phys. Lett.*, vol. B784, pp. 345–366, 2018.

[81] A. M. Sirunyan *et al.*, "A measurement of the Higgs boson mass in the diphoton decay channel," Tech. Rep. arXiv:2002.06398. CMS-HIG-19-004-003, CERN, Geneva, Feb 2020. Submitted to Phys. Lett. B. All figures and tables can be found at http://cms-results.web.cern.ch/cms-results/public-results/publications/HIG-19-004 (CMS Public Pages).

[82] G. Aad *et al.*, "Evidence for the spin-0 nature of the Higgs boson using ATLAS data," *Phys. Lett.*, vol. B726, pp. 120–144, 2013.

[83] V. Khachatryan *et al.*, "Observation of the Diphoton Decay of the Higgs Boson and Measurement of Its Properties," *Eur. Phys. J.*, vol. C74, no. 10, p. 3076, 2014.

[84] M. Aaboud *et al.*, "Cross-section measurements of the Higgs boson decaying into a pair of τ-leptons in proton-proton collisions at $\sqrt{s} = 13$ TeV with the ATLAS detector," *Phys. Rev.*, vol. D99, p. 072001, 2019.

[85] A. M. Sirunyan *et al.*, "Observation of the Higgs boson decay to a pair of τ leptons with the CMS detector," *Phys. Lett.*, vol. B779, pp. 283–316, 2018.

[86] A. M. Sirunyan *et al.*, "Observation of $\mathrm{t\bar{t}H}$ production," *Phys. Rev. Lett.*, vol. 120, no. 23, p. 231801, 2018.

[87] M. Aaboud *et al.*, "Observation of Higgs boson production in association with a top quark pair at the LHC with the ATLAS detector," *Phys. Lett.*, vol. B784, pp. 173–191, 2018.

[88] M. Aaboud *et al.*, "Observation of $H \to b\bar{b}$ decays and VH production with the ATLAS detector," *Phys. Lett.*, vol. B786, pp. 59–86, 2018.

[89] A. M. Sirunyan *et al.*, "Observation of Higgs boson decay to bottom quarks," *Phys. Rev. Lett.*, vol. 121, no. 12, p. 121801, 2018.

[90] M. Aaboud *et al.*, "Search for the Decay of the Higgs Boson to Charm Quarks with the ATLAS Experiment," *Phys. Rev. Lett.*, vol. 120, no. 21, p. 211802, 2018.

[91] A. M. Sirunyan *et al.*, "A search for the standard model Higgs boson decaying to charm quarks," Dec 2019. Submitted to JHEP. All figures and tables can be found at http://cms-results.web.cern.ch/cms-results/public-results/publications/HIG-18-031 (CMS Public Pages).

[92] "A search for the dimuon decay of the Standard Model Higgs boson in pp collisions at $\sqrt{s} = 13$ TeV with the ATLAS Detector," Tech. Rep. ATLAS-CONF-2019-028, CERN, Geneva, Jul 2019.

[93] A. M. Sirunyan *et al.*, "Search for the Higgs boson decaying to two muons in proton-proton collisions at $\sqrt{s} = 13$ TeV," *Phys. Rev. Lett.*, vol. 122, no. 2, p. 021801, 2019.

[94] M. Aaboud *et al.*, "Search for exclusive Higgs and Z boson decays to $\phi\gamma$ and $\rho\gamma$ with the ATLAS detector," *JHEP*, vol. 07, p. 127, 2018.

[95] M. Aaboud *et al.*, "Searches for exclusive Higgs and Z boson decays into $J/\psi\gamma$, $\psi(2S)\gamma$, and $\Upsilon(nS)\gamma$ at $\sqrt{s} = 13$ TeV with the ATLAS detector," *Phys. Lett.*, vol. B786, pp. 134–155, 2018.

[96] G. Aad *et al.*, "Combined measurements of Higgs boson production and decay using up to 80 fb^{-1} of proton-proton collision data at $\sqrt{s} = 13$ TeV collected with the ATLAS experiment," *Phys. Rev. D*, vol. 101, no. 1, p. 012002, 2020.

[97] V. Khachatryan *et al.*, "Search for a standard model-like Higgs boson in the $\mu^+\mu^-$ and e^+e^- decay channels at the LHC," *Phys. Lett.*, vol. B744, pp. 184–207, 2015.

[98] W. Altmannshofer, J. Brod, and M. Schmaltz, "Experimental constraints on the coupling of the Higgs boson to electrons," *JHEP*, vol. 05, p. 125, 2015.

[99] R. Harnik, J. Kopp, and J. Zupan, "Flavor Violating Higgs Decays," *JHEP*, vol. 03, p. 026, 2013.

[100] G. Aad *et al.*, "Evidence for the Higgs-boson Yukawa coupling to tau leptons with the ATLAS detector," *JHEP*, vol. 04, p. 117, 2015.

[101] G. Aad *et al.*, "Search for Higgs and Z Boson Decays to J/$\psi\gamma$ and Υ(nS)γ with the ATLAS Detector," *Phys. Rev. Lett.*, vol. 114, no. 12, p. 121801, 2015.

[102] C. Patrignani *et al.*, "Review of Particle Physics," *Chin. Phys.*, vol. C40, no. 10, p. 100001, 2016.

[103] M. Aaboud *et al.*, "Search for the dimuon decay of the Higgs boson in pp collisions at $\sqrt{s} = 13$ TeV with the ATLAS detector," *Phys. Rev. Lett.*, vol. 119, no. 5, p. 051802, 2017.

[104] "Prospects for the measurement of the rare Higgs boson decay $H \to \mu\mu$ with 3000 fb^{-1} of pp collisions collected at $\sqrt{s} = 14$ TeV by the ATLAS experiment," Tech. Rep. ATL-PHYS-PUB-2018-006, CERN, Geneva, May 2018.

[105] S. Alioli, P. Nason, C. Oleari, and E. Re, "NLO Higgs boson production via gluon fusion matched with shower in POWHEG," *JHEP*, vol. 04, p. 002, 2009.

[106] P. Nason and C. Oleari, "NLO Higgs boson production via vector-boson fusion matched with shower in POWHEG," *JHEP*, vol. 02, p. 037, 2010.

[107] T. Sjostrand, S. Mrenna, and P. Z. Skands, "A Brief Introduction to PYTHIA 8.1," *Comput. Phys. Commun.*, vol. 178, pp. 852–867, 2008.

[108] T. Gleisberg, S. Hoeche, F. Krauss, A. Schalicke, S. Schumann, and J. Winter, "Event generator for the LHC," *Nucl. Instrum. Meth.*, vol. A559, pp. 242–245, 2006.

[109] S. Frixione and B. R. Webber, "Matching NLO QCD computations and parton shower simulations," *JHEP*, vol. 06, p. 029, 2002.

[110] S. Frixione, P. Nason, and B. R. Webber, "Matching NLO QCD and parton showers in heavy flavor production," *JHEP*, vol. 08, p. 007, 2003.

[111] G. Corcella, I. G. Knowles, G. Marchesini, S. Moretti, K. Odagiri, P. Richardson, M. H. Seymour, and B. R. Webber, "Herwig 6: an event generator for hadron emission reactions with interfering gluons (including supersymmetric processes)," *Journal of High Energy Physics*, vol. 2001, no. 01, p. 010, 2001.

[112] J. M. Butterworth, J. R. Forshaw, and M. H. Seymour, "Multiparton interactions in photoproduction at HERA," *Z. Phys.*, vol. C72, pp. 637–646, 1996.

[113] G. Aad *et al.*, "Search for the Standard Model Higgs boson decay to $\mu^+\mu^-$ with the ATLAS detector," *Phys. Lett.*, vol. B738, pp. 68–86, 2014.

[114] J. E. Gaiser, *Charmonium Spectroscopy from Radiative Decays of the J/ψ and ψ'*. PhD thesis, Stanford University, 1982.

[115] "Projections for measurements of Higgs boson cross sections, branching ratios, coupling parameters and mass with the ATLAS detector at the HL-LHC," Tech. Rep. ATL-PHYS-PUB-2018-054, CERN, Geneva, Dec 2018.

[116] "A search for the dimuon decay of the Standard Model Higgs boson in pp collisions at $\sqrt{s} = 13$ TeV with the ATLAS Detector," Tech. Rep. ATLAS-CONF-2018-028, CERN, Geneva, Jul 2019.

[117] G. Aad *et al.*, "Searches for lepton-flavour-violating decays of the Higgs boson in $\sqrt{s} = 13$ TeV pp collisions with the ATLAS detector," *Phys. Lett. B*, vol. 800, p. 135069, 2020.

[118] S. Alioli, P. Nason, C. Oleari, and E. Re, "A general framework for implementing NLO calculations in shower Monte Carlo programs: the POWHEG BOX," *JHEP*, vol. 06, p. 043, 2010.

[119] K. Hamilton, P. Nason, E. Re, and G. Zanderighi, "NNLOPS simulation of Higgs boson production," *JHEP*, vol. 10, p. 222, 2013.

[120] R. D. Ball *et al.*, "Parton distributions for the LHC Run II," *JHEP*, vol. 04, p. 040, 2015.

[121] K. Hamilton, P. Nason, and G. Zanderighi, "MINLO: Multi-Scale Improved NLO," *JHEP*, vol. 10, p. 155, 2012.

[122] F. Cascioli, P. Maierhofer, and S. Pozzorini, "Scattering Amplitudes with Open Loops," *Phys. Rev. Lett.*, vol. 108, p. 111601, 2012.

[123] T. Gleisberg and S. Hoeche, "Comix, a new matrix element generator," *JHEP*, vol. 12, p. 039, 2008.

[124] S. Catani, L. Cieri, G. Ferrera, D. de Florian, and M. Grazzini, "Vector boson production at hadron colliders: a fully exclusive QCD calculation at NNLO," *Phys. Rev. Lett.*, vol. 103, p. 082001, 2009.

[125] T. Sjostrand, S. Mrenna, and P. Z. Skands, "PYTHIA 6.4 Physics and Manual," *JHEP*, vol. 05, p. 026, 2006.

[126] J. Pumplin, D. R. Stump, J. Huston, H. L. Lai, P. M. Nadolsky, and W. K. Tung, "New generation of parton distributions with uncertainties from global QCD analysis," *JHEP*, vol. 07, p. 012, 2002.

[127] D. J. Lange, "The EvtGen particle decay simulation package," *Nucl. Instrum. Meth.*, vol. A462, pp. 152–155, 2001.

[128] M. Czakon and A. Mitov, "Top++: A Program for the Calculation of the Top-Pair Cross-Section at Hadron Colliders," *Comput. Phys. Commun.*, vol. 185, p. 2930, 2014.

[129] "Comparison of Monte Carlo generator predictions for gap fraction and jet multiplicity observables in top-antitop events," Tech. Rep. ATL-PHYS-PUB-2014-005, CERN, Geneva, May 2014.

[130] N. Kidonakis, "Next-to-next-to-leading-order collinear and soft gluon corrections for t-channel single top quark production," *Phys. Rev.*, vol. D83, p. 091503, 2011.

[131] N. Kidonakis, "Two-loop soft anomalous dimensions for single top quark associated production with a W^- or H^-," *Phys. Rev.*, vol. D82, p. 054018, 2010.

[132] G. Aad *et al.*, "The ATLAS Simulation Infrastructure," *Eur. Phys. J.*, vol. C70, pp. 823–874, 2010.

[133] S. Agostinelli *et al.*, "GEANT4: A Simulation toolkit," *Nucl. Instrum. Meth.*, vol. A506, pp. 250–303, 2003.

[134] M. Aaboud *et al.*, "Electron efficiency measurements with the ATLAS detector using 2012 LHC proton–proton collision data," *Eur. Phys. J.*, vol. C77, no. 3, p. 195, 2017.

[135] "Selection of jets produced in 13TeV proton-proton collisions with the ATLAS detector," Tech. Rep. ATLAS-CONF-2015-029, CERN, Geneva, Jul 2015.

[136] "Tagging and suppression of pileup jets with the ATLAS detector," Tech. Rep. ATLAS-CONF-2014-018, CERN, Geneva, May 2014.

[137] I. Connelly, "Performance and calibration of b-tagging with the ATLAS experiment at LHC Run-2," *EPJ Web Conf.*, vol. 164, p. 07025, 2017.

[138] G. Aad *et al.*, "Performance of electron and photon triggers in ATLAS during LHC Run 2," *Eur. Phys. J.*, vol. C80, no. 1, p. 47, 2020.

[139] G. Aad *et al.*, "Measurement of the Z/γ^* boson transverse momentum distribution in pp collisions at $\sqrt{s} = 7$ TeV with the ATLAS detector," *JHEP*, vol. 09, p. 145, 2014.

[140] M. Bahr *et al.*, "Herwig++ Physics and Manual," *Eur. Phys. J.*, vol. C58, pp. 639–707, 2008.

[141] J. Bellm *et al.*, "Herwig 7.0/Herwig++ 3.0 release note," *Eur. Phys. J.*, vol. C76, no. 4, p. 196, 2016.

[142] M. Aaboud *et al.*, "Luminosity determination in pp collisions at $\sqrt{s} = 8$ TeV using the ATLAS detector at the LHC," *Eur. Phys. J.*, vol. C76, no. 12, p. 653, 2016.

[143] G. Aad *et al.*, "Search for the standard model higgs boson in the diphoton decay channel with 4.9 fb^{-1} of pp collision data at $\sqrt{s} = 7$ TeV with atlas," *Phys. Rev. Lett.*, vol. 108, p. 111803, Mar 2012.

[144] M. L. Mangano, M. Moretti, F. Piccinini, R. Pittau, and A. D. Polosa, "ALPGEN, a generator for hard multiparton processes in hadronic collisions," *JHEP*, vol. 07, p. 001, 2003.

[145] A. L. Read, "Presentation of search results: The CL(s) technique," *J. Phys.*, vol. G28, pp. 2693–2704, 2002.

[146] G. Cowan, K. Cranmer, E. Gross, and O. Vitells, "Asymptotic formulae for likelihood-based tests of new physics," *Eur. Phys. J.*, vol. C71, p. 1554, 2011. [Erratum: Eur. Phys. J.C73,2501(2013)].